High-Power Phased-Array Antennas Exploiting Polarization Rotation and Sub-Wavelength Periodic Structures

By

Zongtang Zhang

A dissertation submitted in partial fulfillment of

the requirements for the degree of

Doctor of Philosophy

(Electrical Engineering)

at the

UNIVERSITY OF WISCONSIN-MADISON

2022

Date of final oral examination: 08/02/2022

The dissertation is approved by the following members of the Final Oral Committee:

Nader Behdad, Professor, Electrical and Computer Engineering

John H. Booske, Professor, Electrical and Computer Engineering

Filiz Yesilkoy, Assistant Professor, Biomedical Engineering

Fikadu T. Dagefu, Research Scientist, U.S. Army Research Laboratory

Acknowledgments

It has been such a wonderful journey for me for the past five years at University of Wisconsin-Madison. I would like to take this opportunity to acknowledge the following individuals for helping me and supporting me during my doctoral studies.

First of all, I would like to express my gratitude to my advisors, Professor Nader Behdad and Professor John H. Booske. I would like to thank them for giving me the opportunity to work with them. Their encouragement, support, and mentorship have guided me through the difficulties in my research.

I would also like to thank the members of my doctoral committee, Professor Filiz Yesilkoy and Dr. Fikadu T. Dagefu, for their service and helpful suggestions towards the completion of this dissertation.

During the last five years at UW-Madison, I am fortunate to meet many talented colleagues and friends. Special thanks and appreciations go to Dr. Hung Luyen for his suggestions and assistance in dealing with the problems that I encountered in my research. I would also like to thank my fellow colleagues: Dr. Ruyu Ma, Dr. Yuzhang Zang, Dr. Meng Gao, Dr. Konstantinos Mavrakakis, Dr. Mohammad Ranjbar Nikkhah, Dr. Kai Ren, Dr. Mohammad Mahdi Honari, Dr. Nathan D. Strachen, Dr. Mirhamed Mirmozafari, Alex Bouvy, Ruben F. Delgado Castillo, Jiahao Zhao, and Jinkai Wu for their help and support.

I want to acknowledge the Office of Naval Research for their support. This work relates to Department of Navy awards N00014-16-1-2308 and N00014-19-1-2502 issued by the Office

of Naval Research. The United States Government has a royalty-free license throughout the world in all copyrightable material contained herein. Any opinions, findings, and conclusions or recommendations expressed in this material are those of the author and do not necessarily reflect the views of the Office of Naval Research.

Last but not least, I would like to express my sincere gratitude to my parents and my family. This dissertation would never been possible without their continuous encouragement, support and unconditional love.

Contents

List of Figures

List of Tables

Abstract

Phased-array antennas have been deployed to address some of the needs of various applications ranging from satellite, mobile, and airborne communications to radar and electronic warfare systems. However, their extreme cost and complexity have limited their application only to the most expensive pieces of military hardware. Therefore, new ideas for developing affordable, wideband, high-power-capable phased arrays are needed to enable the widespread use of this technology in future tactical systems. To address this need, this dissertation investigates four different designs of affordable, high-power-capable, passive phased-array antennas. The first design presented a dual-band polarization-rotating reflectarray. The proposed dual-band reflectarray is capable of independent beam control at each band. The second design introduced a high-power-capable, ultra-wideband phase shifter that exploits the concept of polarization rotation to achieve 1-bit electronic phase shifting capability while handling extremely high power levels. This high-power phase shifter can be used either in a high-power transmitarray or in a high-power, direct-fed, passive phased-array architecture. Two different Risley-prism-based, mechanically beam-steerable antennas were presented in Chapter 4 and 5. It can provide good 2D beam steering performance in the upper space with relatively simple structures. These two designs are expected to be useful in designing affordable, beam-steerable antennas in which scanning speed can be traded off to reduce system complexity.

Chapter 1

Introduction

1.1 Introduction and Background

A phased-array antenna typically consists of an array of antenna elements, which are fed coherently and use variable phase or time-delay control at each element to radiate electromagnetic energy in a desired direction and suppress energy radiation in undesired directions [1,2]. Existing phased-array antennas can be categorized into either active or passive electronically steered arrays (AESAs or PESAs), depending on the specific system architecture. Active electronically steered arrays (AESAs) use a Transmitter/Receiver (T/R) module for each radiating element [3, 4]. Each T/R module is a fully fledged transceiver that can not only amplify the transmitted and received signal, but also control the phase and amplitude of these signals to achieve beam steering. Passive electronically steered arrays (PESAs), on the other hand, only have a central transmitter and receiver, with phase shifters and attenuators located at each radiating element or sub-array. PESAs have less complicated implementations, in which only a single source is used to feed the array. The radiated power from the feeding source is then distributed over the array aperture. While both PESAs and AESAs have been widely used, each of these two types has its own advantages and disadvantages.

Since each array element has its own T/R module in AESA architecture, it offers more

degrees of freedom in controlling the relative phase and amplitude at each array element. Therefore, AESAs are capable of more flexible beam scanning, adaptive beam shaping and nulling, and multi-beam operation. One other advantage of AESAs is that in the case of the failure in a small amount of array elements, the overall performance of the array will not be severely deteriorated. Major issues in the development of AESAs include the high cost, complexity, limited bandwidth, power handling capability, and difficulties of thermal management [5–13]. This problem is more significant in high-power AESAs. The total radiated power was primarily determined by the T/R module in AESAs. At high-power levels, the power amplifier (PA) in each T/R module will operate in low-efficiency regimes, thereby limiting the average radiated power. Furthermore, the lower PA efficiency results in generation of significant heat that must be efficiently dissipated from the aperture. This thermal management in high-power AESAs complicates the array design, limits its power handling capability and also adds to its size, weight, cost and power consumption.

As opposed to AESAs, PESAs are less complex to design since it only needs a single source to feed the array. Major challenges in the design and deployment of PESAs include the cost, loss, bandwidth and power handling capability of their phase shifters, especially for high-power passive phased arrays. Unfortunately, few of the phase shifters in the literature can provide the desired properties of low-loss, low-cost, wide bandwidth, and high power handling capabilities simultaneously [14–26].

In recent years, there has been a growing interest in employing phased-array antennas in various applications ranging from satellite and airborne communications to radars and imaging systems [27–32]. While a number of phased-array systems have been deployed, their extreme cost and complexity have limited their application only to the most expensive pieces of military hardware. Therefore, many military systems that can potentially benefit from the capabilities offered by phased arrays are left behind. Thus, new ideas for developing affordable, high-power-capable phased arrays are needed to enable the widespread use of this technology in future tactical systems. To address this need, new approaches that have

the potential for developing affordable, high-power-capable, wideband phased-array antenna systems are presented. The designs introduced in this dissertation are expected to enable the development of wideband, beam-steerable, and affordable phased arrays capable of handling high power levels. The proposed phase shifters and arrays have several fundamental technical advantages over state-of-the-art in phased-array antennas. These include: 1) Significant reduction of cost and complexity; 2) Elimination of most T/R modules; 3) The capability of radiating high power levels; 4) Wide bandwidth; 5) Simplification of the thermal management solution and 6) Significant reduction of the feed network losses. The combination of these technical advantages combined with their simplicity is expected to make the proposed phase shifters and passive phased arrays practical solutions for addressing the problem of affordable array technology.

1.2 Proposed Approach

Examining the current state-of-the-art in high-power phased-array technology shows that the combination of high-power capability ($> 20\ W/cm^2$ continuous-wave radiated power), wideband operation (e.g. BW $> 50\%$), low cost, low design complexity and easy thermal management are not available form any one single technology. In this dissertation, two different approaches were proposed to advance the current state-of-the-art in high-power passive phased-arrays. The first approach was to design high-power phased array with polarization-rotating spatial phase shifters. The second approach was to implement mechanically beam-steerable antenna based on Risley prism concept.

Recently, the concept of polarization rotation (PR) has been exploited as a promising solution to design wideband spatial 1-bit phase shifters for use in transmitarrays [33–36] and reflectarrays [37–43]. For the reflective polarization-rotating phase shifter, the polarization of the reflected wave is rotated by 90° either in the clockwise or in the counter-clockwise direction. This geometrical rotation creates a very wideband phase shift of 0°/180° between

the waves reflected from bit-0 or bit-1 PR phase shifter. This way, the PR phase shifters can locally manipulate the phase if the reflected wave and collimate the reflected wave with 1-bit phase resolution. Similarly, a 1-bit transmissive polarization-rotating phase shifter rotates the polarization of the transmitted wave by either $+90^\circ$ or -90° with respect to that of the incident wave. This creates a geometric $0^\circ/180^\circ$ phase shift between the two differently rotated transmitted wave, thereby creating a 1-bit spatial phase shifter. Ref. [35] presented a wideband linearly polarized transmitarray antenna operating at 7–16 GHz using PR-based phase shifters having a wide bandwidth of 78%. A wideband, low-profile transmitarray using a PR-based phase shifting unit cell with a fractional bandwidth of 49% was presented in [36]. The PR concept has also been applied in [38, 39] to design reconfigurable reflectarrays having wideband operation in Ku-band for satellite communications. The 1-bit phase shifters presented in these two works have a wide bandwidth of about 30% [38] and 20% [39], respectively. My previous work demonstrated a wideband reflectarray design based on 1-bit, polarization-rotating phase shifters having a 40% bandwidth and relatively simple structure [41]. Lately, I built a wideband, electronically reconfigurable reflectarray antenna capable of beam scanning within a $\pm 60^\circ$ range over 8.5-11.5 GHz [43]. As demonstrated in these examples, 1-bit spatial phase shifters operating based on the PR concept have demonstrated their advantages in designing wideband transmitarrays and reflectarrays. In this thesis, a dual-band PR reflectarray with independent beam control at each band was proposed in Chapter 2. A high-power-capable, ultra-wideband, phase shifter based on PR concept that can be used either in a transmitarray or in a direct-fed passive phased-array architecture was presented in Chapter 3.

With the advancement of mechanical controlling technique, an alternative approach of high-power, beam-steerable array designs is to mechanically control the antenna configuration, including element control [44, 45], feed displacement [46–48] and array movement [49–58], to scan the beam. Although the beam-scanning speed can not compared with the electronically reconfigurable arrays, the simplicity, high efficiency, high-power capabil-

ity and easy thermal management of the proposed antenna system make it a promising candidate for affordable phased-array antennas for radar, radiative wireless power transfer, and on-the-move, point-to-point wireless communications systems. Most mechanical beam-steering systems using array movement methods need only one or two actuators to move or rotate the phase-shifting arrays. This attractive feature provides a good solution for simpler and more affordable beam-steerable antennas in applications that do not require high-speed beam scanning. Specifically, mechanical beam-steerable antenna systems based on the Risley prism concept have attracted attention for their simplicity and good beam scanning performance [53–58]. In the optical regime, a Risley-prism system typically consists of a pair of rotatable wedge-shaped prisms used in conjunction with a well-collimated beam of light (e.g., a laser beam) [59,60]. The beam can be steered when the prisms are rotated with respect to each other. In the microwave regime, the two wedge-shaped prisms used in optical systems were replaced by a pair of flat prisms, illuminated by a feed antenna [53]. The spherical wave radiated by the feed antenna is collimated by the lens placed below the two flat prisms. The relative rotational displacement between two prisms provides beam steering in both azimuth and elevation directions in the upper hemisphere of the outgoing aperture. Each flat prism is generally implemented by multilayer printed circuit boards. In this thesis, two different Risley-prism-based, mechanically beam-steerable antennas will be discussed in Chapter 4 and 5. The proposed Risley-prism-based antenna system was implemented with a much simplified architecture and provides good beam scanning performance.

1.3 Overview of the Dissertation

The aim of this research is to advance the current state-of-the-art in spatial phase shifters and high-power passive phased-arrays by addressing the existing limitations. The efforts undertaken to accomplish this research goal have been presented in detail in several chapters of this dissertation. A brief overview of each chapter is provided as follows.

Chapter 2 presents the design and proof-of-concept demonstration of a dual-band reflectarray antenna capable of generating two beams at X and Ku bands, whose directions of maximum radiation can be set independently from each other. The reflectarray uses dual-band PR unit cells with 1-bit phase quantization. The proposed unit cell provides independent phase shifts at two frequency bands by controlling a cluster of two orthogonal dipoles to operate as either $+90^\circ$ or -90° reflective polarization rotators. Two dipole clusters are interleaved in a unit cell and used to achieve dual-band operation. Simulation results of a unit cell designed to operate at X and Ku bands demonstrate independently controlled, dual-band PR operation over 16.1% and 20% bandwidths for the lower and higher bands, respectively. The dual-band unit cells were used to construct three different static reflectarray prototypes demonstrating the different ways where such independent phase control at the two bands of a dual-band reflectarray antenna may be advantageous. The three static reflectarray prototypes were simulated, fabricated, and experimentally characterized. Simulation and measurement results of these prototypes agree well and demonstrate independent phase shift control at the X and Ku bands over a relatively wide field of view without exciting grating lobes.

Chapter 3 presents the design and high-power experimental characterization of a wideband, high-power-capable, electronically reconfigurable phase shifter for high-power phased-array applications. The device studied in this work offers an electronically switchable, 1-bit phase shift using the concept of PR. The PR-based phase shifter is designed to work in a custom-designed, double-ridge (DR) waveguide environment. Two PIN diodes are used to control the transmission phase of the signal by rotating the polarization of the incident wave by either $+90^\circ$ or -90° with respect to that of the incident wave, thereby creating a wideband, 1-bit phase shift between the two states. Simulation results demonstrated that this element can work over one octave bandwidth ranging from 6 to 12 GHz. A prototype of the device was fabricated and experimentally characterized at low- and high-power levels. The measurement results confirmed the simulations and demonstrated the wideband, high-

power-density capability of the device. High-power continuous-wave (CW) experiments were conducted across the entire 6-12 GHz band and demonstrated that the CW power handling capability of the device exceeds 23.6 W/cm^2. High-power pulsed power experiments conducted at 9.382 GHz demonstrated that the peak power handling capability of the device exceeds 347 W/cm^2 for short duration pulses.

Chapter 4 presents a beam-steerable antenna system that uses two mechanically-rotatable, phase-shifting surfaces (PSSs) functioning like a pair of Risley prisms for beam scanning operation at X-band. One of the PSSs also acts as a lens, performing beam collimation in addition to providing a phase shift gradient. Unit cells constituting the two PSSs were co-designed to determine the distance between the two surfaces that results in high transmission coefficients and small phase errors under different beam-scanning conditions. Both simulation and measurement results have verified that the distance of 2 mm provides the best performance regarding to peak gain. Prototypes of the PSSs having circular apertures with diameters of $11.5\lambda_0$ at 10 GHz were fabricated and illuminated by a feed antenna to characterize the beam scanning performance. The measurement results of the proposed antenna system demonstrate the capability to steer the main beam within a $\pm 60^\circ$ scanning range with a maximum gain variation of less than 3.6 dB by rotating the two PSSs with respect to each other. The fabricated prototype provides side lobe levels less than -13.1 dB, polarization purity higher than 20 dB, and small beam pointing errors of no more than 1° in all examined beam scan scenarios.

Chapter 5 presents a low-profile, mechanically beam-steerable antenna that implements the Risley prism beam-steering concept using only a single flat prism. The proposed antenna achieves 2D beam steering and consists of two parts: a holographic leaky-wave antenna and a PSS that acts as a flat prism. The lower holographic leaky-wave antenna both acts as the feed for the prism and provides a phase-shifting gradient over its output aperture. When paired with the flat prism, the system can provide 2D beam steering by mechanically rotating the two layers against each other. Unlike conventional Risley-prism-based beam-

steerable antennas, the proposed approach results in a very low-profile antenna and does not need spatial illumination of a two-prism system with a separate feed antenna. The flat prism is implemented using a PSS consisting of low-pass, hexagonal-shaped, spatial phase shifters. A prototype antenna with an overall thickness of only 1.1 λ_0 at 10 GHz was designed, fabricated, and experimentally characterized. Measurement results agree well with theoretical predictions and both show wide-angle beam scanning ranging from 0°-57° in the elevation and 0°-360° in the azimuth plane. The proposed antenna system has an equivalent aperture diameter of 7.1 λ_0 and a measured peak gain of 22.3 dBc at 10 GHz, corresponding to an aperture efficiency of 34.5%. The proposed concept is expected to be useful in designing low-profile, beam-steerable antennas in which scanning speed can be traded off to reduce system complexity.

In chapter 6, some insight with respect to the future work of this dissertation is provided.

Chapter 2

A Dual-Band Polarization-Rotating Reflectarray With Independent Phase Control at Each Band

The full manuscript is published as:

Z. Zhang, H. Luyen, J. H. Booske and N. Behdad, "A dual-band polarization-rotating reflectarray with independent phase control at each band," *IEEE Trans., Antennas Propag.*, vol. 69, no. 9, pp. 5546-5558, Sept. 2021.

2.1 Introduction

In recent years, reflectarray antennas have attracted significant interest as alternatives to conventional high-gain reflector antennas for radar and satellite communication applications [61–64]. The beam collimation and pointing operation of a reflectarray antenna can be achieved by controlling the reflection phase of each of its spatial phase shifters that populate the reflectarry's aperture. It is ideally desirable to provide continuous phase variation for each phase-shifting element between 0° and 360°. However, the continuous 360° tuning ability generally comes at the cost of high profile and narrow bandwidth of the reflectarray. Reflectarrays using 1-bit phase correction have received significant attention for their low complexity and low loss, especially for applications requiring large-aperture arrays. Various 1-bit reflectarray antennas have been reported to show a good balance between the design complexity and beam pointing performance [63–71].

In many wireless applications, such as point-to-point, point to multi-point, and satellite communication systems, dual-band antenna systems that share the same aperture may be required. In such situations, using the same aperture to meet the needs of the different frequency bands helps reduce the cost, size, and weight of the overall system. In such dual-band applications, the ability to achieve independent phase shift control at each band is critical as it allows for generating different phase shift patterns (i.e., Fresnel patterns) over the reflectarray's aperture at the two bands. This has several implications. First, it allows for generating beams that are pointed towards different directions in space if needed. More importantly, however, to achieve a good beam collimation at different frequencies, the Fresnel patterns generated over the aperture will be different (due to the difference in wavelength and the optical path length, in terms of the wavelength, between the feed point and any point on the surface of the reflectarray) at the two bands. This is the case even if both beams are pointed towards the same direction for both center fed and offset fed reflectarray antennas. Thus, development of dual-band reflectarray unit cells that can provide independent phase

control at each band is an important problem.

A thorough literature review reveals numerous publications on dual-band transmitarray [72–76] and reflectarray antennas [77–90]. Reference [78] reported a single-layer dual-band reflectarray operating in X and K bands. Each unit cell of the presented reflectarray consists of a circular patch with slots and two phase-delay lines attached to the patch. While varying the lengths of the phase-delay lines allows for adjusting the phase shift of each unit cell continuously, independent phase control ability at different bands was not achieved. In [82], a dual-band, single-layer reflectarray antenna operating at X and K bands was presented. This reflectarray element consists of a circular patch and a microstrip ring, both of which are attached to two phase-delay lines to tune the phase shift of each unit cell. However, the unit cell has an electrical size of $0.56\lambda_0$ at the central operating frequency of the higher band, causing non-negligible grating lobes when the main beam is pointed at large oblique angles. Additionally, this reflectarray only works with a single linear polarization. In [87], a dual-band, dual-circularly polarized reflectarray has been reported for K and Ka band satellite communications. To achieve this, dual-band dual-linearly-polarized reflectarray and a dual-band polarizer were placed apart from each other. This allows the beam and polarization of the dual-band reflectarray to be independently controlled at different bands. However, this reflectarray backed by FSS has only 2.2% and 2.9% 1-dB bandwidth at the lower and higher bands, respectively. This reflectarray also has a high profile due to the multiple layer structure. Overall, dual-band, dual-polarized reflectarray antennas with independent phase shift or beam control at different bands are rarely reported and are relatively difficult to design because of the coupling and interaction between higher- and lower-band features. My goal for this study was to achieve a dual-band, dual-polarized reflectarray with independent beam control, low side lobe level (below -15 dB), significant bandwidth (at least 15% 3dB bandwidth at both bands), and unit cell dimensions smaller than $0.5\lambda_0$ at both bands to avoid grating lobes.

Recently, 1-bit phase shifters exploiting polarization rotation concept have been studied

as a promising solution to design wideband, low-complexity reflectarrays and transmitarrays [36, 37, 39–41]. My previous work [41] demonstrated a wideband reflectarray design based on 1-bit, polarization-rotating phase shifters having a 40% bandwidth and relatively simple structure. Other 1-bit reflectarrays based on non-PR approach mostly relied on using microstrip patches as array elements [65, 66, 89], which generally achieved less than 10% bandwidth. Furthermore, using resonant structures to achieve 1-bit reflectarrays generally results in relatively large unit cell dimensions and may cause grating lobes if the beam is not directed towards broadside or if the reflectarray is to be used with an off center feed.

In this chapter, I present a dual-band, 1-bit spatial phase shifter design using the polarization rotation concept. This spatial phase shifter can be used to construct dual-band reflectarray antennas capable of offering independent phase shift and beam directions at two different operating frequency bands. The proposed polarization-rotating unit cell (PRUC) provides dual-band operation by diagonally interleaving two similar polarization-rotating structures with different physical dimensions. Each structure consists of two orthogonal dipoles on the top surface with different backside connections to control the reflection phase state (with relative values of $0°/180°$) at each frequency band. An illustrative PRUC was designed to operate in the X and Ku bands. The unit cell has periods of $0.232\lambda_{0L}$ and $0.4\lambda_{0H}$ at the center frequencies of the lower band and higher band, respectively. This eliminates the possibility of exciting grating lobes in any band for off-broadside beam directions or offset feed locations. Simulation results of the illustrative dual-band unit cell show independent control of 1-bit phase shift at each band. This PRUC was subsequently used to construct three proof-of-concept, dual-band reflectarrays designed to demonstrate the different ways the unit cell may be used. I fabricated and experimentally characterized these different static prototypes. The first prototype was designed to collimate the main beams towards broadside direction at both bands with center feeds. This design illustrates that having independent phase control at each band is vital because the Fresnel patterns needed for beam collimation are different at the two bands, even in this simplest of cases. The second prototype was con-

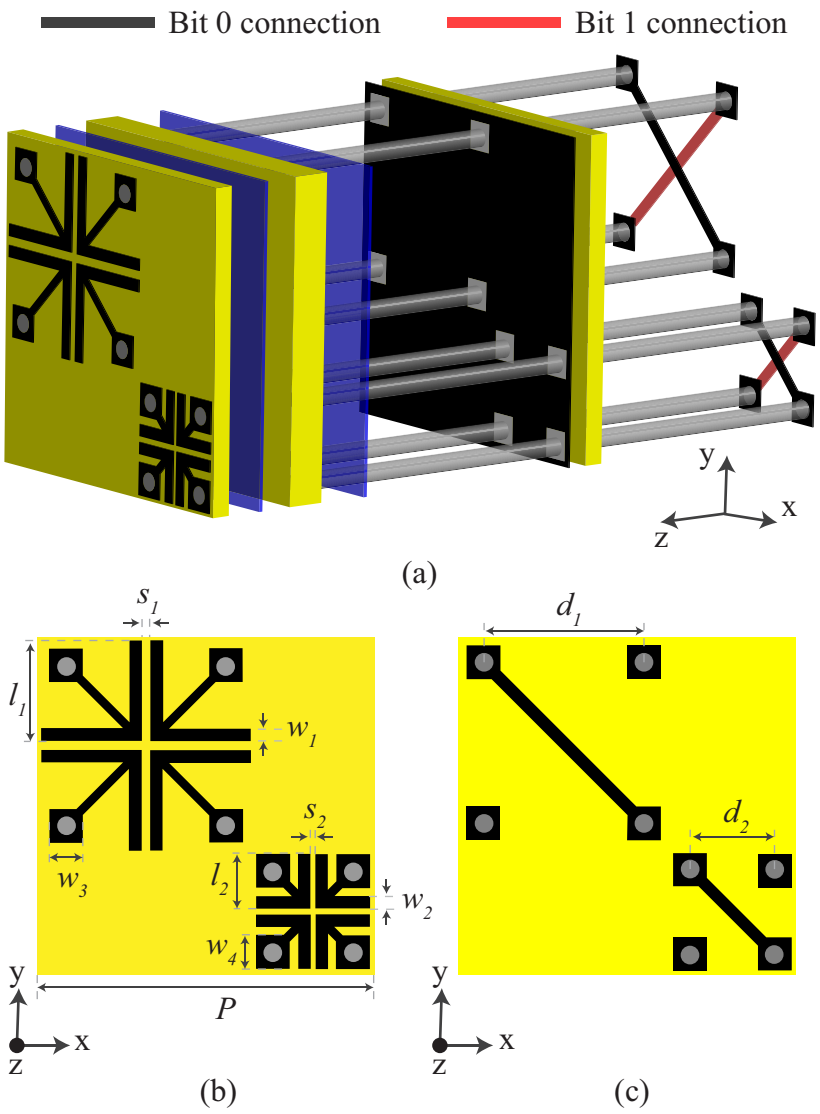

Figure 2.1: (a) Three-dimensional topology of the proposed dual-band, polarization-rotating unit cell with back-side connections. (b) Top surface of the unit cell. (c) Bottom surface of the unit cell for one of the backside configurations. Dark gray and black represent metal, yellow represents dielectric substrates, and blue represents bonding layers.

figured to have the main beams at $\theta = 45°$, $\phi = 0°$ at the lower band and $\theta = 45°$, $\phi = 180°$ at the higher band with center feeds. The third prototype was configured for generating the main beams at broadside direction at both bands with offset feeds.

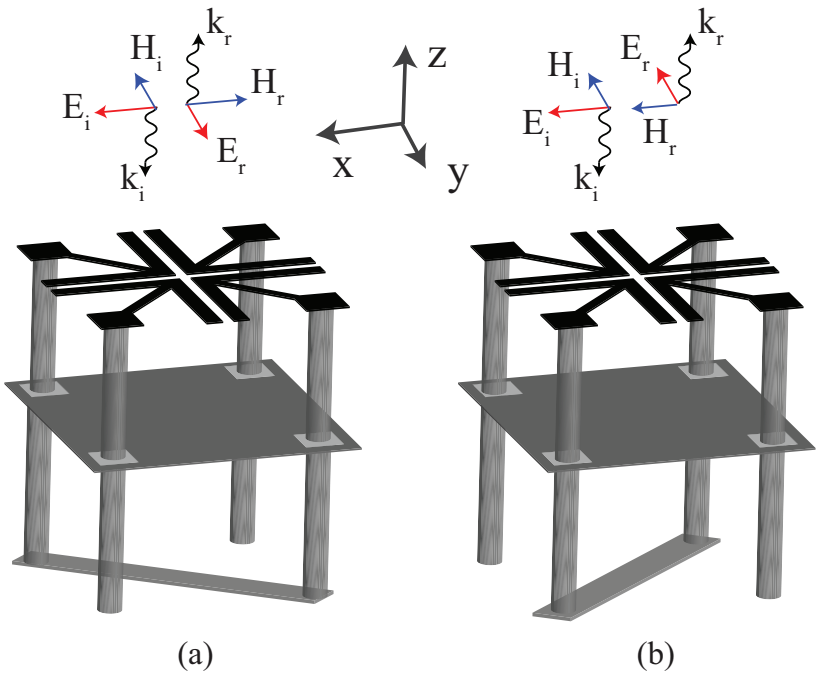

Figure 2.2: Illustration for the polarization rotation operation of (a) bit-0 and (b) bit-1 configurations of a dipole cluster under illumination of an $\hat{x}$-polarized incident plane wave.

2.2 Unit Cell Design and Simulations

Fig. 2.1 shows the topology of the proposed dual-band PRUC having three metallic layers. The top metallic layer consists of two dipole clusters, each of which is formed by four single-headed arrows pointing towards the clusters' respective centers. Each dipole cluster is connected to four vias going through four slots in a ground plane and reaching the bottom metallic layer, where two vias along a diagonal line are connected by a conducting strip while the other two vias are left open. The larger dipole cluster and corresponding back-side connection provide 1-bit phase shift for the lower frequency band. Similarly, the smaller dipole cluster can be controlled via the respective back-side connection to realize 1-bit phase shift for the higher frequency band.

Each (of the two) dipole clusters acts as a 1-bit polarization-rotating phase shifter with the operating principle similar to that of the unit cell reported in [41]. Therefore, detailed explanation for the polarization-rotation operation of the unit cell will not be repeated

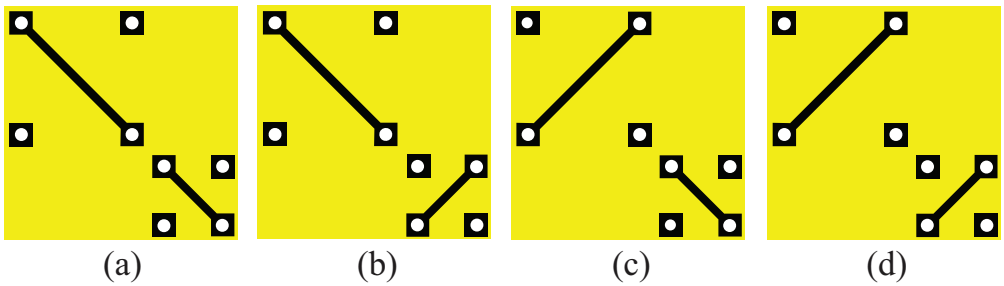

Figure 2.3: Four different back-side configurations of the proposed dual-band unit cell: (a) bit (0, 0) configuration, (b) bit (0, 1) configuration, (c) bit (1, 0) configuration, and (d) bit (1, 1) configuration. The first digit refers to the state of the lower band and the second digit refers to the state of the higher band.

here for brevity. Instead, I provide a brief description of how 1-bit phase shift is achieved by controlling the connections on the back side of the unit cell. Fig. 2.2 illustrates the operation of each dipole cluster of the proposed PRUC in two modes corresponding to two backside connection configurations. The conducting strips on the back side of the unit cell are orthogonal for the two operating modes, which are referred to as bit-0 and bit-1 configurations. When the incident electric field vector points towards the positive $\hat{x}$-direction, the bit-0 unit cell provides a reflected electric field vector pointing towards the positive $\hat{y}$-direction. Similarly, the bit-1 unit cell provides a reflected electric field vector pointing towards the negative $\hat{y}$-direction. Therefore, the bit-0 and bit-1 unit cells produce reflected electric field vectors pointing in opposite directions with equal amplitude, which is equivalent to a phase difference of 180°. The lower-band and higher-band features can be independently configured in bit-0 and bit-1 states, resulting in four total combinations for the proposed PRUC. These four states are labeled as bit (0, 0), bit (0, 1), bit (1, 0), and bit (1, 1) with corresponding back-side connection configurations shown in Fig. 2.3. Note that the first digit (e.g., 0 in bit (0, 1)) refers to the state of the lower-band feature and the second digit (e.g., 1 in bit (0, 1)) represents the state of the higher-band feature.

Unlike the unit cell presented in [41], the four arrowheads of each dipole cluster are pointed towards each other and towards the center of the dipole cluster in this design. This modification was made to miniaturize the dimensions of the dipole clusters. The size

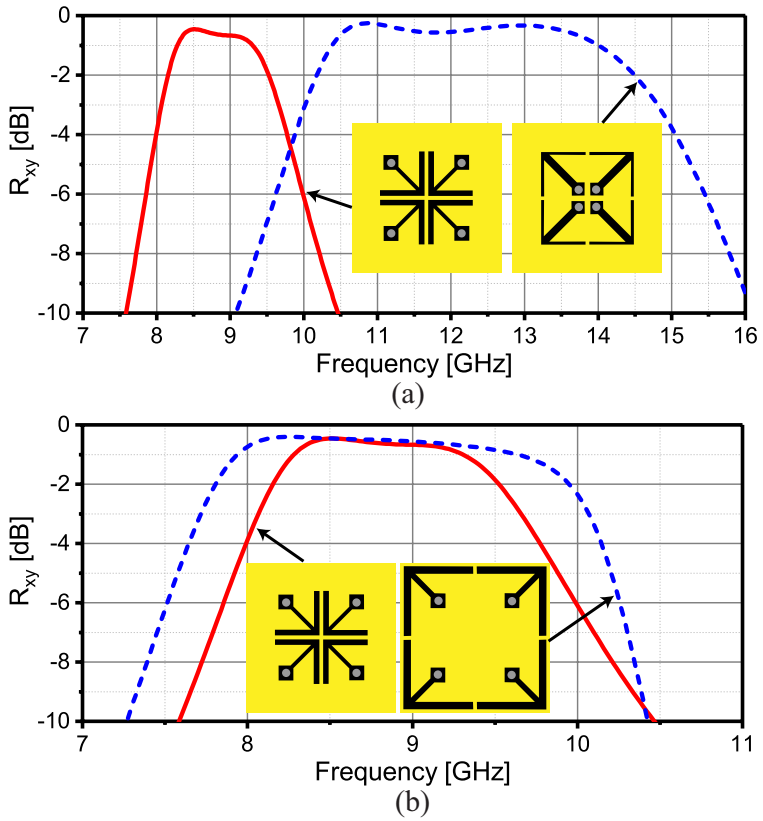

Figure 2.4: Comparison of the simulated reflection coefficients, R_{xy}, of unit cells with different arrow orientations and/or dimensions. (a) Two unit cells with inwardly and outwardly pointing arrows having the same overall dimensions of 5 mm × 5 mm. (b) Two unit cells with inwardly and outwardly pointing arrows having the same center operating frequency but different overall dimensions for the dipole clusters. Specifically, the inward pointing arrow unit cell was 5 mm × 5 mm, whereas the out-pointing-arrow unit cell was 7.7 mm × 7.7 mm (approximately 237% larger area).

miniaturization effect is illustrated in Fig. 2.4, which presents the simulated co-polarization reflection coefficients, R_{xy}, for four different single-band unit cells having the same periodicity of 8 mm but different orientations and dimensions of the arrows. Fig. 2.4(a) shows the simulated R_{xy} for two single-band PRUCs with different arrowhead orientations. The dipole clusters of the two unit cells occupy the same area of 5 mm × 5 mm. The center operating frequency of the unit cell having four inwardly pointing arrows is 8.9 GHz, which is about 1.4 times smaller than the center operating frequency of 12.4 GHz observed for the unit cell having four outwardly pointing arrows. Fig. 2.4(b) shows the simulated R_{xy} for two unit cells with different arrow orientations, whose dimensions were tuned to have the same center

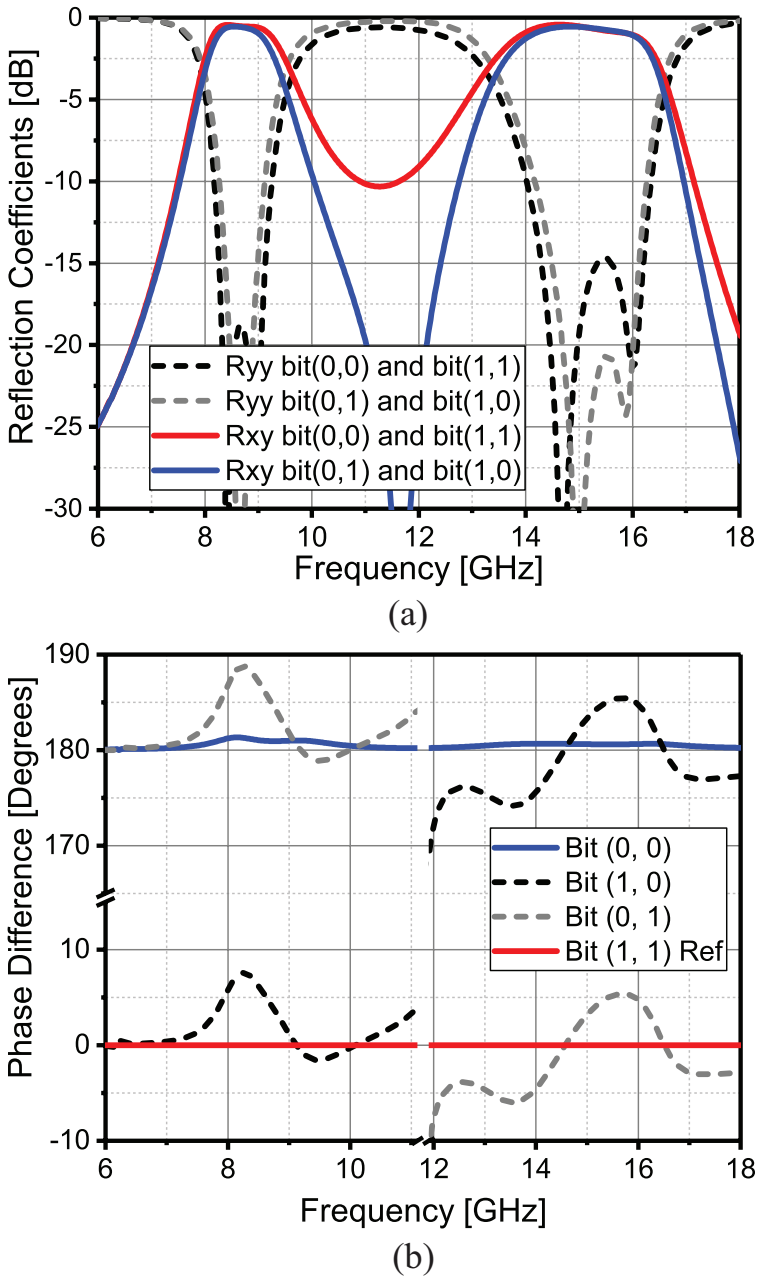

Figure 2.5: Simulated reflection coefficients of the dual-band polarization-rotating spatial phase shifter in different states. (a) Magnitudes of the co-polarization (R_{xy}) and cross-polarization (R_{yy}) reflection coefficients of four operating modes of the PRUC. (b) Phases of the co-polarization reflection coefficients of four operating modes of the unit cell.

operating frequencies. In order to get the same center operating frequency as the unit cell with inwardly pointing arrows, the unit cell with outwardly pointing arrows needs to have a larger dipole cluster occupying an area of 7.7 mm $\times$ 7.7 mm (about 237% larger area

compared to the other unit cell). Therefore, inwardly pointing arrows allows for efficiently reducing the footprint of the dipole clusters and place the higher- and lower-band clusters further apart given a certain unit cell size, thereby minimizing the coupling between them. As will be shown later, this enables the unit cell to have independent phase control at each band while being smaller than half a wavelength at the higher band.

The dual-band PRUC was simulated in CST Microwave Studio using periodic boundary conditions and tuned to achieve two operating bands centered at 8.7 GHz and 15 GHz. In this illustrative embodiment, the unit cell structure comprises three Rogers RO4003C substrates having thicknesses of 0.81 mm, 1.52 mm, and 0.81 mm for the top, middle, and bottom substrates, respectively, and a dielectric constant of 3.38. The three dielectric substrates are bonded by two Rogers RO4450F prepreg layers with a dielectric constant of 3.52 and thicknesses of 0.1 mm. The unit cell's periodicity is 8 mm, which is $0.232\lambda_0$ at 8.7 GHz and $0.4\lambda_0$ at 15 GHz. This period of the unit cell (less than $0.5\lambda_0$ at both bands) allows for avoiding grating lobes for the dual-band beam steering reflectarray constructing with the proposed PRUC. The dimensions of the proposed PRUC, including the widths and lengths of the arrowheads (w_1, l_1, w_2 and l_2), spacings between the arrowheads (s_1 and s_2), spacings between the vias (d_1 and d_2), and the square pads' widths (w_3 and w_4), were tuned to achieve high co-polarization reflection coefficients for both bands. Final values are given in Table 2.1.

Table 2.1: Dimensions (in mm) of the proposed dual X-/Ku-band unit cell.

P	l_1	l_2	s_1	s_2	w_1	w_2	w_3	w_4	d_1	d_2
8	2.4	1.3	0.2	0.2	0.3	0.3	0.8	0.8	3.8	2

Fig. 2.5(a) shows the magnitudes of the simulated co-polarization and cross-polarization reflection coefficients, R_{xy} and R_{yy}, of four different states of the PRUC. Several observations about the results in this figure were noted. First, the bit (0, 0) and bit (1, 1) cells have identical responses and so do the bit(1, 0) and bit (0, 1) cells. Second, there are slight

differences in the reflection for the different states. For example, the upper edge of the lower band of the bit (0, 0) state's $|R_{xy}|$ is slightly higher than for the bit (0, 1) state, and the lower edge of the higher band of the bit (0, 0) state's $|R_{xy}|$ is slightly lower than for the bit (0, 1) state. However, these slight differences are not considered significant. Second, the dip in $|R_{xy}|$ between the two bands was deeper for bit (0, 0) state versus bit (0, 1) state. However, this did not interfere with meeting any of the design objectives and, again, is insignificant. Overall, the 3 dB reflection coefficient bandwidths, over which $|R_{xy}| > -3$ dB, of the proposed PRUC cover 8-9.4 GHz (16%) for the lower band and 13.5-16.5 GHz (20%) for the higher band. The phase responses of the simulated co-polarization reflection coefficient R_{xy} for the four modes are shown in Fig. 2.5(b). The phase of R_{xy} of the bit (1, 1) cell was taken as the reference to calculate the relative reflection phase values of all four modes. The phase differences between the bit (0, 0) and bit (1, 1) cells are almost 180° over the two operating bands. Changing the phase state at the higher band (or lower band) causes a small fluctuation of less than ±8° in the phase value at the lower band (or higher band), as can be seen by comparing the phases of the bit (1, 1) and (1, 0) (or (1, 1) and (0, 1)) cells. Meanwhile, the cells with different phase states in one band provide a phase difference of within ±8° of 180°, regardless of the phase state of the other band. These results demonstrate the ability of the proposed PRUC to independently control the phase state at the two frequency bands with negligible inter-band influence.

2.3 Design of a Beam-Steerable, Dual-Band Reflectarray

The proposed PRUCs were used to construct a beam-steerable, dual-band reflectarray antenna. The reflectarray has a square aperture with dimensions of 304 × 304 mm^2, equivalent to about $8.8\lambda_0 \times 8.8\lambda_0$ at 8.7 GHz and $15.2\lambda_0 \times 15.2\lambda_0$ at 15 GHz. Fig. 2.6 illustrates the configuration of the designed dual-band reflectarray antenna with center feed and offset feed

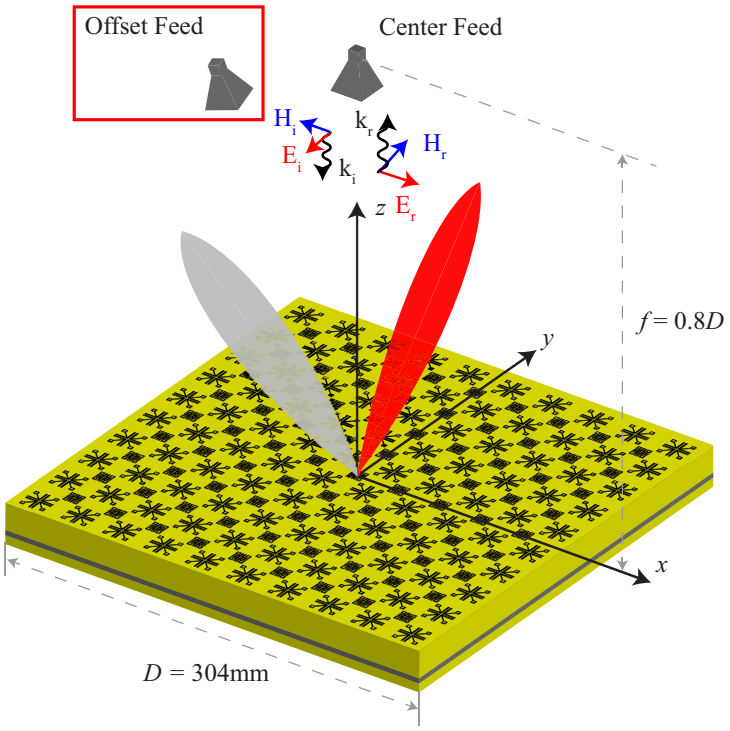

Figure 2.6: Different configurations of the proposed dual-band, polarization-rotating reflectarray antenna studied in this work.

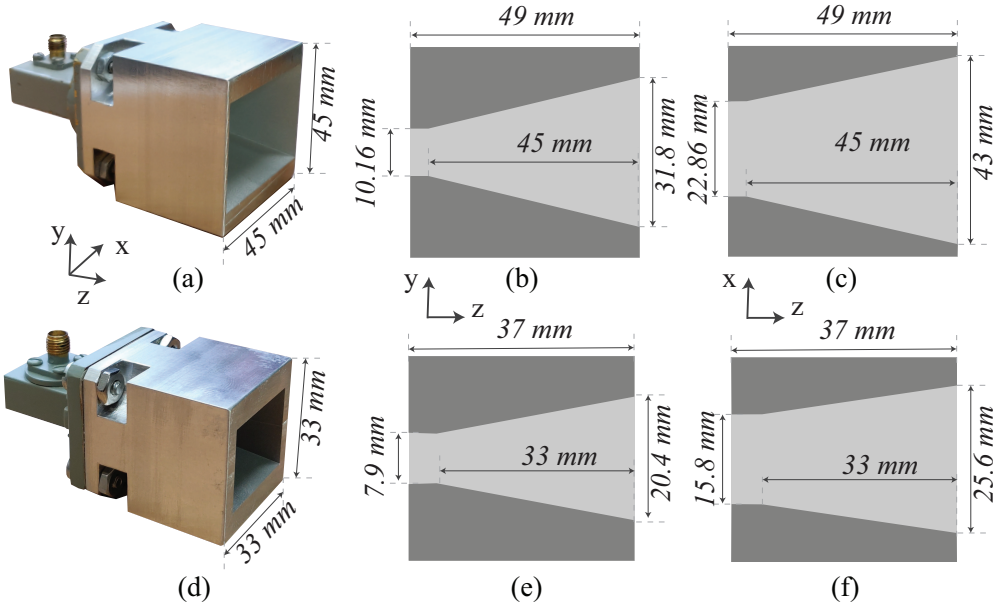

Figure 2.7: Photographs of the fabricated (a) X-band and (d) Ku-band feed horn antennas. The dimensions of the fabricated antennas at different cross section planes (b) y-z plane of X-band horn, (c) x-z plane of X-band horn, (e) y-z plane of Ku-band horn and (f) x-z plane of Ku-band horn are shown.

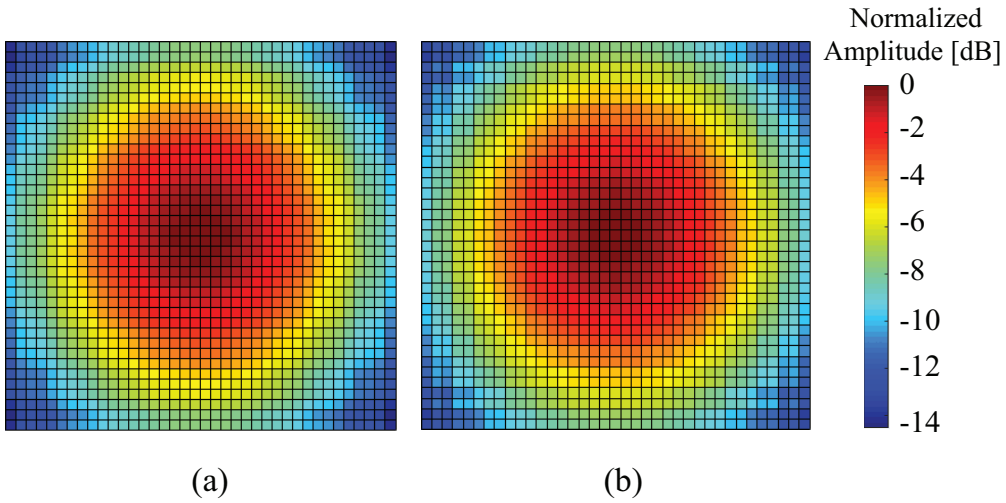

Figure 2.8: Simulation results for normalized electric field pattern generated by the (a) X-band and (b) Ku-band feed horn antennas on the plane of the reflectarray for center-fed cases.

scenarios. Two custom-made horn antennas, one working at X-band and the other working at Ku-band, with nearly rotationally symmetric radiation patterns were used for this illustrative design. An advantage of using two separate horn antennas over one wideband antenna is that the physical dimensions of the two antennas can be chosen differently to provide similar f/D ratios for optimum illumination efficiency at both frequency ranges. This is generally difficult to achieve with one single antenna since the amplitude tapering and phase wrapping over the illuminated aperture change as a function of frequency as the electrical size of the feed antenna varies. Since the focus of this work was to demonstrate the value of the dual-band unit cell design, I decided to use two separate antennas for achieving optimum aperture efficiencies at both operating frequency bands to better assess the beam collimation and steering performance of the illustrative dual-band reflectarray. However, this does not preclude the use of a single wideband (or dual-band) feed antenna with the reflectarray if required in a practical scenario. The X-band and Ku-band horn antennas are made of aluminum and have aperture dimensions of 45×45 mm^2 ($1.3\lambda_0 \times 1.3\lambda_0$ at 8.7 GHz) and 33×33 mm^2 ($1.7\lambda_0 \times 1.7\lambda_0$ at 15 GHz), respectively. These specific aperture dimensions were chosen to be no larger than the cross-sectional areas of the flanges of the respective

SMA-to-waveguide adapters used for the two bands, to minimize aperture blockage for the reflectarray. Photographs and dimensions of the two feed horn antennas connected to their respective SMA-to-waveguide adapters are shown in Fig. 2.7.

The design process started with conducting full-wave simulations of the feed horn antennas (without the reflectarray) using CST Microwave Studio to compute the phase and amplitude distribution of the incident electric fields generated by the feed antennas on the surface coinciding the reflectarray aperture at frequencies of interest. Fig. 2.8 shows the corresponding simulated electric field distributions generated by the two feed antennas at 8.7 GHz (for the X-band antenna) and 15 GHz (for the Ku-band antenna) for center-fed cases. The amplitudes of the incident electric fields at the four corners of the reflectarray aperture are about 14 dB lower than those at the reflectarray's center at both 8.7 GHz and 15 GHz. The optimal f/D ratios of each antenna at a frequency are identified as the f/D ratios that result in the maximum illumination efficiency at that frequency. The illumination efficiencies, which are the product of spillover efficiencies and tapering efficiencies, can be calculated from the radiation patterns of the feed antennas at 8.7 GHz (for the lower-band feed) and 15 GHz (for the higher-band feed) using formulas provided in [91,92]. This calculation leads to the optimal f/D of 0.8 for both lower-band and higher-band feed antennas.

Subsequently, the phases of the incident electric fields generated by the horn antennas were used to determine the Fresnel patterns for the 1-bit phase shifters of the reflectarray. Since the beam collimation is independent at the two frequency bands, there are two separate Fresnel patterns, one for the lower band and the other for the higher band, overlapping in the same physical aperture. For the lower band, the incident phases at the respective frequency were sampled at the physical centers of the lower-band dipole clusters and used to derive the lower-band Fresnel pattern. Similarly, the higher-band Fresnel pattern was determined using the incident phases (at the respective frequency) sampled at the physical centers of the higher-band dipole clusters. Due to the displacement of the center points of the lower- and higher-band dipole clusters with respect to each other, the reflectarray can be considered

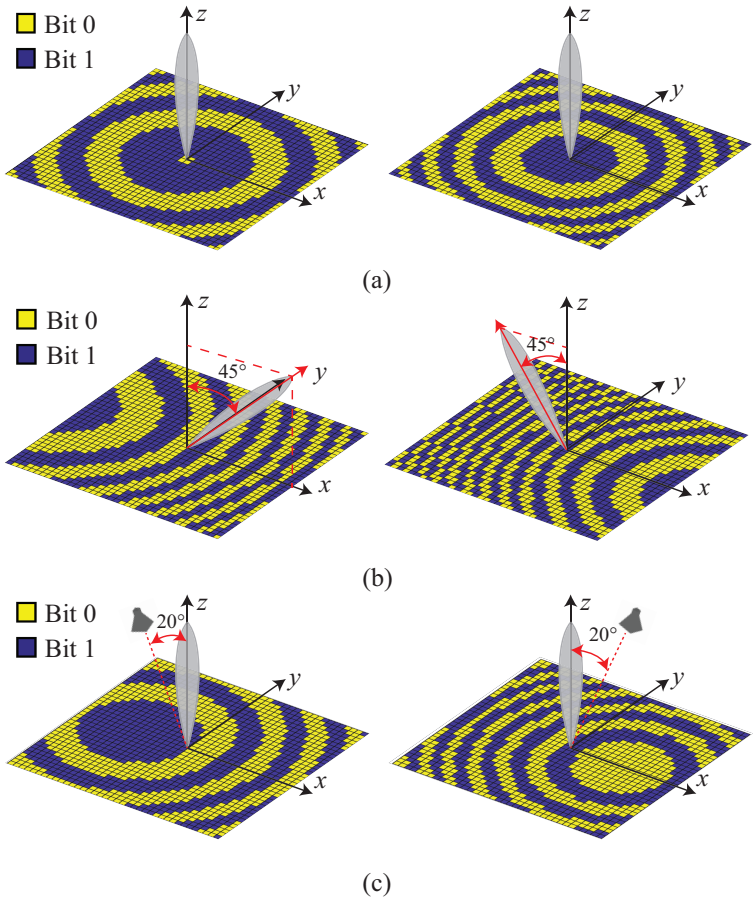

Figure 2.9: GA-optimized phase shift patterns of 1-bit phase shifters populating the apertures of the three different dual-band polarization rotating reflectarray designs examined in this work. (a) Design 1 providing broadside beam at both bands with center feeds. (b) Design 2 providing beams directed towards $\theta = 45°$, $\phi = 0°$ at the lower band and $\theta = 45°$, $\phi = 180°$ at the higher band with center feeds. (c) Design 3 providing broadside beams at both bands with offset feeds. Left: lower band. Right: higher band.

to consist of 38×38 lower-band elements and 37×37 higher-band elements. For each band, the Fresnel pattern was determined for each combination of beam collimation scenario and frequency according to the procedure presented in [40, 41]. Following the derivation of the Fresnel patterns, a genetic algorithm (GA) optimization was deployed to optimize the patterns of the phase shifters for enhancing the peak gains at both frequency bands. The optimization was conducted independently for each band using the following procedure. The initial population for the GA process consisted of 50 individuals which were represented by binary strings. One of the individuals was the derived Fresnel pattern and the rest were

randomly generated. Each phase state was represented as a gene encoded into two states, "0" and "1". At each generation of the GA optimization, a crossover operation with 90% probability and a 5%-probability mutation operation were applied, and a new pattern of the phase shifters was generated, which was used to calculate the peak gain based on the equivalent electric and magnetic current method [92]. Finally, the phase shifter patterns with maximum peak gain at both frequency bands derived at the end of the GA process were used to construct a physical model of the dual-band reflectarray.

2.4 Simulation and Measurement Results

Three different reflectarray prototypes that utilize the proposed dual-band unit cell were designed. The prototypes were designed to showcase the versatility of the proposed unit cell in designing different types of static reflectarrays. The first prototype was designed to use a center feed and generate beams directed towards broadside at both bands. The second prototype was designed to have center feeds but generate X and Ku-band beams that are directed towards different directions. Specifically, the X-band beam is directed to $\theta = 45°$, $\phi = 0°$ and the Ku-band beam is directed towards $\theta = 45°$, $\phi = 180°$. The third prototype was designed to collimate the beams at broadside direction at both bands with offset feeds. For the case with offset feeds, the two feed antennas were positioned to create the same oblique angles of incidence of 20° in the x–z plane but with opposite x coordinate values. Each of these prototypes demonstrates in its own way the significance of having independent phase control in each frequency range. I followed the design procedure mentioned in the previous section to derive the optimized Fresnel patterns for the lower- and higher-band phase shifters for each reflectarray prototype. These patterns are shown in Fig. 2.9.

Observe that even for the simplest case of a center-fed reflectarray with beams collimated towards broadside, the Fresnel patterns needed for beam collimation are different at the two different frequencies. To implement such Fresnel patterns, each spatial phase shifter

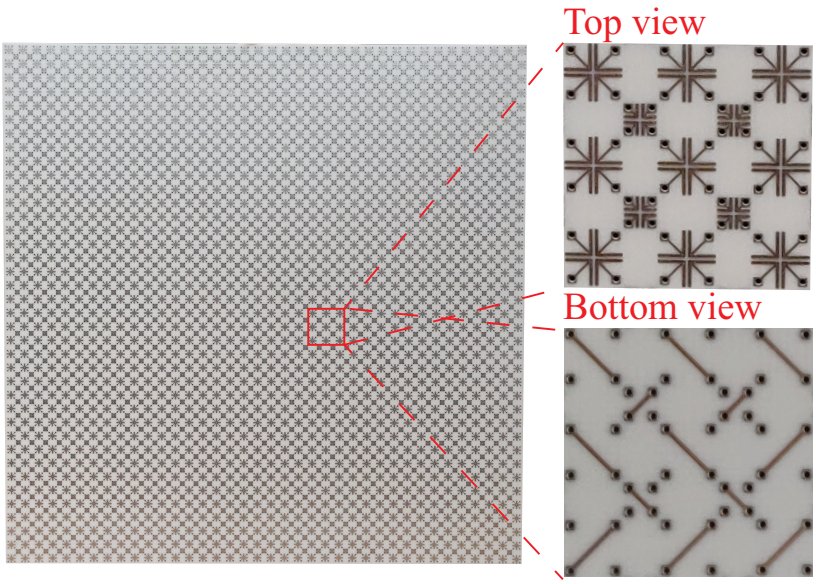

Figure 2.10: Photographs of one of the fabricated reflectarray prototypes.

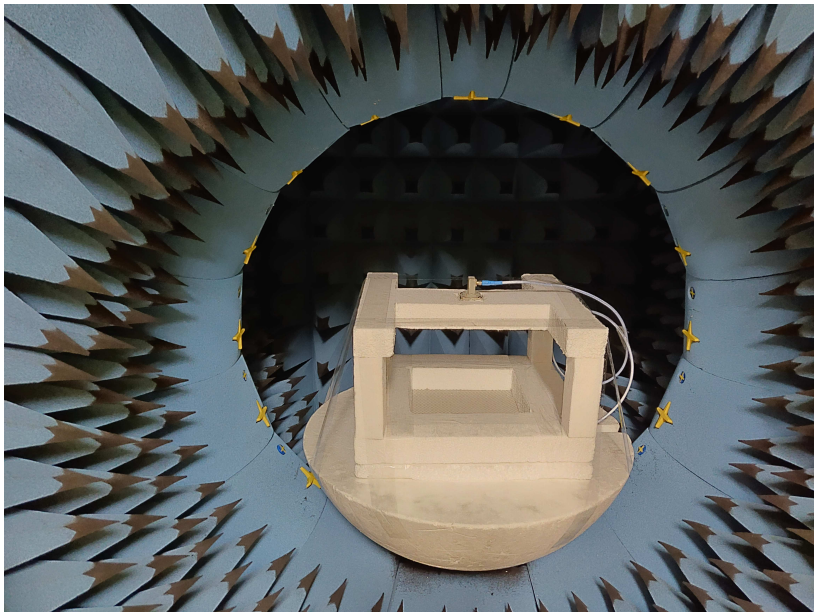

Figure 2.11: Radiation pattern measurement setup.

must be capable of providing independent phase shift at each operating frequency. This independent phase control feature becomes even more important when offset feeds are used or when the two beams are to be directed towards different directions. This latter case may be necessary in fixed point-to-multi-point communications links that operate at different frequency bands. Based on the phase-shifter patterns, I modeled the physical structures of

the three reflectarrays in full-wave simulations. For each reflectarray prototype, one feed antenna (out of two) was used at a time to simulate the response at the respective operating band. A total of six full-wave simulations were conducted to predict the performances of the three prototypes at both operating frequency bands. In each full-wave simulation, the complete physical structure of the feed horn antenna was modeled to ensure that he feed blockage effect is considered in predicting the radiation patterns of the reflectarray antennas. In order to quantify the feed blockage effect of the horn antennas, I conducted extra full-wave simulations for the first prototype, where I used an equivalent field source to replace the horn antenna [40]. At 8.7 GHz, the peak gain for the simulations using equivalent field sources is 0.5 dB larger than the peak gain value obtained using physical horn antennas. The gain difference of 1.1 dB between the two cases is more significant at 15 GHz where the aperture blockage effect is more significant. The simulations also accounted for all ohmic and dielectric losses in the reflectarrays and the feed antennas. In all simulations, the simulated reflection coefficients at the inputs of the horn antennas were below -10 dB over the respective operating frequency bands, verifying good power delivery to each of the reflectarrays.

Subsequently, prototypes of each reflectarray design were fabricated. Each fabricated prototype was implemented on three Rogers RO4003C substrates bonded together by two layers of Rogers RO4450F. The overall dimensions of each prototype were 304 mm long, 304 mm wide, and 3.3 mm thick. The vertical vias connecting the top metallic layer with the bottom metallic layer were implemented with plated via holes with diameters of 0.46 mm. Fig. 2.10 shows a photograph of one of the fabricated reflectarray prototypes along with the zoom-in views for the top and bottom surfaces of the array. The interleaving arrangement of the higher-band and lower-band dipole clusters can be seen on the zoom-in portion of the top surface. The bottom view shows different strip orientations for realizing different operating states of the PRUCs. The fabricated reflectarray prototypes were experimentally characterized in a near-field measurement chamber, as shown in Fig. 2.11. Styrofoam fixtures were used to fix the reflectarrays and feed horn antennas at the desired positions and

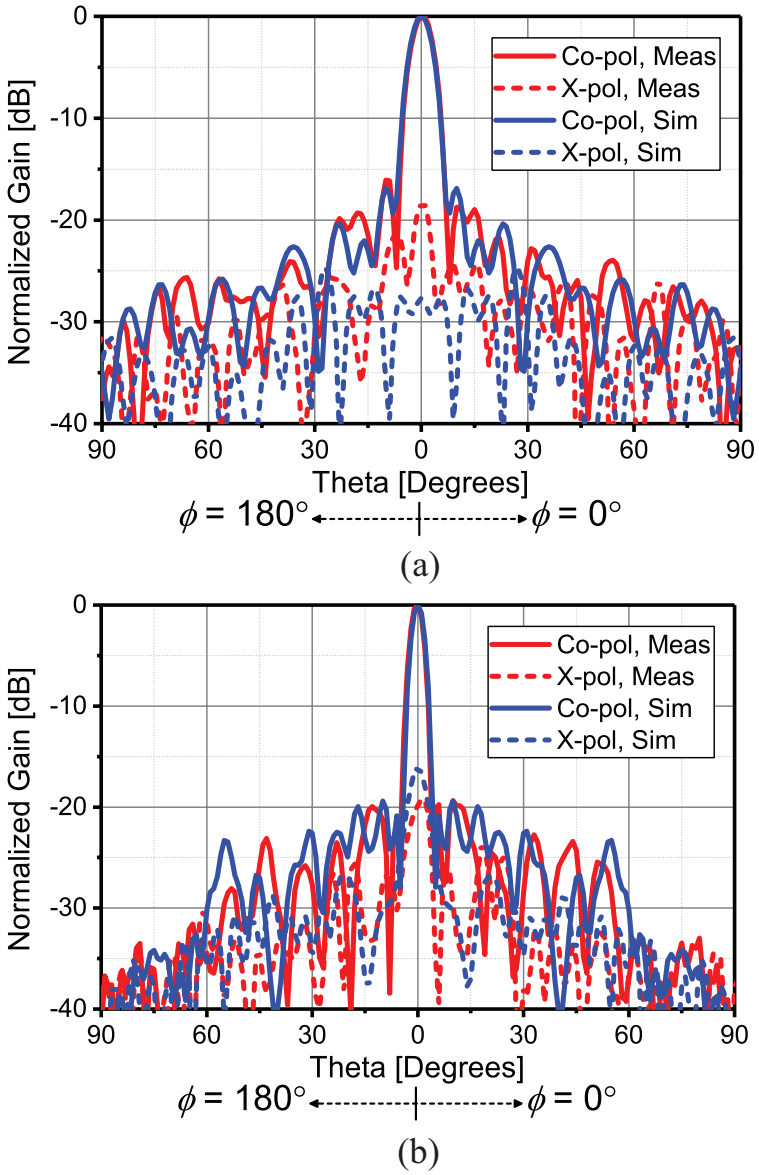

Figure 2.12: Simulated and measured normalized radiation patterns in the x–z plane for the reflectarray antenna designed to provide beam collimation at broadside direction with center feeds (Design 1) at (a) 8.7 GHz and (b) 15 GHz.

alignments during the measurements.

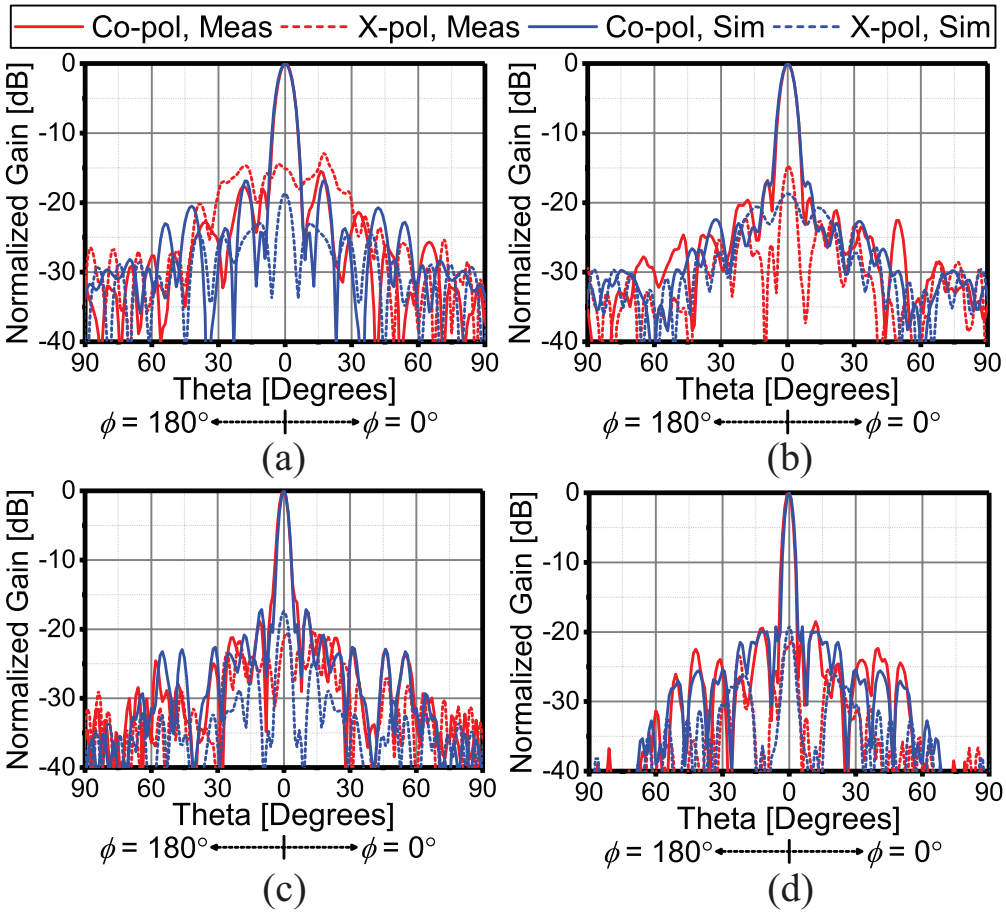

Figure 2.13: Simulated and measured normalized radiation patterns in the x–z plane for Design 1 at (a) 8.2 GHz, (b) 9.2 GHz, (c) 14.5 GHz, and (d) 15.5 GHz.

2.4.1 Design 1: Center-Fed With Broadside Beam Collimation at Each Band

Fig. 2.12 shows the simulated and measured normalized radiation patterns for Design 1 at 8.7 GHz and 15 GHz in the E-plane. Since the radiation patterns of the feed horn antennas are almost rotationally symmetric, the radiation patterns of the dual-band reflectarray antenna prototype are nearly identical in the E-plane and H-plane. Therefore, only the E-plane radiation patterns are presented for brevity. At 8.7 GHz, the measured realized gain at broadside direction is 23.3 dBi, corresponding to an aperture efficiency of 21.9%. These measured values agree well with the simulation results of 23.5 dBi maximum realized gain

and 22.9% aperture efficiency. At 15 GHz, the measured realized gain at broadside direction and corresponding aperture efficiency are 27 dBi and 17.3%, respectively, which are slightly smaller than the predicted values of 27.7 dBi for the realized gain and 20.3% for the aperture efficiency. The measured and simulated maximum side-lobe levels are -16.1 dB and -16.9 dB, respectively, at 8.7 GHz, and -19.7 dB and -19.3 dB, respectively, at 15 GHz. Fig. 2.13 shows the simulated and measured normalized radiation patterns for Design 1 at 8.2, 9.2, 14.5 and 15.5 GHz, respectively, in the E-plane. Both measurements and simulations show cross-polarization levels smaller than -14.5 dB at both bands. The measured and simulated maximum side-lobe levels are below -12.5 dB.

Fig. 2.14 reports the measurement and simulation results for the maximum realized gains as a function of frequency for Design 1. It can be seen that the simulated and measured 3-dB gain bandwidths for the lower band are both 7.9-9.5 GHz, corresponding to 18.7% bandwidth. For the higher band, the measured 3-dB gain bandwidth ranges from 14 GHz to 16.5 GHz (16.6%), while the simulated band of 13.9-16.5 GHz (17.3%) is slightly wider. The measured 3-dB gain bandwidths of this prototype agree well with the simulated 3-dB reflection coefficient bandwidths of the dual-band PRUCs reported in Section 2.2. Both measurements and simulations show maximum side-lobe levels of smaller than -12 dB within the operating frequency bands. While the simulations predict the trend in the variation of the peak gain with respect to frequency well, there are certain discrepancies between the gain values observed in the simulations and measurements. The average difference between the simulated and measured peak gains is 0.4 dB over the lower band and 0.7 dB over the higher band. These discrepancies can be attributed to fabrication tolerances, measurement uncertainties, and limited simulation accuracies. Any fabrication tolerances in the dimensions or alignments of the reflectarray structure would have more impact on the higher-frequency (and physically smaller) features, which may explain why the discrepancies are more pronounced at the higher band. Moreover, possible misalignment between the feed antennas and the reflectarray as well as some features in the measurement setup that were not taken

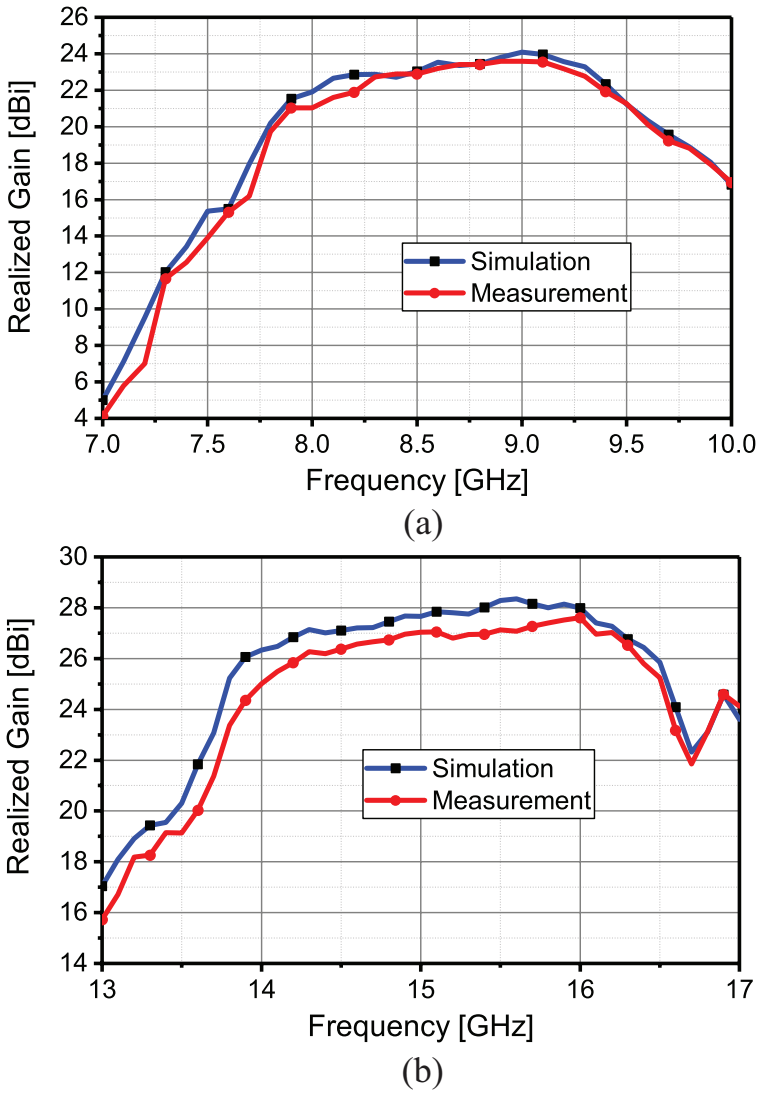

Figure 2.14: Simulated and measured maximum realized gains over the (a) lower band and (b) higher band of Design 1, which provides beam collimation at broadside direction with center feeds.

into account in the full-wave simulations, such as the cable connecting the feed horn and the test port of the measurement chamber, also contributed to the differences between the measurements and simulations.

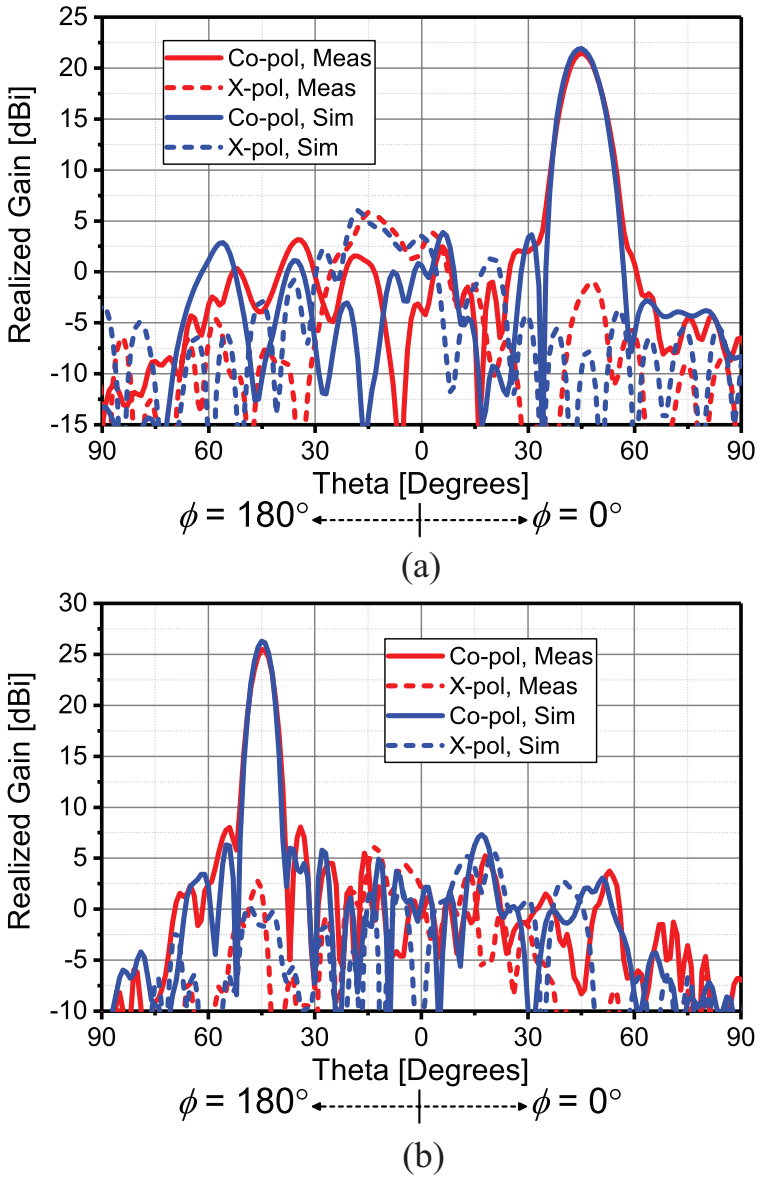

Figure 2.15: Simulated and measured radiation patterns in the x–z plane for the reflectarray antenna (Design 2) providing beam collimation at $\theta = 45°$, $\phi = 0°$ at lower band and $\theta = 45°$, $\phi = 180°$ at higher band with center feeds at (a) 8.7 GHz and (b) 15 GHz.

2.4.2 Design 2: Center-Fed With Different Beam Directions at Each Band

Fig. 2.15 shows the simulated and measured normalized radiation patterns in the E-plane for Design 2 providing beam collimation at $\theta = 45°$, $\phi = 0°$ at 8.7 GHz and $\theta = 45°$, $\phi = 180°$ at 15 GHz with center feeds. At 8.7 GHz, the measured peak gain and aperture efficiency

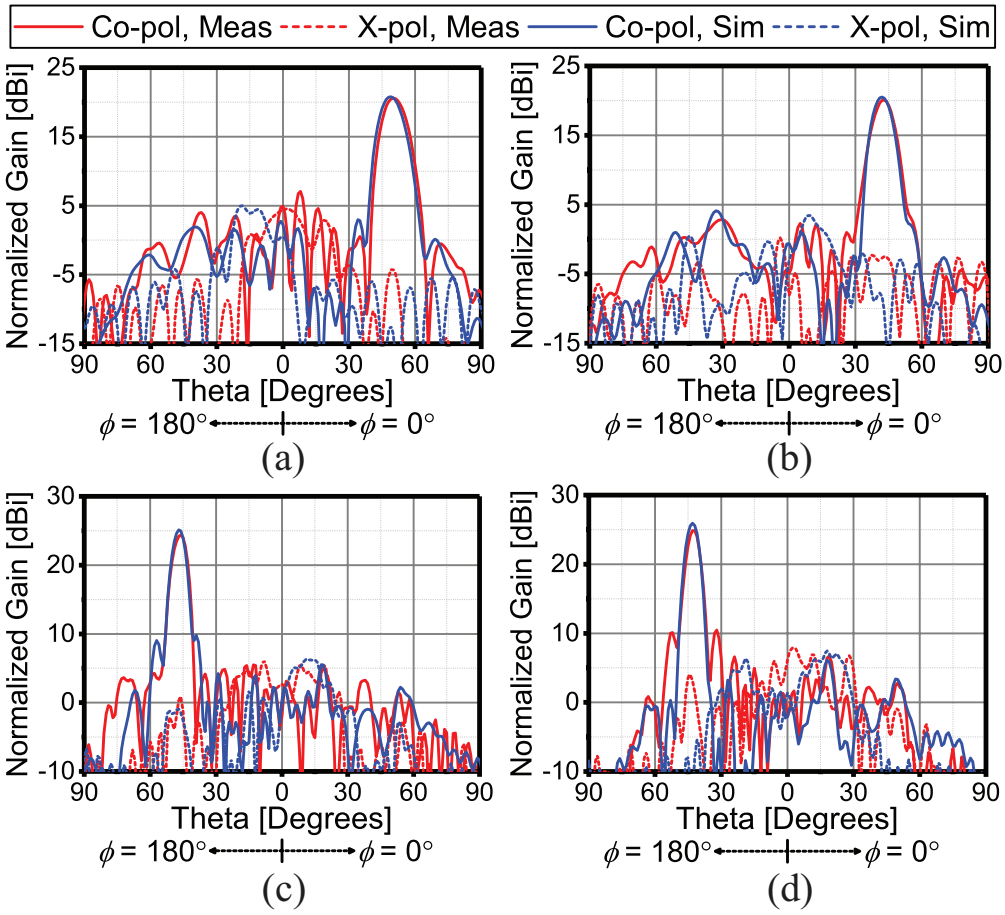

Figure 2.16: Simulated and measured normalized radiation patterns in the x–z plane for the reflectarray antenna (Design 2) at (a) 8.2 GHz, (b) 9.2 GHz, (c) 14.5 GHz, and (d) 15.5 GHz.

are 21.5 dBi and 20.5%, respectively. These measured realized gain and aperture efficiency results are sightly lower than the simulated values of 21.9 dBi and 22.4%, respectively. At 15 GHz, the measured and simulated maximum realized gains are 25.5 dBi and 26.3 dBi, which are equivalent to aperture efficiencies of 17.3% and 20.8%, respectively. Compared to Design 1 with a broadside beam, the measured peak gains are reduced by 1.8 dB at 8.7 GHz and 1.5 dB at 15 GHz. The measured and simulated side-lobe levels are below -18.2 dB and -18 dB, respectively, at 8.7 GHz, showing very good agreement. At 15 GHz, the measured maximum side-lobe level of -17.4 dB is slightly higher than the simulated value of -19 dB. Additionally, measured and simulated polarization purities are all better than 22.5 dB in

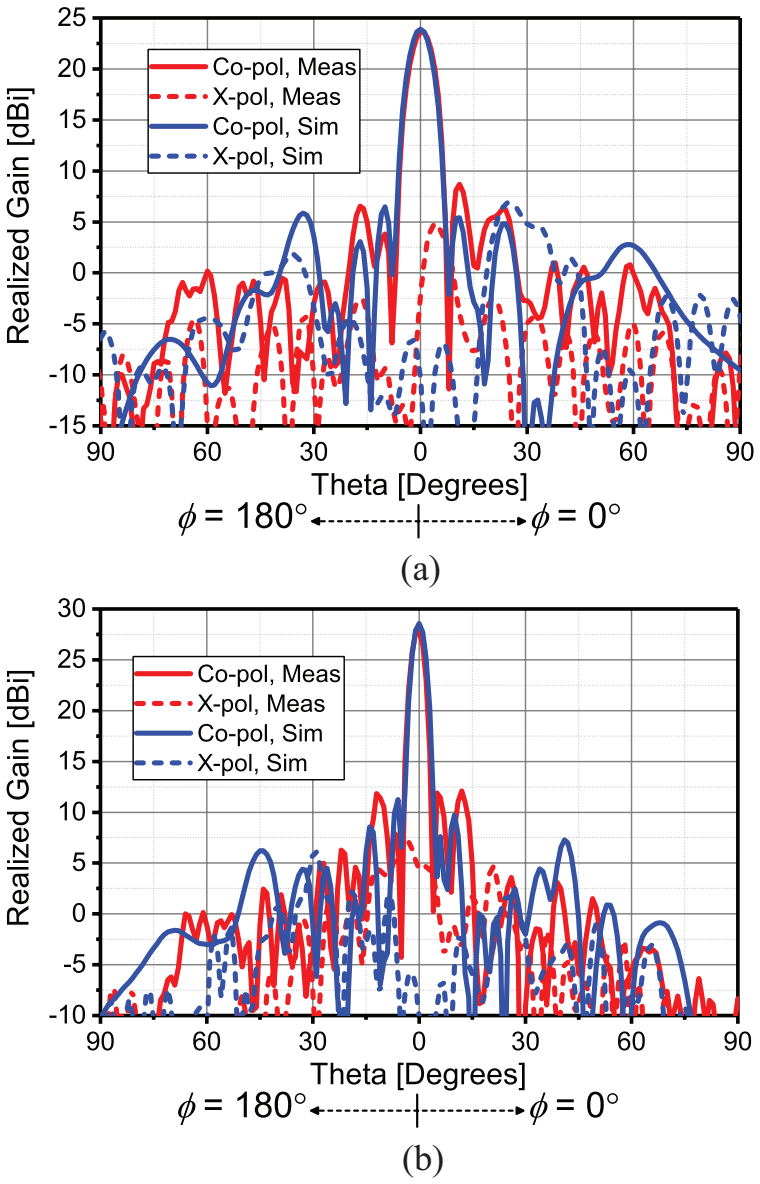

Figure 2.17: Simulated and measured radiation patterns in the x–z plane for Design 3. The reflectarray antenna provides beam collimation at broadside direction with offset feeds at (a) 8.7 GHz and (b) 15 GHz.

the main beam directions at both bands. Overall, the simulation and measurement results agree well in terms of side-lobe and cross-polarization levels.

Fig. 2.16 shows the simulated and measured normalized radiation patterns for Design 2 at 8.2, 9.2, 14.5 and 15.5 GHz, respectively, in the E-plane. The simulation and measurement results still agree well. The simulated and measured peak gain differences are less than

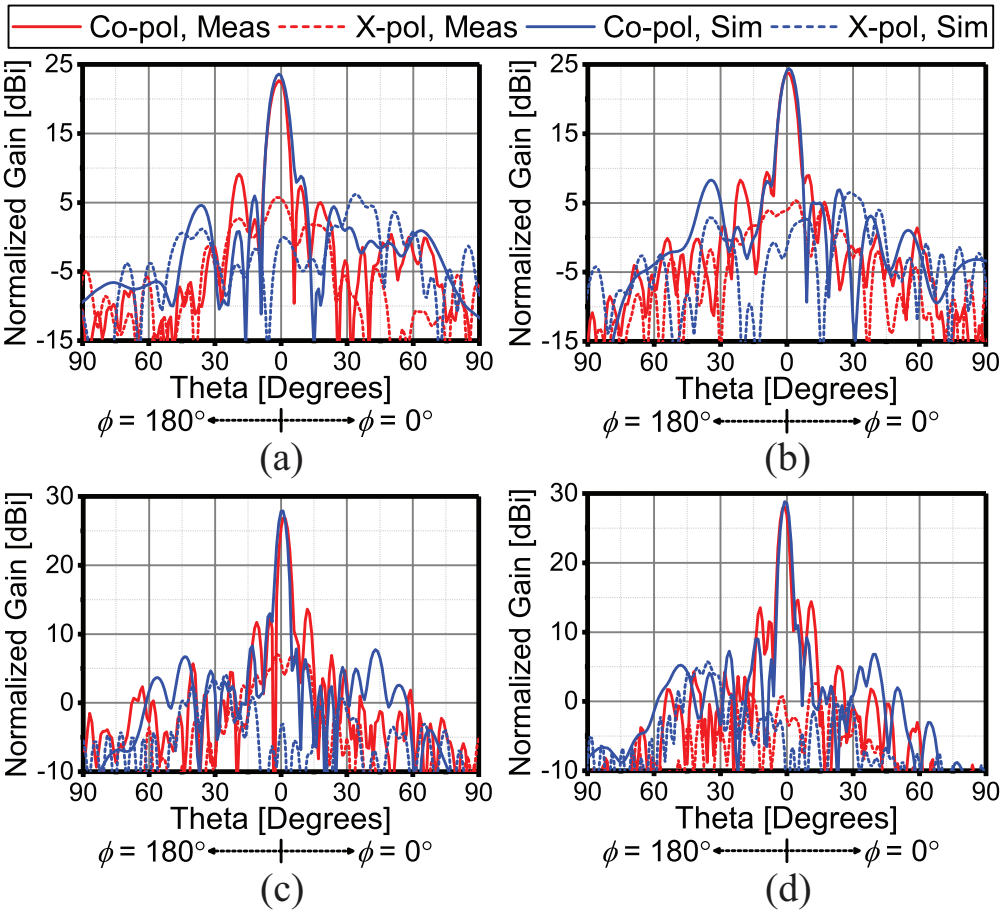

Figure 2.18: Simulated and measured normalized radiation patterns in the x–z plane for Design 3 at (a) 8.2 GHz, (b) 9.2 GHz, (c) 14.5 GHz, and (d) 15.5 GHz.

0.3 dB at the lower band and 0.7 dB at the higher band, respectively. The measured and simulated maximum side-lobe levels are below -15 dB. Both measurements and simulations show polarization purities better than 20 dB at both bands.

2.4.3 Design 3: Separate Offset-Feds With Broadside Beam Collimation

Figs. 2.17(a) and 2.17(b) show normalized radiation patterns in the E-plane for Design 3 at 8.7 GHz and 15 GHz, respectively. The measured realized gain at broadside direction is 23.6 dBi at 8.7 GHz, corresponding to an aperture efficiency of 23.5%. These measured values are slightly lower than the simulated peak gain of 23.9 dBi and simulated aperture efficiency

of 25.1%. The discrepancies between the measurements and simulations are more noticeable at 15 GHz as the measured peak gain of 27.8 dBi is 0.8 dB lower than the simulated value. The corresponding aperture efficiencies calculated from the measured and simulated gains are 20.8% and 25%, respectively. The measured maximum side-lobe levels are -14.9 dB at 8.7 GHz and -15.7 dB at 15 GHz, while the simulated results are -17.4 dB at 8.7 GHz and -17.3 dB at 15 GHz. The maximum normalized cross-polarization levels recorded in the measurements are -18.8 dB at 8.7 GHz and -20.6 dB at 15 GHz, while the simulated results are -17.0 dB at 8.7 GHz and -21.5 dB at 15 GHz. I also added four frequencies points, 8.2, 9.2, 14.5 and 15.5 GHz, of the simulated and measured normalized radiation patterns for Design 3 in the E-plane, as shown in Fig. 2.18. The discrepancies between the measured and simulated peak gains are within 1 and 1.1 dB for lower band and higher band frequency points, respectively. Both measurements and simulations show cross-polarization levels of smaller than -16 dB at these frequencies. The measured and simulated maximum side-lobe levels are all below -13 dB.

Table 2.2: Comparisons between the performances of Design 1 and Design 3, which provide broadside collimated beams with center (Design 1) and offset (Design 3) feeds.

Scenarios	Center feed 8.7 GHz	Offset feed 8.7 GHz	Center feed 15 GHz	Offset feed 15 GHz
Simulated Gain [dBi]	23.5	23.9	27.7	28.6
Measured Gain [dBi]	23.3	23.6	27.0	27.8
Simulated SLL [dB]	-16.9	-17.4	-19.3	-17.3
Measured SLL [dB]	-16.1	-14.9	-19.7	-15.7

Table 2.2 compares the maximum realized gains and side-lobe levels for the two designs providing broadside beam collimation but with different feed placements (Design 1 with center feeds and Design 3 with offset feeds). The measured peak gains for the design using offset feeds are 0.3 dB larger at 8.7 GHz and 0.8 dB larger at 15 GHz compared to those of the one using center feeds. This agrees well with the simulation prediction that Design 1 provides 0.4 dB higher and 0.9 dB higher gains than Design 3 at the lower and higher bands,

Table 2.3: Comparisons between the proposed design and other dual-band reflectarrays reported in the literature.

Ref.	Freq. bands	Aperture size [mm]	Aperture efficiency	f/D	1-dB bandwidth	Independent beam control	Grating lobes	Pol.
This work	X/Ku	304, Square	24%, 21%	0.80 both	11.5%, 10.0%	Yes	No	Dual-pol.
[78]	X/K	280, Circular	47%, 25%	0.64, 0.87	16.0%, 9.1%	No	Yes at K band	Linear
[82]	X/K	300, Circular	63%, 42%	1.27 both	25.0%, 18.0%	Yes	Yes at K band	Linear
[84]	X/K	400, Circular	58%, 61%	0.90 both	9.1%, 14.0%	No	No	Dual-pol.
[87]	K/Ka	403 × 249, Elliptical	29%*, 14%*	0.88 both	2.2%, 2.9%	Yes	No	Dual-circular

*Calculated from the data provided in the paper.

respectively. The higher gains associated with using the offset feeds are partly attributed to the reduction of aperture blockage caused by the feed antennas. The gain difference is more significant at the higher band where the aperture blockage effect of the centrally placed, Ku-band feed horn antenna is more pronounced. However, the side-lobe levels for the prototype using offset feeds are generally higher than the side lobe levels for the prototype using center feeds.

I compared my design with other dual-band reflectarrays reported in the literature to highlight the advantages of the proposed approach. Table 2.3 compares several key parameters of these dual-band reflectarrays. Careful examination of Table 2.3 reveals that the proposed reflectarray design has four important features, the *combination* of which is not available from the other competing designs reported in Table 2.3. These include: 1) The ability to provide independent phase shift and beam control at each band; 2) Avoiding the excitation of any grating lobes for large beam scan angles or large feed offset angles; 3)

Ability to support dual-linear or dual-circular polarization simultaneously at each band; and 4) Having moderately wide (>10%) bandwidth at each band. None of the other designs reported in Table 2.3 possess all of these characteristics in a single design. This demonstrates the advantages of the proposed PRUC design as a building block of dual-band reflectarray antennas. One disadvantage of the current design compared to those reported in [78, 82, 84] is its lower aperture efficiency. This is most likely a consequence of using 1-bit phase quantization in my design, which is known to cause more than 3 dB gain loss compared to reflectarrays that use continuous spatial phase shifters [42, 89]. Reflectarray unit cells with 1-bit phase quantization, similar to those reported in this work, have been used in designing electronically reconfigurable reflectarrays before. For such applications, the reduction in the aperture efficiency caused by 1-bit phase quantization may be an acceptable design trade off as it drastically reduces the implementation complexity of these systems.

2.5 Conclusions

This chapter presented a dual-band spatial phase shifter that operates based on the polarization rotation concept and provides 1-bit phase quantization. This polarization-rotating unit cell is capable of providing independent phase control at each band of operation and has unit cell dimensions smaller than half a wavelength at the highest frequency band of operation. These features are important in designing center- and offset-fed reflectarray antennas or reflectarray antennas that have fixed beams pointed towards different directions at each band.

Having independent phase control at each band ensures that the different optimum Fresnel patterns needed for efficient beam collimation at each band can be implemented. I demonstrated that this feature is needed even in center-fed reflectarrays with broadside beam collimation at each band. Small unit cell dimensions ensure that no grating lobes is excited if the reflectarray design requires offset feeds or beams directed off broadside (or

both). The proposed PRUC provides dual-band operation by diagonally interleaving two similar polarization-rotating structures with different physical dimensions. Simulation results for four operating states of the illustrative PRUC demonstrate polarization rotation operation at X and Ku bands with independent 1-bit phase shift control at each band. I used the PRUC to design three different fixed-beam reflectarray antennas to showcase the importance of having independent phase shift control and small unit cell dimensions even in static reflectarray antennas. Prototypes of each of these three different designs were fabricated and experimentally characterized. Measurement results of the reflectarray design that provides broadside beams at both bands and uses center feeds shows 3-dB gain bandwidths of 18.7% and 16.6% for the lower and higher bands, respectively. The reflectarray design that provides beams along the $\pm 45^{\circ}$ direction while using a center feed shows a lower gain (by 1.8 dB at 8.7 GHz and 1.5 dB at 15 GHz) compared to the gain of the first prototype. Maximum aperture efficiencies of 23.5% at the lower band and 20.8% at the higher band were observed for the fabricated prototype generating broadside beams at both bands with offset feeds. Overall, the measurement results agree well with the simulation results for the three designs, demonstrating the performance and suitability of the proposed dual-band reflectarray unit cell for a wide range of designs with different characteristics.

Chapter 3

A Wideband, 1-Bit, Electronically Reconfigurable Phase Shifter for High-Power Microwave Phased-Array Applications

3.1 Introduction

Modern high-power microwave (HPM) technologies have received considerable interest in applications ranging from electronic warfare, high-power radars, satellite and airborne communications to next-generation unmanned systems. In such applications, it is often required to radiate extremely high-power levels from an antenna aperture. These power levels can range from tens of kilowatt on the lower end to Gigawatt peak power levels on the higher end. Moreover, it is often desirable to have high-gain antennas whose beams can be rapidly steered towards the desired direction. These requirements have demanded and motivated innovations for the development of phased-array antennas that can be used in HPM applications [93–96]. In addition to the high-power requirement, many applications such as radar or electronic warfare systems also require the phased-array antennas having wide bandwidths to be able to accommodate different types of sources and/or dynamic radiated waveforms. The simultaneous requirements of high radiated power levels, wide bandwidths, and rapid electronic beam-steering are extremely challenging to meet with many existing phased-array design approaches. This is particularly the case in active phased-array architectures [2], in which individual transmit/receive modules are integrated with each radiating element of the array. In such cases, the wide bandwidth requirements of the system result in PA operating in low-efficiency regimes, thereby limiting the average radiated power. Furthermore, the lower PA efficiency results in generation of significant heat that must be efficiently dissipated from the aperture. These challenges are motivating factors for development of less complex, high-power-capable, wideband, passive phased array antennas that can be excited with one or a few HPM sources such as vacuum electronics amplifiers or oscillators.

Phase shifters not only are critical components in any phased-array system (arguably the most important component) but also represent a considerable portion of the overall cost of passive phased-array antennas [14]. Therefore, a low-cost, high-power-capable, wideband phase shifter is a vital component of any high-power, wideband phased-array antenna, espe-

cially for electrically large phased arrays. Examples of phase shifter technologies studied to address this issue include those using MEMS [15–17], ferrite [18–21], ferroelectric [21], and semiconductor-based technologies [22–24]. RF MEMS phase shifters are capable of working over wide frequency bands [17]. However, they have limited power handling capability (few Watts) and typically need high-voltage drive circuits. Ferrite-based phase shifters offer high-power handling capability (few kW) and low-loss over moderate bandwidths (around 20%), but they are bulky and consume high dc power levels [18–21]. Semiconductor-based phase shifters can offer wide bandwidths (40% in [23], 66.7% in [24]), but their power handling capabilities are usually limited to a few Watts. Besides, they also tend to have a higher losses with typical values of 2 dB/bit. Finally, mechanically reconfigurable passive arrays have demonstrated peak power handling capabilities in the order of several MW [25, 26], albeit at the expense of high cost and weight, significantly reduced beam-scanning speeds and bandwidths. PIN diode switches have been commonly used in designing spatial phase shifters in transmitarrays and reflectarrays [33, 38, 39, 43]. Generally, they have a high linearity and can be designed to handle high RF power levels. PIN diodes have relatively low cost and fast switching speeds ranging from several nano seconds to micro seconds. Thus, they are good candidates for use in designing electronically-reconfigurable devices operating at high-power levels.

Recently, the concept of PR has been exploited as a promising solution to design wideband spatial 1-bit phase shifters for use in transmitarrays [33, 35, 36] and reflectarrays [37–43, 97]. In this chapter, I present the unit cell of a high-power-capable, ultra-wideband phase shifter based on the PR concept. The proposed polarization-rotating phase shifter can be used either in transmitarray or in a direct-fed passive phased-array architecture. The proposed PRUC provides 1-bit phase quantization capability and is designed to work over a very wide frequency band covering the 6-12 GHz range. In its current embodiment, the unit cell consists of a pair of orthogonal dipoles sandwiched by two orthogonal double-ridge waveguide sections. It can be excited either directly in the case of a direct-fed array or connected to

transmit/receive antennas for use in a transmitarray architecture. Two PIN diodes load the orthogonal dipoles and are used to control the direction of rotation of the polarization of the transmitted wave by 90° in either the clockwise or the counter clockwise direction. The unit cell has a dimension of 12×12 mm^2. Simulation results of the prototype show that it offers a wideband operation in the 6-12 GHz range, where the transmission coefficient $|T_{xy}| > -1$ dB and reflection coefficient $|R_{yy}| < -10$ dB. Multiphysics simulations were used to design the thermal management solution and study the average power handling capability of the device. These simulations suggest that the average power handing capability of the device exceeds 34 W, or 23.6 W/cm^2, across the whole frequency band. This is equivalent to a radiated CW power density of 236 kW/m^2 from the antenna aperture. I fabricated and experimentally characterized a prototype of the proposed PRUC at low and high power levels. High-power experiments were conducted under CW and pulsed operation modes to determine the average and peak power handling capabilities of the device. These experiments demonstrate that the device has a CW power handling capability better than 34 W[1] over the entire frequency band of operation and has a peak power handling capability of 500 W, equivalent to 347 W/cm^2, at 9.382 GHz. This peak power handling capability translates to a power density of 3.47 MW/m^2 from the antenna aperture. The phase shifter studied in this chapter achieves three important attributes simultaneously. These attributes include: 1) Very-high-power handling capability of 34+ W (23.6+ W/cm^2) average power and up to 500 W (347 W/cm^2) peak power per element; 2) Very wide operating bandwidth of one octave (6-12 GHz); and 3) Rapid electronic switching capability with 1-bit phase quantization. The combination of these attributes are not currently available from previously-reported phase shifters. This suggest that the proposed PRUC is suitable for use in developing high power microwave, electronically beam-steerable, phased-array antennas.

[1]The power level at which CW experiments were conducted was limited to 34 W because of the limitations of the test setup. It is expected that the CW power handling capability of the device is higher than 34 W but this could not be experimentally verified.

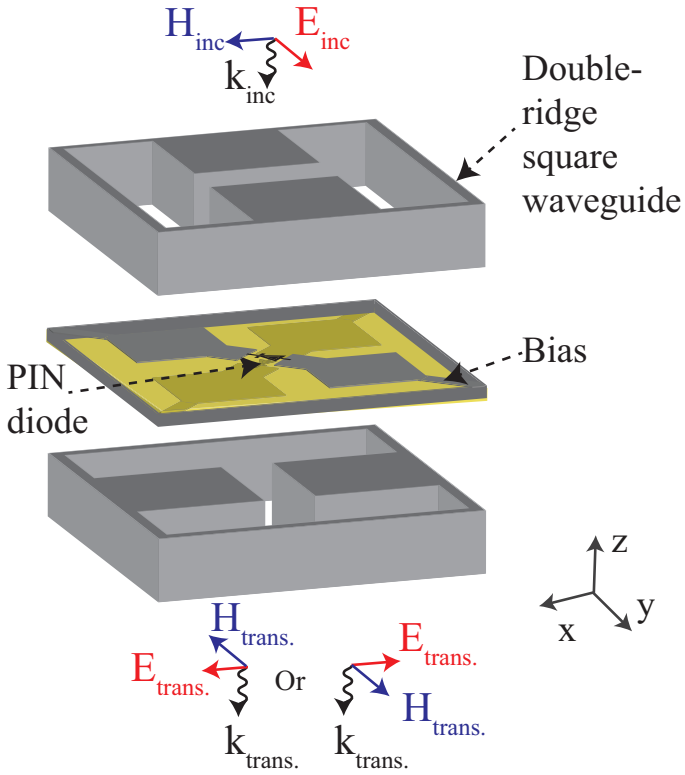

Figure 3.1: The 3D view of the proposed PRUC.

3.2 Unit Cell Design and Simulations

Fig. 3.1 shows the 3D view of the proposed PRUC. I envision that the PRUC may be used either in a high-power transmitarray architecture or in a high-power, direct-fed, phased-array architecture. Fig. 3.2 shows the corresponding two embodiments. I envision that in the transmiatarray architecture (shown in Fig. 3.2(a)), the proposed PRUC can be used as a spatial phase shifter. In such an operating mode, the ridges of the input/output DR waveguide will be tapered to facilitate the task of impedance matching the PRUC to free-space. Another architecture in which the proposed PRUC is likely to be used is a direct-fed, high-power phased-array (see Fig. 3.2(b)). In this embodiment, I envision that the output DR waveguide of each PRUC transitions to a DR horn with the same aperture dimensions as those of the DR waveguide. This converts the PRUC to a small-aperture DR horn antenna with 1-bit electronic phase switching capability. Such an antenna constitutes an element of a

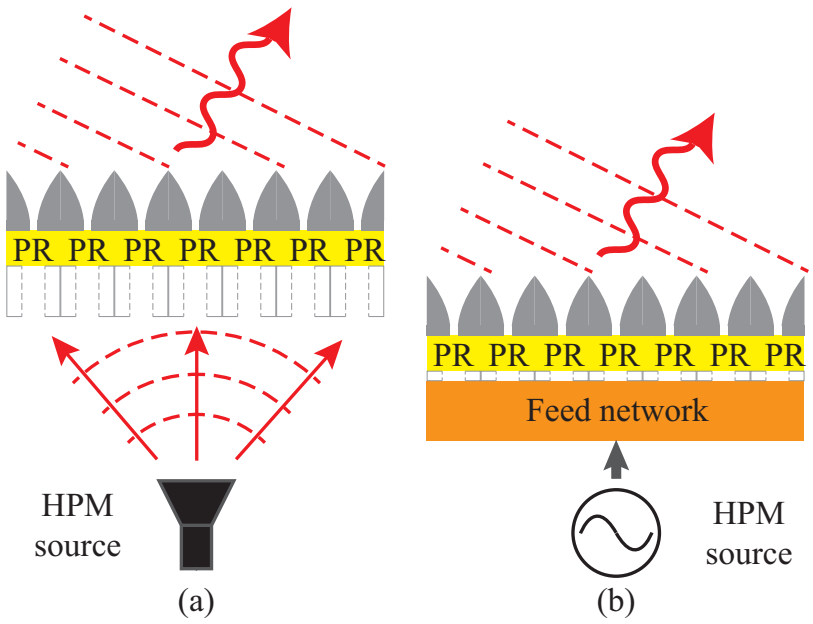

Figure 3.2: Two embodiments that the proposed PRUC can be used in. (a) High-power transmitarray using the proposed PRUC as spatial phase shifters. (b) High-power, direct-fed, phased array using the proposed PRUC as high-power 1-bit phase shifters.

passive phased-array fed with its own dedicated feed networks and a single high-power source (e.g., a vacuum electronics amplifier or oscillator). In such a direct-fed architecture, a random phase shift, implemented with a delay line section of the DR waveguide, can be incorporated with each element. This will be used to suppress the grating lobes that will be excited due to 1-bit phase quantization, if all array elements are excited with the same phase [98, 99]. In either phased-array embodiment, the proposed high-power-capable PRUC plays a key role and is the main sub-system that limits the power handling capability of the phased-array. Therefore, the focus of the remainder of this chapter is solely on the design, optimization, and experimental characterization of the proposed high-power-microwave-capable wideband phase shifter at both low- and high-power levels.

Fig. 3.1 shows the topology of the high-power-capable, electronically reconfigurable 1-bit unit cell proposed in this work. The unit cell consists of three parts, two orthogonal DR waveguides and two dipole structures oriented in the $\pm 45^{\circ}$ directions. The cross dipole pair acts as a coupling mechanism between the two orthogonal DR waveguides to rotate

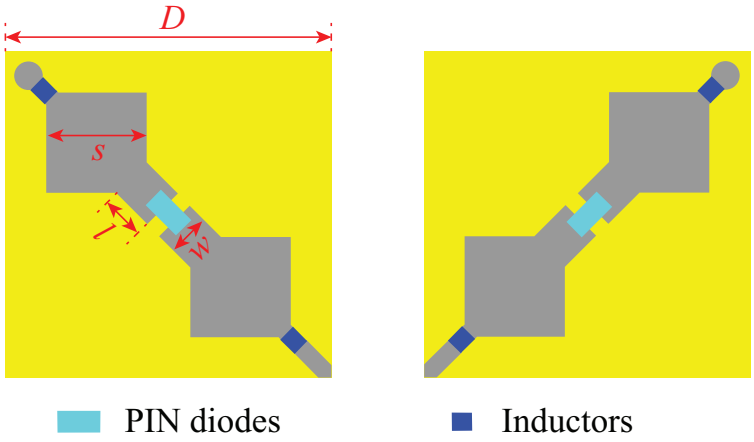

Figure 3.3: The top and bottom views of the middle dipole layer used in the construction of the PRUC. Yellow represents AlN substrate. Grey represents copper. Feature dimensions (in mm) of the dipole structure are as follows: $D = 12$, $s = 3.75$, $w = 1.2$, $l = 1.36$.

the polarization of the transmitted wave by $+90°$ or $-90°$. The DR waveguide sections are used to both broaden the operating bandwidth of the device and to serve as efficient heat-sinks for cooling the device when operated under high average power conditions. The unit cell receives an electromagnetic field whose electric field is normal to the ridges of the first DR waveguide. The coupling dipoles are oriented with an angle of $+45°$ or $-45°$ with respect to the polarizations of the incoming and outgoing waveguides. Therefore, they can efficiently couple the energy from one waveguide to another and in the process result in polarization rotation. An important feature of the PRUC is the ability to control the direction of the polarization rotation (e.g., clockwise or counterclockwise), which depends on the arrangement of the dipoles in the middle layer. Fig. 3.1 shows the unit cell design, where the dipoles of the middle-layer are orthogonal to each other. Each dipole is loaded with a PIN diode at its center. When the PIN diode is ON, the two halves of the dipole are connected to each other and the dipole is active. When the PIN diode is OFF, the dipole is inactive. In the normal operation mode of the PRUC, one of the dipoles is always active and the other one is inactive. Switching the active dipole results in rotating the polarization of the wave in the other direction, thereby changing the phase shift from $0°$ to $180°$ or vice versa. This results in the 1-bit polarization-rotating design. One end of each of the dipoles

is dc connected to the body of the DR waveguide to simplify the biasing of the PIN diodes. The other side is dc connected to the dc bias source that provides the forward or reverse bias voltage.

Fig. 3.3 shows the front and back views of the middle dipole structure of the PRUC. The unit cell has an aperture size of 12×12 mm^2, not including the wall thicknesses of the DR waveguides. Each PIN diode functions as a SPST switch with the ON and OFF states controlled by the corresponding forward and reverse bias states. The two PIN diodes always have reversed polarities with respect to each other. When one diode is forward biased, the other one is reverse biased, and vice versa. This determines the two operating states of the unit cell, which rotate the polarization of the transmitted wave by $+90^\circ$ and -90° with respect to those of the incident, linearly-polarized waves. Four lumped inductors are used to for RF/dc isolation.

I used a PIN diode manufactured by MACOM (model number MA4SPS502) and lumped inductors with an inductance value of 4.3 nH for RF/dc isolation (Coilcraft 0402DC-4N3X). These components were modeled as equivalent circuits of lumped elements in unit-cell simulations to take into account their ohmic losses and reactive effects. Specifically, the reverse-biased diode is modeled with a 0.078 pF capacitor in series with a 0.1 nH inductor. In the forward bias state, the diode is modeled as a resistor of 2.4 Ω in series with an inductor of 0.1 nH. These values were obtained through the measurement of the diode response over a wide bandwidth and extracting its equivalent circuit parameters. In this work, I used forward bias voltages of 1.2 V to control the PIN diode. The dc current for forward biasing the PIN diode is about 100 mA. The resistance of the forward-biased diode is a source for ohmic loss as RF currents flow through the diode.

The PRUC was designed to operate over an octave bandwidth ranging from 6 - 12 GHz. The middle dipole layer was implemented using a 0.63-mm thick Aluminum Nitride (AlN) ceramic substrate with a dielectric constant of 7.5 at 1 GHz. AlN ceramic substrate was used due to its high thermal conductivity of 170 W/mK. This facilitates the cooling of the

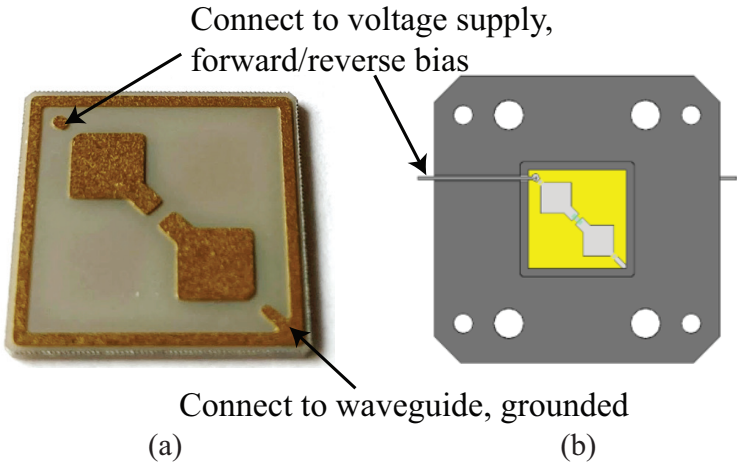

Figure 3.4: (a) Photograph of the fabricated dipole layer on the AlN substrate. (b) Topology of the waveguide shim used to supposed the middle dipole layer and provide dc bias paths to bias the PIN diodes.

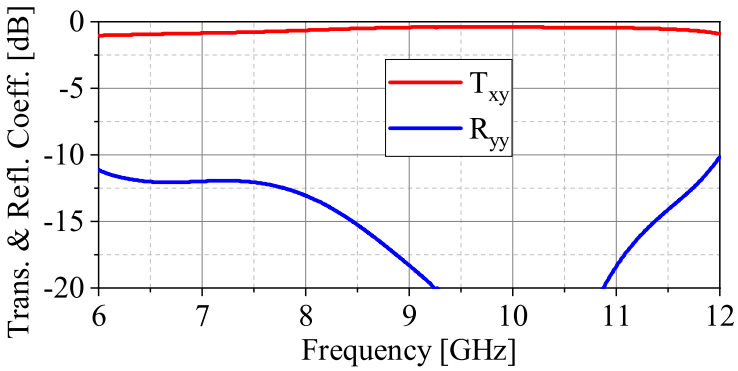

Figure 3.5: The simulated transmission and reflection coefficients of the proposed PRUC.

PRUC and the PIN diode junction when it operates under high average power conditions (see Section 3.3). The fabricated dipole structure is shown in Fig. 3.4. I also designed a waveguide shim for fixing this structure inside the DR waveguides. The waveguide shim also offers paths for the wires used to connect the dipoles to the dc bias source. One end of each dipole structure is always connected to the body of the DR waveguides, which are connected to ground when conducting the experiments. The other end is connected to a forward bias voltage of 1.2 V or a reverse bias voltage ranging from 0 V to 10 V depending on the RF power applied to the PRUC.

The PRUC was modeled and simulated with periodic boundary conditions in CST Mi-

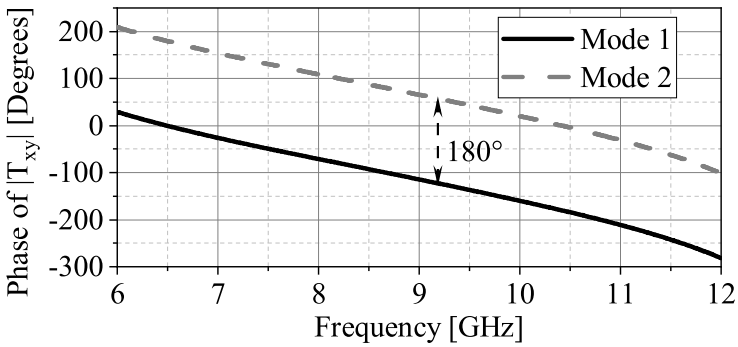

Figure 3.6: The simulated transmission phase of the two modes of the proposed PRUC.

crowave Studio. In the unit cell simulations, the PIN diodes (in forward and reverse bias) and the inductors were modeled with corresponding equivalent circuits of lumped components (inductors, resistors, and capacitors). These unit cell simulations took into account the ohmic and dielectric losses of all materials as well as the ohmic losses of the PIN diodes and those of the inductors. Fig. 3.5 shows the magnitudes of the simulated transmission, T_{xy}, and reflection coefficients, R_{yy} of the bit-0 unit cell, which are exactly the same as those of the bit-1 unit cell. The unit cells provide a good polarization rotation operation over a frequency range of 6-12 GHz, where $|T_{xy}| > -1$ dB and $|R_{yy}| < -10$ dB. Fig. 3.6 shows the phases of T_{xy} for two modes of the reconfigurable PRUC. The two modes provide a phase difference of 180° over the whole frequency range of 6-12 GHz. This suggests that the device can achieve an octave bandwidth, corresponding to 66.7%.

3.3 Thermal Design and Simulations

Thermal issues are one of the main factors that limit the average power handling capability of a microwave device. Therefore, developing a good thermal management solution and evaluating its performance is critical in devices subjected to high average power levels such as the proposed PRUC. To ensure that the maximum junction temperature of the PIN diode does not exceed the maximum rated temperature ($175°C$), I need to ensure that the heat generated within the PIN diode can be efficiently dissipated. Thus, an AlN ceramic substrate

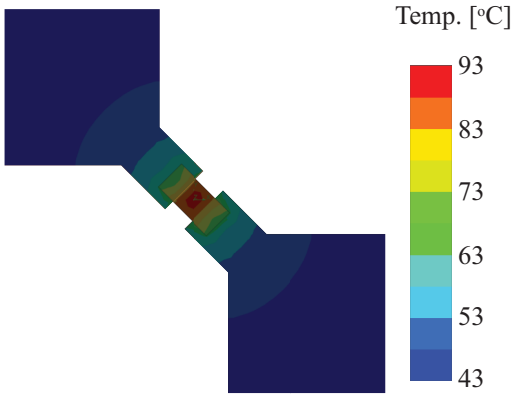

Figure 3.7: The simulated temperature distribution of the dipole structure when the diode is forward biased.

with a high thermal conductivity of 170 W/mK is used to accommodate the two orthogonal dipoles. The AlN substrate is thermally connected to the body of the waveguide offering a path with low thermal resistivity and allowing the body of the waveguide to act as an efficient heat sink. Moreover, forced-air cooling is used to enhance the efficiency of heat dissipation from the junctions of the PIN diodes. A pair of circular holes with diameters of 4 mm are used to implement the inlets and outlets for the forced-air cooling system in each waveguide. Each pair of holes are arranged perpendicular to the waveguide ridges. The diameter of the hole was optimized to enhance the air flow rate above the PIN diodes without deteriorating the RF performance. Four holes are used as the inlets and outlets of the forced-air cooling system.

In this work, my goal is to develop phased-array unit cells capable of handling an average input power density of 22 W/cm^2. This corresponds to an input power level of 50 W for a phased-array element using $\lambda/2 \times \lambda/2$ spacing at 10 GHz (or approximately a power level of 222 kW radiated from a 1 m^2 aperture). A power density of 22 W/cm^2 corresponds to an average power level of 32 W for the proposed PRUC with physical dimension of 12×12 mm^2. As a result, in the multiphysics simulations conducted in this section, an input power level of 32 W was used. Additionally, the inlets of the cooling system were assumed to supply air into the device with a pressure level of 15 psi, while both outlets were set to have ambient

pressure allowing for simplifying the design of the thermal management system. The RF losses predicted from CST Microwave Studio simulations were applied to thermal analysis as heat sources. Most of the RF losses are due to the ohmic loss caused by the resistance of the forward-biased PIN diode. The rest of the RF losses include the dielectric losses and ohmic losses due to the AlN substrate and waveguides. The thermal simulations were carried out by flow-simulation using SolidWorks, where the power handling capability of the proposed device was predicted and the efficacy of the thermal management solution was evaluated as well. As one can expect, the PIN diodes are most likely the main cause of failure and the main factor limiting the power handling capability of the PRUC. This further demonstrates the fact that the primary challenge in designing a high-power, electronically beam-steerable phased-array antennas is the development of high-power-capable, electronically-controllable phase shifters. Thus, the reliability of the PIN diodes employed in the present design should be ensured. Fig. 3.7 shows the simulated temperature distribution on the PRUC when forced air is circulated through the system with an inlet pressure of 15 psi at both inlets of the structure. The simulation result demonstrates that the highest temperature happens at the junction of the PIN diode, as expected. It also indicates that the maximum junction temperature within the PIN diode is $93^\circ\ C$, which is well below the maximum rated junction temperature of $175^\circ\ C$. Thus, these simulation result suggest that the device should be capable of handling the required input average power level of 32 W.

3.4 Fabrication and Low-Power Measurements

A prototype of the proposed PRUC was fabricated. The dipole section of the PRUC was implemented on a 0.63 mm AlN ceramic substrate. The waveguide shim and the input and output waveguide sections were fabricated out of aluminum using wire electrical discharge machining (EDM). Considering that the input/output DR waveguide sections are non standard, I fabricated DR waveguide transition sections that would allow for the use of

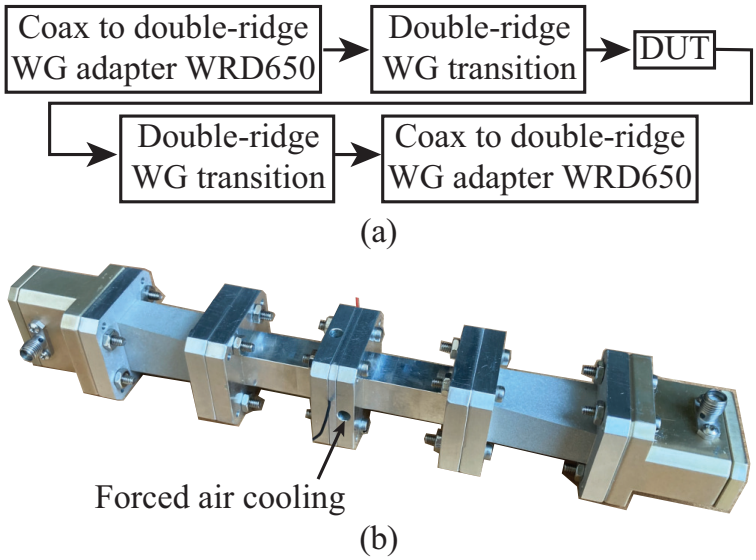

Figure 3.8: (a) The block diagram of the test fixture used to measure the response of the DUT including commercially-available coax to waveguide adapters WRD650, the transition section between the WRD650 waveguide and the custom-made DR waveguide used in the DUT, and the DUT. (b) Photograph of the assembled test fixture including the DUT in the middle.

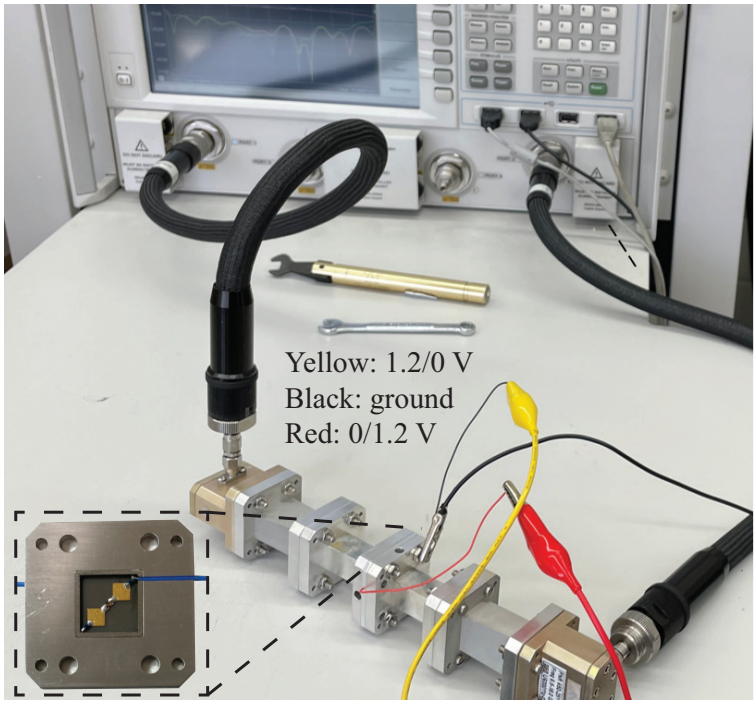

Figure 3.9: Photograph of the measurement setup used to measure the S-parameters of the DUT. The inset shows the photograph of the waveguide shim section that holds the AlN substrate supporting the dipoles in place.

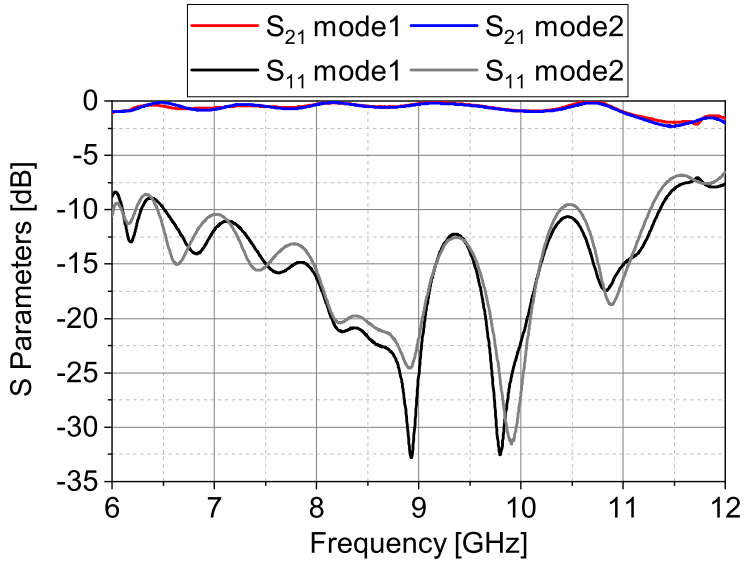

Figure 3.10: The measured transmission and reflection coefficients of the two modes of operation of PRUC.

standard coax-to-DR waveguide adapters to perform device characterization. Fig. 3.8 shows the complete system for measuring the scattering parameters of the proposed PRUC using a vector network analyzer (VNA). This system includes two commercially-available coax to standard DR waveguide adapters, WRD650, a transition DR waveguide section that converts the WRD650 waveguide to the custom DR waveguides with square cross sections used in the PRUC, and the device-under-test (DUT). The AlN substrate supporting the dipole structures was placed inside a waveguide shim and sandwiched by the two input/output DR waveguide sections. The frequency response was measured using a calibrated VNA at an incident power level of 1 mW over the frequency range of 6-12 GHz.

Fig. 3.9 shows the measurement setup for measuring the transmission and reflection coefficients of DUT. Commercially-available adapters, WRD650, were used to interface the device with the external test setup. A dc source was used to forward and reverse bias the PIN diodes when measuring the S parameters. As shown in Fig. 3.9, the black wire connects the body of the DR waveguides to the ground. The yellow wire connects one of the dipole structures to the dc source. Similarly, the red wire connects the other dipole structure to the dc source. When one of the dipole structures was forward biased, the other

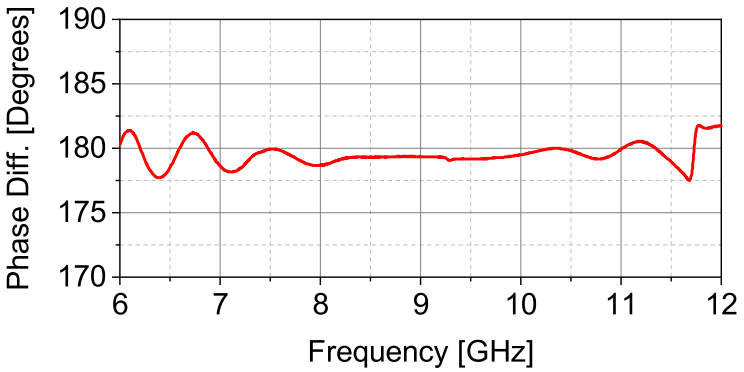

Figure 3.11: The measured phase difference between the transmission coefficients of the PRUC in its two modes of operation.

one was reverse biased and vice versa. The forward bias voltage was 1.2 V and reverse bias voltages in the range of 0 V to 10 V were used depending on the level of input power. Low-power measurements were conducted with a reverse bias voltage of 0 V and high-power measurements were performed with reverse bias voltages of up to 10 V as discussed in the following section. The dc bias current for the forward-biased PIN diode was 100 mA. The waveguide shim hosting the AlN substrate and the dipoles is shown in the inset of Fig. 3.9. Fig. 3.10 shows the magnitudes of the measured transmission and reflection coefficients of DUT in its two different operating states. Overall, the 1 dB transmission coefficient bandwidth, over which $|S_{21}| > -1$ dB, is in the 6-11 GHz (58.8%) frequency range. From 11 to 12 GHz, the $|S_{21}|$ is larger than -2 dB. Fig. 3.11 shows the phase differences of the measured transmission coefficient for the two different modes of operation. The phase differences between the two different modes are within $\pm 3^\circ$ of 180° over the operating band ranging from 6 to 12 GHz. These results demonstrate the ability of the proposed PRUC to electronically control the phase state over a wide bandwidth with 1-bit phase quantization.

I note several observations about the measurement and simulation results. First, the phase difference between two modes is almost 180° over the operating band for both the measurement and simulation results. Second, the magnitudes of the measured and simulated transmission coefficients are larger than -1 dB ranging from 6 to 11 GHz. There are slight

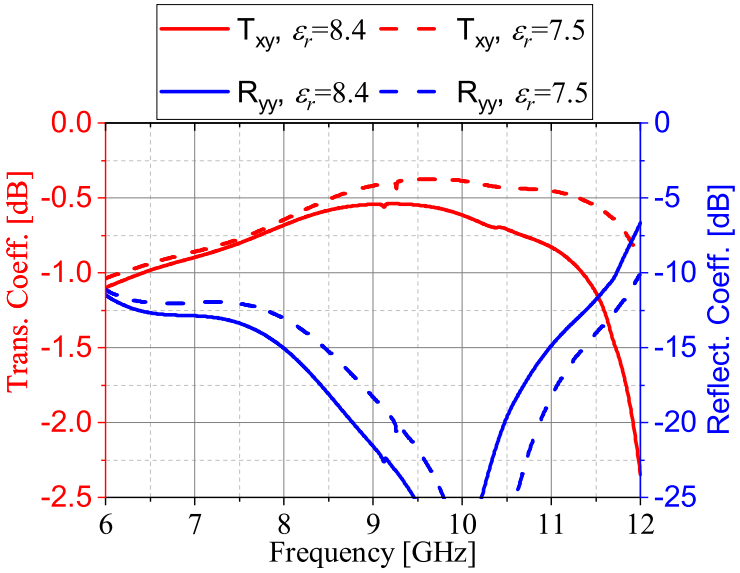

Figure 3.12: The simulated transmission and reflection coefficients of the two modes of the proposed PRUC. The results are obtained for two different values of dielectric constant and loss tangent used for the AlN slab.

differences in the transmission coefficients in the 11 to 12 GHz frequency range. For example, the measured $|S_{21}|$ of roughly -2 dB is lower than the simulated $|S_{21}|$, which is higher than -1 dB. These differences are likely due to the uncertainty in the exact value of the dielectric constant of the AlN substrate used in the fabrication of the DUT. Specifically, it is likely that the actual value of the dielectric constant is higher than the value of 7.5, which I used in the design process. To verify whether this hypothesis is true or not, I characterized the dielectric constant and loss tangent of the AlN substrate using a standard waveguide measurement technique [100]. Through this process, I measured a dielectric constant of 8.4 and loss tangent of 0.008 at 10 GHz for the specific AlN sample used in the construction of the device.

Fig. 3.12 shows the simulated transmission and reflection coefficients of the device with the original and the measured dielectric constant and loss tangent of the AlN substrate. As can be seen, the simulated transmission coefficient, $|T_{xy}|$, obtained for ϵ_r=8.4 and $\tan\delta$ = 0.008 values, is lower than that calculated using ϵ_r=7.5 and $\tan\delta$=0.005, especially in the 11 to 12 GHz frequency range. Considering that the simulated results obtained for (ϵ_r,

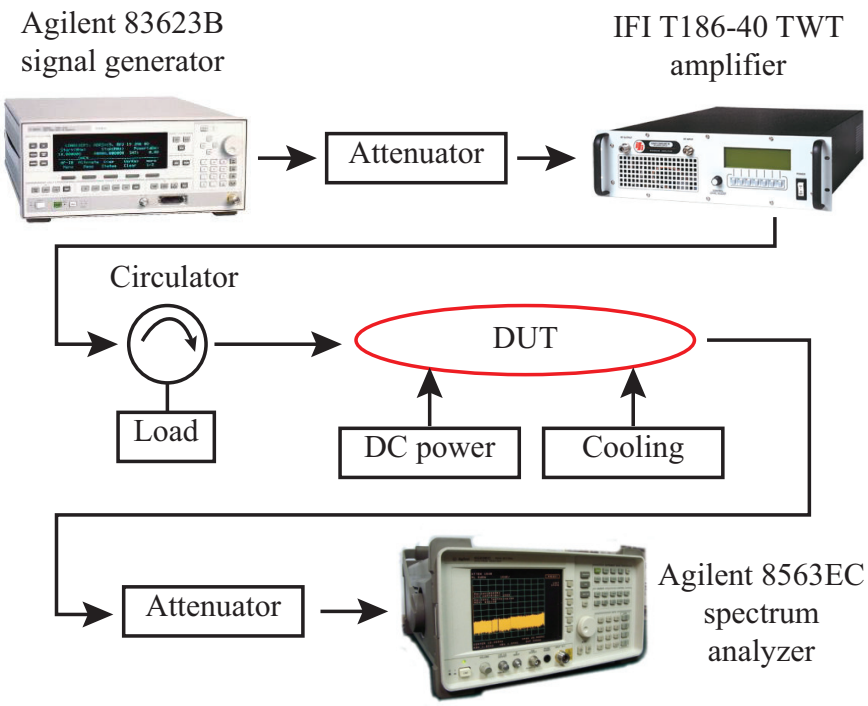

Figure 3.13: The block diagram of the measurement system used to characterize the response of the PRUC under high CW operating conditions.

$\tan\delta = 8.4,\ 0.008$) are closer to the measurement results, it is a reasonable conclusion that the real dielectric constant and loss tangent values of the AlN substrate are 8.4 and 0.008, respectively. These results also support the hypothesis that the differences between the actual ϵ_r and $\tan\delta$ values and those used in the simulations are the main reasons for the discrepancy observed between the measured and simulation results.

3.5 High-Power Experiments

In this section, I will discuss the high-power characterization of the proposed PRUC. I conducted these experiments both in the CW and pulsed operating modes to measure the average and peak power handling capabilities of the DUT, respectively. I also conducted experiments to determine the linearity of the response of the DUT and performed transmission/reflection coefficient measurements under different input power levels.

Table 3.1: The CW power level that the PRUC was subjected to without failing at different frequencies within its operating band. This power was limited by the maximum output power level available from the TWT amplifier used in the measurements.

Frequency [GHz]	6	8	10	11	12
Power into DUT [W]	34.0	35.5	36.3	35.5	35.5

3.5.1 CW Experiments

Fig. 3.13 shows the experimental setup used to measure the response of the DUT under high average input power level conditions. I used a broadband travelling-wave-tube (TWT) amplifier to provide a high input power level at different frequency points. The TWT amplifier operates over a frequency range of 6-18 GHz and provides 40 W CW power at the band edges (6 and 18 GHz) and approximately 60 W CW at 10 GHz. The TWT has also a built-in solid state preamplifier allowing it to achieve the maximum output power level with an input power level of about 0 dBm. The other components of this system include a signal generator (Agilent 8362B), a spectrum analyzer (Agilent 8563EC), a circulator, the DUT, attenuators before the amplifier and spectrum analyzer, a dc power source, and a forced-air cooling system. The spectrum analyzer was used to record the output power. The dc power source was used for biasing the two PIN diodes at appropriate dc voltage levels. As the input RF power applied to the device increases, the reverse dc bias voltage at the two terminals of the reverse-biased PIN diode should also be increased as discussed in [101]. The forward bias voltage was 1.2 V in all the CW experiments. A reverse bias voltage of 10 V was used to ensure the reverse-biased PIN diode working in a safe region during the high-power CW experiments. A forced-air cooling system with an inlet air power of 15 psi was employed during the CW high-power experiments.

I conducted a series of experiments to verify the average power handling capability of the PRUC and to attempt to characterize any potential nonlinearities that may be generated

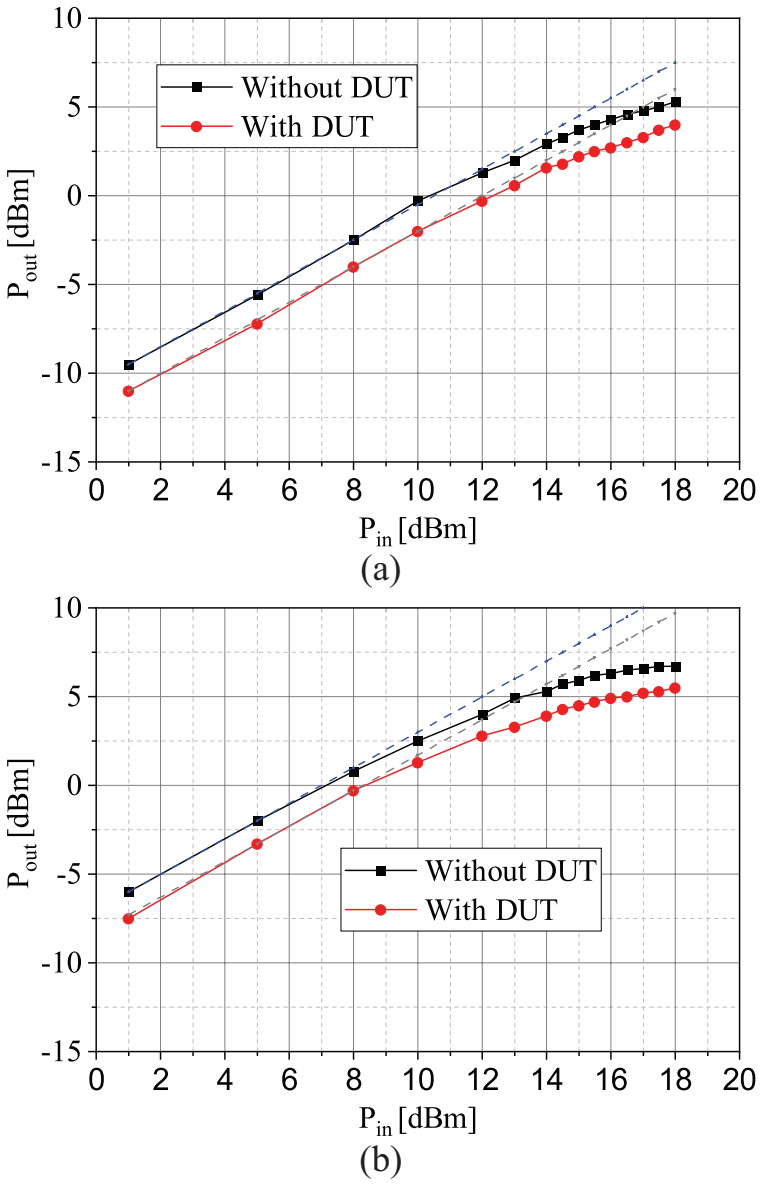

Figure 3.14: Measured output power vs. input power levels in the presence and absence of the DUT. P_{in} is measured at the output of the signal generator and P_{out} is measured at the input of the spectrum analyzer (see Fig. 3.13). Attenuators with attenuation coefficients of 30 dB and 40 dB are present in the system chain before and after the TWT amplifier, respectively. (a) 8 GHz and (b) 10 GHz.

by it. The CW measurements were carried out in two steps using the measurement setup shown in Fig. 3.13. First, the transmitted CW signal was measured in the absence of the DUT and its level was recorded as a baseline. This baseline allows us to calculate the loss of the entire system without the DUT. Then, I measured the transmitted CW signal in the

presence of the DUT for different input power levels. The input power level to the system was then gradually increased to determine the power level at which the device fails and to characterize the linearity of the entire system. I conducted the CW experiments at 6, 8, 10, 11 and 12 GHz. At each frequency and for each input power level, the power was applied to the DUT for a duration of 10 minutes. After this, the switching performance of the device was checked again and we verified that both PIN diodes were functioning properly. Table 3.1 lists the maximum CW power level applied to the DUT at each frequency. These power levels are limited by the maximum available power at the output port of the TWT as well as the losses of the different system components located between the output of the TWT and the input of the DUT. Considering that the DUT was not damaged during any of these experiments and at any of the applied CW power levels, I conclude that the average power handling capability of this unit cell is more than 34 W CW. Experimental determination of what maximum CW power handling capability of the device is requires a CW amplifier capable of providing a higher output power level, which is not currently available to us. Nevertheless, the experiments verify that the proposed PRUC is capable of supporting the minimum 22 W/cm^2 desired input power density.

I also characterized the nonlinearity of the system in an attempt to determine the level of nonlinearities that may be introduced by the PRUC. The primary factor expected to cause nonlinearity in the response of the proposed PRUC is the nonlinear response of the PIN diodes. By selecting the right PIN diode for a given power level and using appropriate forward and reverse bias voltages, the nonlinearities contributed by PIN diodes are usually very low [102]. Fig. 3.14 reports the measured output power versus the input power (as measured from the output port of the signal generator) at 8 and 10 GHz. Attenuators with attenuation coefficients of 30 dB and 40 dB are present in the system chain before and after the TWT amplifier, respectively. The measurements were conducted in both the presence and absence of the DUT. Observe that there is little difference between the linearity of the two curves indicating that the observed nonlinearities are due to the nonlinear

responses of the other system components. Indeed, after examination of the other system components, I determined that the nonlinear response observed in Fig. 3.14 is primarily due to the nonlinearity of the TWT amplifier. These measurements were also conducted at other frequencies (6 and 12 GHz) yielding similar results.

I also performed two-tone tests to characterize the third-order intermodulation distortion (IMD) that may be introduced by the PRUC [103]. Two input signals with frequencies of 8.995 GHz and 9.005 GHz that generated using different signal generators were combined by a power combiner. Then, the combination of the two input signals was fed to the TWT amplifier. Finally, the signal was transmitted to the DUT, and received by the spectrum analyzer. To determine the level of nonlinearities that may be introduced by the PRUC, this IMD experiment was also conducted in both the presence and absence of the DUT. I found no significant difference between the level of intermodulation products measured in the presence and in the absence of the DUT. Therefore, we conclude that the nonlinearities measured in these experiments are primarily contributed by other components used in the test setup including the TWT amplifier and the spectrum analyzer. Furthermore, we conclude that the nonlinearities of the DUT are lower than what we can measure using the existing system. This is not surprising as the nonlinearities generated by PIN diodes are very small [102,104].

3.5.2 Pulsed Power Experiments

I have also conducted a series of high-power pulsed experiments on the fabricated PRUC prototype to experimentally verify its peak power handling capabilities. Pulsed experiments were performed using an X-band high-power magnetron source capable of providing a peak power of 25 kW with a pulse width of 1 μs at 9.382 GHz [105–109]. Fig. 3.15 shows the pulsed experimental setup. The setup is composed of a high-power pulsed X-band magnetron source, WR-90 waveguides, a circulator, an E-H tuner, directional couplers, crystal detectors, the DUT, high-power loads, an oscilloscope, and a dc power source. The power delivered to the DUT was adjusted by the E-H tuner along with the circulator in different pulsed experiments.

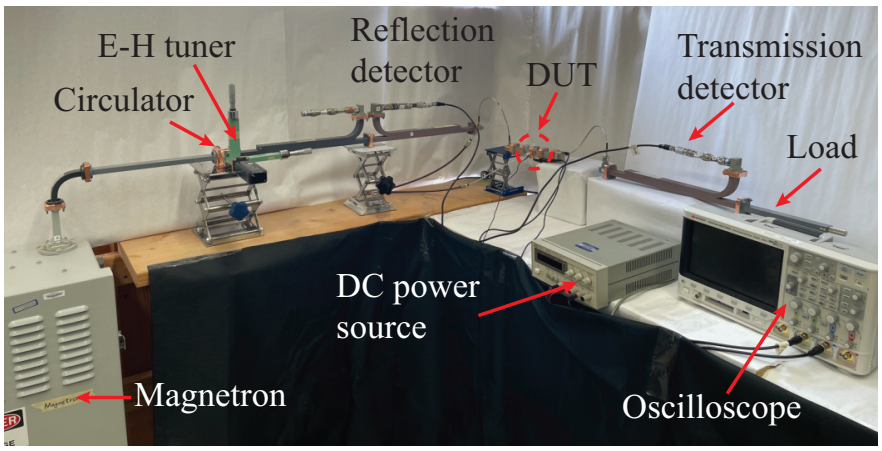

Figure 3.15: Experimental setup for measuring the peak power handling capability of the proposed PRUC using a high-power magnetron. The magnetron generates a single-frequency pulse at 9.382 GHz with a peak power of 25 kW and a pulse width of 1 μs.

All waveguide connections were sealed by copper tape to minimize any potential leakage of power. The crystal detectors that were connected to the outputs of the directional couplers were used to detect the transmitted and reflected signals when the DUT was illuminated with the incident pulsed signal. The detector outputs were connected to the digital oscilloscope that recorded the transmitted and reflected pulsed waves. The dc power source was used to provide the forward and reverse bias voltage for the PIN diode of the DUT. The magnetron was operated in single-pulse mode. This means the magnetron only generated one short-duration pulse with a pulse width of 1 μs for every high-power pulsed experiment.

Fig. 3.16 shows the normalized, measured time-domain power transmission and reflection coefficients of the DUT under different illuminated peak power levels. The normalized time-domain power transmission coefficient is defined as the ratio of the transmitted signal detected by the crystal detector when the DUT is present to that after the DUT is removed. A waveguide short-circuit termination was used as a calibration standard to calculate the normalized time-domain power reflection coefficients. The time-domain power reflection coefficient is obtained by normalizing the reflected signal detected by the crystal detector in the presence of the DUT to the reflected signal detected by the crystal detector when the DUT is replaced with a short-circuit termination. I conducted the pulsed experiments for power

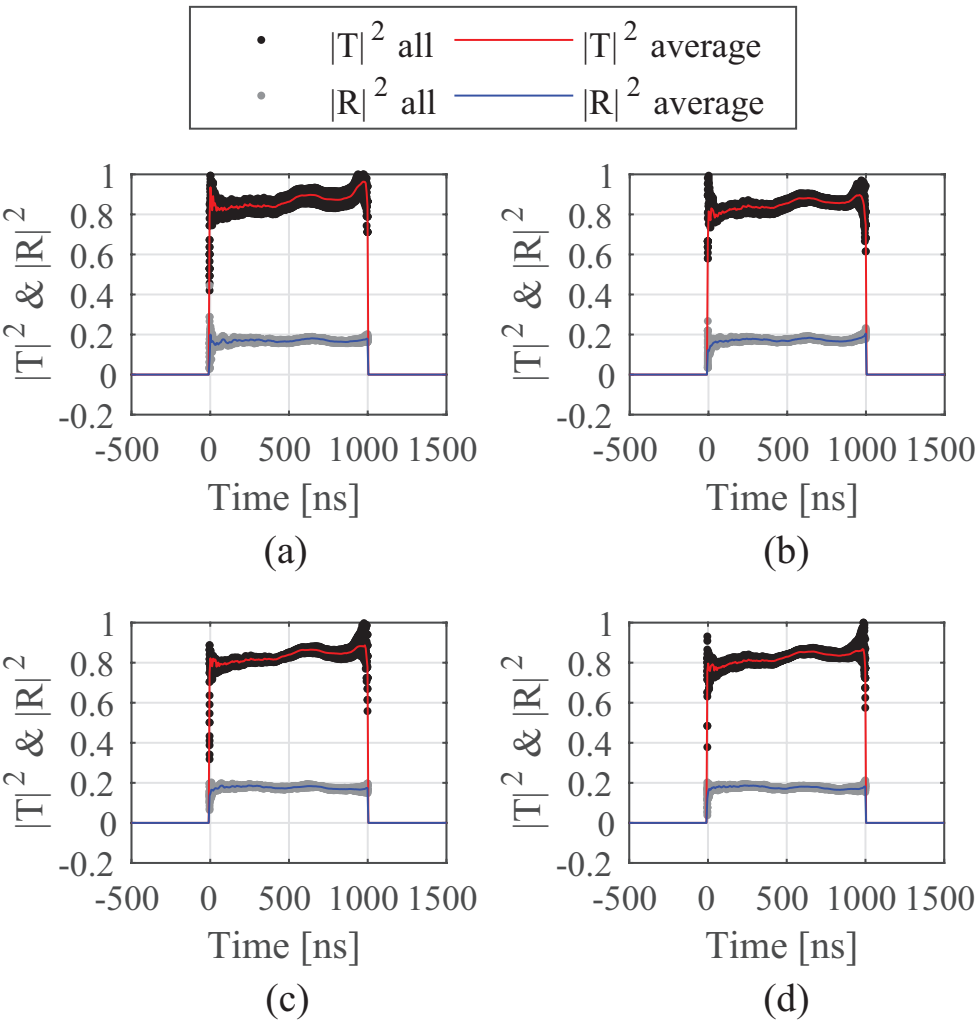

Figure 3.16: Normalized, measured time-domain power transmission and reflection coefficients for the PRUC under different incident peak power levels. The power levels incident on the PRUC are: (a) 316 W; (b) 378 W; (c) 442 W and (d) 500 W.

levels at 500 W, 600 W, 700 W, and 800 W, respectively, as measured at the output of the E/H tuner. The measurement setup shown in Fig. 3.15 has about 2 dB loss before the DUT. Therefore, the corresponding power levels delivered into the DUT are 316 W, 378 W, 442 W, and 500 W, respectively. For each power level, I conducted the experiment 25 times and averaged the normalized time-domain transmission and reflection coefficients. Observe that before breakdown, most of the power was transmitted through the DUT and absorbed by the load. Only a small portion of the power was reflected. As can be seen from Fig. 3.16, the normalized, measured time-domain power transmission and reflection coefficients are about

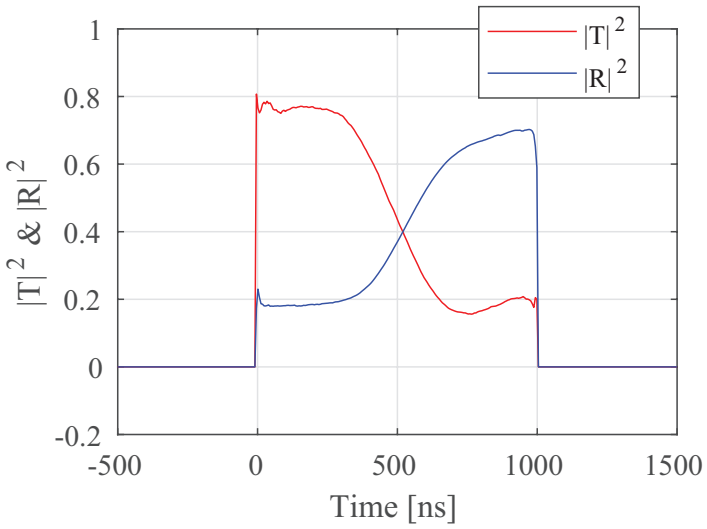

Figure 3.17: Normalized, measured time-domain power transmission and reflection coefficients for the PRUC under 568 W incident peak power level. As can be observed, PIN diode breakdown happened at about 350 ns after the start of the high-power pulse.

Table 3.2: Comparison between the proposed design and other passive phase shifter technologies reported in the literature.

Reference	This work	[15–17]	[18–21]	[22–24]	[25, 26]
Tuning mechanism	PIN diode	MEMS	Ferrite	Semiconductor	Mechanical
Power handling capability	CW: >34 W; Peak: 500 W	CW: few W	CW: ∼kW; Peak: 100s kW	CW: few W	Peak: ∼MW
Bandwidth	Wide (one octave)	Wide (>40%)	Moderate (<30%)	Wide (>40%)	Moderate (<25%)
Switching speed	10s ns	10-100 μs	10-100 μs	∼ns	100s ms-seconds
Cost	Medium	Low	Very high	High	High
RF loss	1 dB/1-bit	1-2 dB/bit	<1 dB/360°	∼2 dB/bit	<1 dB/360°
Size and weight	Medium	Small	Large	Small	Large
DC power consumption	Low (0.12 W)	Negligible	High (∼10W)	Low (<10 mW)	High (few W)

0.8 and 0.2, respectively.

When the incident power level increases, the maximum local field density within the

DUT exceeds the breakdown level, and the PIN diode of DUT fails. This breakdown can be observed in the form of a significant increase in the reflected power level and a significant decrease in the transmitted power level. Fig. 3.17 shows the normalized, measured time-domain power transmission and reflection coefficients for the DUT under 568 W of incident peak power level when the breakdown occurred. As can be observed, the PIN diode breakdown happened at about 350 ns after the start of the high-power pulse. The transmission coefficient, $|T|^2$, is close to 0.8 before breakdown. After breakdown, the transmission coefficient, $|T|^2$, decreases to around 0.2. Conversely, the reflection coefficient, $|R|^2$, is increased from 0.2 to around 0.7. Pulsed experiments at an incident power level of 568 W were conducted twice and the device failed both times. Therefore, the maximum power that the DUT can reliably handle is determined to be 500 W and the breakdown happens at the peak power of 568 W. The peak power handling capability of 500 W for this unit cell suggests that a phased-array constructed from this building block should be capable of handling peak power levels of 3.5 MW/m^2. After the breakdown, I examined the device and the PIN diodes and found that the forward biased PIN diode was the only component of the PRUC that was damaged. No other evidence of breakdown or damage was observed in any of the other DUT components.

I compared my design with existing phase shifter technologies to highlight the primary contributions of the present work. Table 3.2 compares several key figures of merits of the existing phase shifter technologies. Here, I only name a few references for each phase shifter technology as their performances are representative of each category. The interested reader is referred to [14,21] for comparison of existing phase shifter technologies. Careful examination of Table 3.2 reveals that the proposed design has three important features, the combination of which is not available from the other competing designs reported in Table 3.2. These include: 1) very-high-power handling capability of at least 23.6 W/cm^2 average power and up to 347 W/cm^2 peak power per element; 2) wide operating bandwidth of one octave (6-12 GHz); and 3) fast electronic switching capability with 1-bit phase quantization. None of

the other designs reported in Table 3.2 possess all of these characteristics in a single design. The phase shifter design described herein combines the high-power handling capability, wide bandwidth, and fast electronic switching features with a relatively low-loss and low-cost strategy. The proposed design can be used in high-power phased-arrays in applications such as radar and communication systems on ships and aircraft, and electronic warfare systems. It is possible that the peak power handling capability of this phase shifter can be increased by deploying electronic switches capable of handling higher peak power levels. Likely examples may include plasma switches or semiconducting switches with higher breakdown voltage levels than the silicon-based PIN diode switch used in this work. This is expected to pave the way towards using this phase shifter architecture in developing HPM phased-arrays that have significantly higher power handling requirements (hundreds of MW to GW peak power levels).

3.6 Conclusions and Discussions

This chapter presented the unit cell of a wideband, high-power-capable phase shifter that provides 1-bit electronically switchable phase quantization using the concept of polarization rotation. This PRUC offers 0°/180° phase shift over a wide bandwidth of 6 to 12 GHz. I designed and fabricated a prototype of the proposed PRUC along with the required test fixtures used to measure its frequency response. Low-power scattering parameter measurements performed using a calibrated VNA showed successful operation of the 1-bit phase shifter over the 6-12 GHz range. The measured insertion loss was better than 1 dB in the 6-11 GHz range and better than 2 dB in the 11-12 GHz frequency range.

I also conducted a series of continuous wave and pulsed high-power measurements to characterize the average and peak power handling capabilities of the proposed PRUC and to examine its linearities. CW experiments demonstrated that the average power handling capability of the PRUC is higher than 34 W over the entire 6-12 GHz frequency band. Due

to the output power limitations of the power amplifier used in these experiments, I was not able to determine the maximum CW power level that the device can handle. Nonetheless, 34 W (23.6 W/cm^2) CW is high enough to meet the objectives of the present research project. The peak power handling capability of the device was determined to be 500 W (347 W/cm^2) for short-duration pulses at a frequency of 9.382 GHz. It is likely that the device is capable of handling a similar level of peak power across its entire frequency band of operation since the main mechanism of failure was the breakdown of the silicon-based PIN diodes. However, this could not be experimentally demonstrated since the available high-power source is a single-frequency magnetron.

Finally, experiments conducted to characterize the nonlinearities of the device did not show any significant nonlinearity introduced by the PRUC. In characterizing the 1-dB compression point and the third-order intermodulation intercept point of the device, the measurement accuracy was limited by the nonlinearities of the other components used in the measurement system (power amplifier and the spectrum analyzer). This indicates that the use of this element in high-power phased-array antennas is not expected to cause major nonlinearity problems.

The peak power handling capability of this phase shifter was determined for a relatively long pulse duration of 1 μs. It is possible that this device can handle higher peak power levels if shorter duration pulses (e.g., less than 200 ns) are used. I, however, cannot verify this hypothesis at this point due to the lack of availability of such sources. Additionally, the peak power handling capability of this phase shifter can potentially be increased by deploying electronic switches capable of handling higher peak power levels (e.g., by using GaN, GaAs, photoconductive, or plasma switches as opposed to the silicon-based PIN diodes used in this work). This is expected to pave the way towards using this phase shifter architecture in developing HPM phased-arrays that have significantly higher power handling requirements (hundreds of MW to GW peak power levels). Exploration of these topics are left as future works.

Chapter 4

X-band, Mechanically-Beam-Steerable Lens Antenna Exploiting the Risley Prism Concept

The full manuscript was published as:

Z. Zhang, H. Luyen, J. H. Booske and N. Behdad, "X-band, mechanically-beam-steerable lens antenna exploiting the Risley prism concept," *IET Microw., Antennas Propag.*, vol. 14, no. 14, pp. 1902–1908, Nov. 2020.

4.1 Introduction

Phased array antennas provide adaptive radiation patterns in various applications ranging from satellite and airborne communications to imaging systems [1, 2]. While many active phased-array antennas have been developed, the cost, loss, power handling capability, and thermal management challenges associated with high-power active phased-array antennas have limited their use primarily to high-end military applications [1, 2]. This has motivated developing techniques to design less expensive phased-array antennas. Beam steering arrays exploiting Rotman [110] or Luneburg lenses [111], which do not need T/R modules, are attractive for radar and communication systems. However, the design of the beam switching network gets complicated as the total number of beams increases. Electronically-reconfigurable reflect-/transmit-arrays, which provide very high-speed beam steering and do not need individual T/R modules for array elements, have been studied as promising alternatives to phased arrays [63, 112]. However, electronic switches can be very lossy at higher frequencies. Furthermore, most electrically-tunable reflect-/transmit-arrays reported to date use coarse, 1-bit phase quantization, which results in low aperture efficiencies. Therefore, in applications requiring low cost and prioritizing high efficiency over high-speed beam scanning, mechanical beam-steering systems that do not require electronic switches may be good alternatives.

Various techniques have been presented to realize mechanical beam steering. These can be divided into three categories: element movement methods [44, 45], feed displacement methods [46–48], and array movement methods [49–54]. The element movement methods control the phase responses of individual unit cells by deploying micro-motors to move [44] or rotate [45] each unit cell independently. However, implementing individual control for the array elements increases complexity and cost, especially for arrays consisting of large numbers of elements. Alternatively, methods exploiting movement of feed antennas or the whole PSSs to scan the beam have been investigated to provide a good compromise between practicality

and performance. The less complex and costly feed displacement methods move a feed antenna along focal arcs of a lens or reflectarray to generate radiation patterns with different main beam directions. These techniques have been demonstrated to provide ±45° beam scanning ranges with maximum scan losses of about 4 dB at Ka-band [46] and X-band [47,48]. However, the feed movement increases the complexity and cost of the mechanical system supporting this movement. Consequently, the feed displacement methods are not commonly used. Most mechanical beam-steering systems using array movement methods only need one or two actuators to move or rotate the phase-shifting arrays [49–54]. This attractive feature provides a good solution for less complex and more affordable beam-steerable antennas in applications that do not require high-speed beam scanning.

Recently, mechanical beam-steerable antenna systems based on the Risley prism concept have attracted attention for their simplicity and good beam scanning performance [53,54,56, 57]. A Risley-prism-based beam-steering system typically consists of a pair of PSSs, which replace the two dielectric wedges in the original Risley prism concept [59], illuminated by a feed antenna. The relative rotational displacement of two PSSs provides beam steering in both azimuth and elevation directions in the upper hemisphere of the outgoing aperture. The design concept has been demonstrated for mechanical beam-steering systems working at X-band with a ±20° scan range [54], at Ka-band with a ±75° scan range [53], at Ku-band with a ±40° scan range [57] and at X-band with a ±51° scan range [56]. However, these works did not address the question of how to determine the best distance between the two PSSs in the design procedure for optimizing the beam scanning performance and no bandwidth results were presented in [53,54,56,57]. In this chapter, I present a mechanically-beam-steerable antenna using the Risley prism concept. Low-pass frequency selective surface (FSS) unit cells populating the two PSSs were co-designed to select the distance between the two PSSs for improving the gain and output phase accuracy of the antenna system. A fabricated beam-steerable antenna system prototype demonstrated a bandwidth of 4.2% at broadside direction, the ability to scan the main beam from broadside direction to $\theta = 60°$

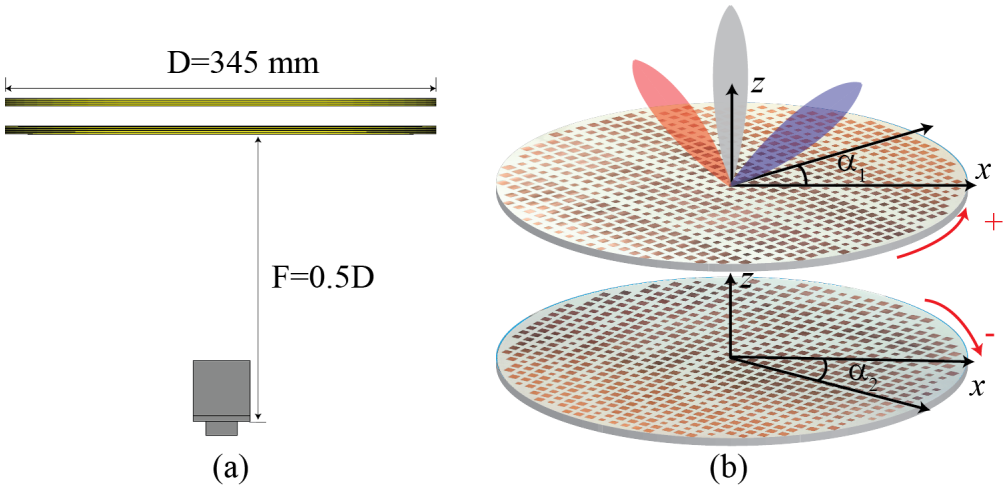

Figure 4.1: (a) Configuration of the proposed beam steering system consisting of two PSSs and a feed horn antenna. (b) 3-D view of the two PSSs.

with less than 3.5 dB gain variation, and high beam-pointing accuracy.

4.2 Designs of PSSs and Unit Cells

Fig. 4.1 shows the configuration of the mechanical beam-steering antenna system based on the Risley prism concept. Two prisms are implemented with two circular PSSs that consist of square unit cells with periodicities of d. While the top PSS is designed to provide a linear phase gradient, the bottom PSS is designed to combine the phase correction pattern for collimating the wavefront illuminated by the feed antenna with the desired phase gradient. When a PSS is illuminated with a plane wave under normal incidence, the relationship between the unit cell's size, d, phase difference between two adjacent unit cells along the phase gradient direction, $\Delta\phi$, and the angle showing the direction of the transmitted wave, θ, can be expressed as $kd\sin\theta = \Delta\phi$, where k is the wave number in free space. When two PSSs, each with a linear phase gradient of $\Delta\phi/d$, are stacked against and rotated with respect to each other, the equivalent phase gradient at the output aperture can be calculated as a linear combination of the two phase gradient vectors and changes as a function of the rotation angles of the two surfaces. As a result, the main beam of the outgoing wave can

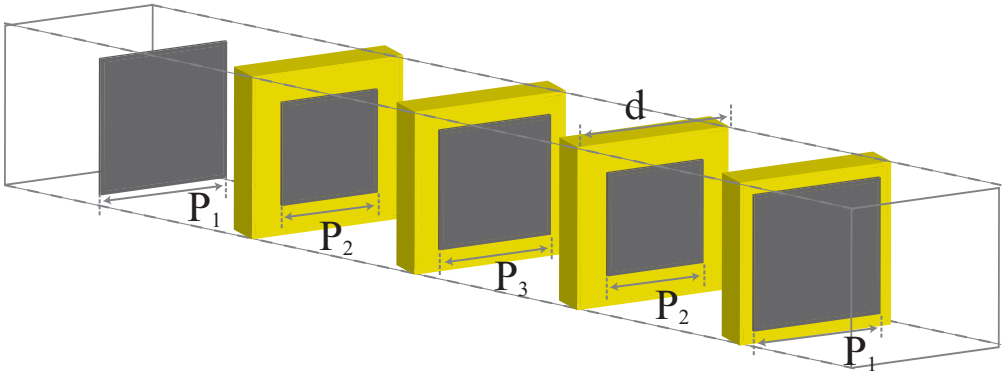

Figure 4.2: 3-D topology of the low pass unit cell (bonding layers between dielectric substrates are not shown). Dark gray represents metal and yellow represents dielectric substrates.

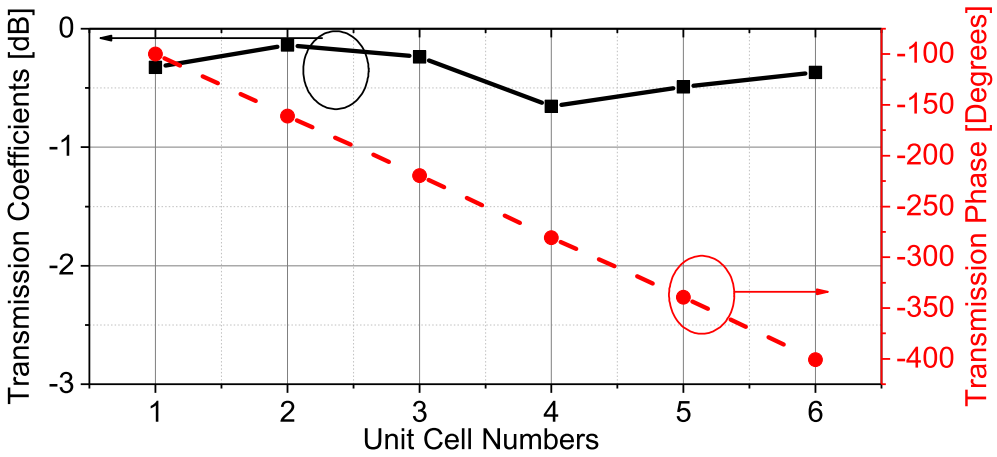

Figure 4.3: Magnitudes and phases of simulated transmission coefficients at 10 GHz of six unit cell states populating the two PSSs.

be pointed anywhere within a cone with an apex angle of $2\theta_0$, where θ_0 is the maximum scan angle corresponding to a phase gradient of $2\Delta\phi/d$. In this chapter, a maximum scan angle of 60° was selected for the beam-steering system, which is sufficient for most satellite and airborne systems [1,2]. The phase progression between two adjacent unit cells along the phase gradient direction was chosen to be 60° in the proposed PSSs, which means six different unit cells are needed to cover the 0°-360° phase range. Then, the unit cell dimension, d, was calculated to be 11.5 mm (about $0.385\lambda_0$ at 10 GHz). The six unit cell states are used to populate the two PSSs to realize the desired phase profiles for the beam steering operation.

Table 4.1: Dimensions for all six unit cells.

Unit cell number	1	2	3	4	5	6
P_1 (mm)	4.9	6.2	6.93	7.2	7.31	7.6
P_2 (mm)	1	5.64	6.1	6.8	7.31	7.53
P_3 (mm)	1.5	5.8	6.93	7.2	7.31	7

Table 4.2: Average transmission loss and phase error of 36 unit cell combinations for different spacings between the two PSSs

Distance (mm)	1	2	3	4	5
Average loss (dB)	1.87	1.76	1.79	1.89	2.05
Phase error (Degrees)	20	8.2	12.6	19.4	24.2

I designed unit cells of a low-pass FSS similar to ones presented in [113, 114] to provide the desired phase shift values needed for the PSSs. Fig. 4.2 shows the 3-D view of the unit cells used in this work. Each unit cell is composed of five metal layers sandwiching four dielectric substrates. The unit cells were implemented using Rogers RO4003C substrates, with thicknesses of 0.81 mm and ϵ_r of 3.38, bonded together by 0.1 mm-thick Rogers RO4450F prepregs with ϵ_r of 3.52. The unit cell structure is symmetric with respect the the center (third) metallic layer for simplicity. The dimensions of the capacitive patches in the metallic layers were tuned in full-wave simulations of the unit cells with periodic boundary conditions in CST Microwave Studio to achieve the desired transmission phases at 10 GHz. Fig. 4.3 shows the magnitudes and phases of the simulated transmission coefficients of different unit cells at 10 GHz. All unit cells provide transmission coefficients higher than -0.7 dB and the transmission phase differences between any two consecutive unit cells are about 60°. I also examined the frequency responses of the six unit cells with respect to the incidence angle in the range of 0° to 45° with 15° increments. The unit cell responses were found to be stable for incidence angles in the ±45° range. The dimensions of the metallic patches in each unit cell are listed in Table 4.1.

The distance between the two PSSs is an important design parameter that needs to be

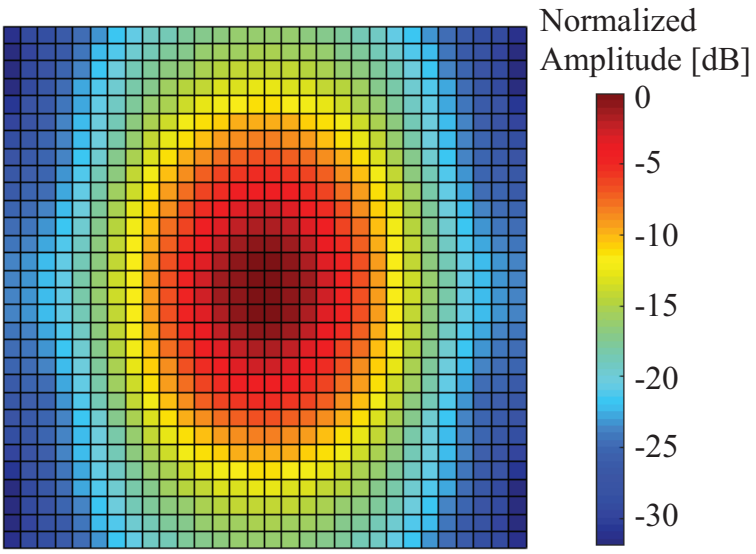

Figure 4.4: Simulation results for normalized electric field pattern generated by the feed horn antenna on the plane of the first lens.

determined. To identify this distance, I conducted a co-design method which evaluates the magnitudes and phases of the transmission coefficients through two unit cells placed one on top of another when the distance between them is varied from 1 mm to 5 mm with a 1 mm interval. Each unit cell is chosen from one of the six finalized unit cells. In other words, I conducted a two-degree-of-freedom optimization, involving separation distance (5 discreet options) was one degree of freedom, and the unit cell design (6 discreet options) was the second degree of freedom. Due to the rotations of the PSSs for different beam scan angles, different unit cell combinations (between a unit cell of the lower PSS and a unit cell of the upper PSS right above it) occur. Since there are six different unit cells, a total of 36 unit cell combinations were evaluated in the simulations for each distance value, for a total of 180 choices in the discretized optimization space. I simplified the simulations by assuming the edges of two square-shaped unit cells are always aligned with each other, which typically is not the case considering the rotations of the two PSSs. After each simulation, I calculated the transmission loss and difference between the actual and expected transmission phases. The transmission loss and phase error were then averaged over 36 combinations for each distance value. Table 4.2 shows the average transmission loss and phase error for five distance values

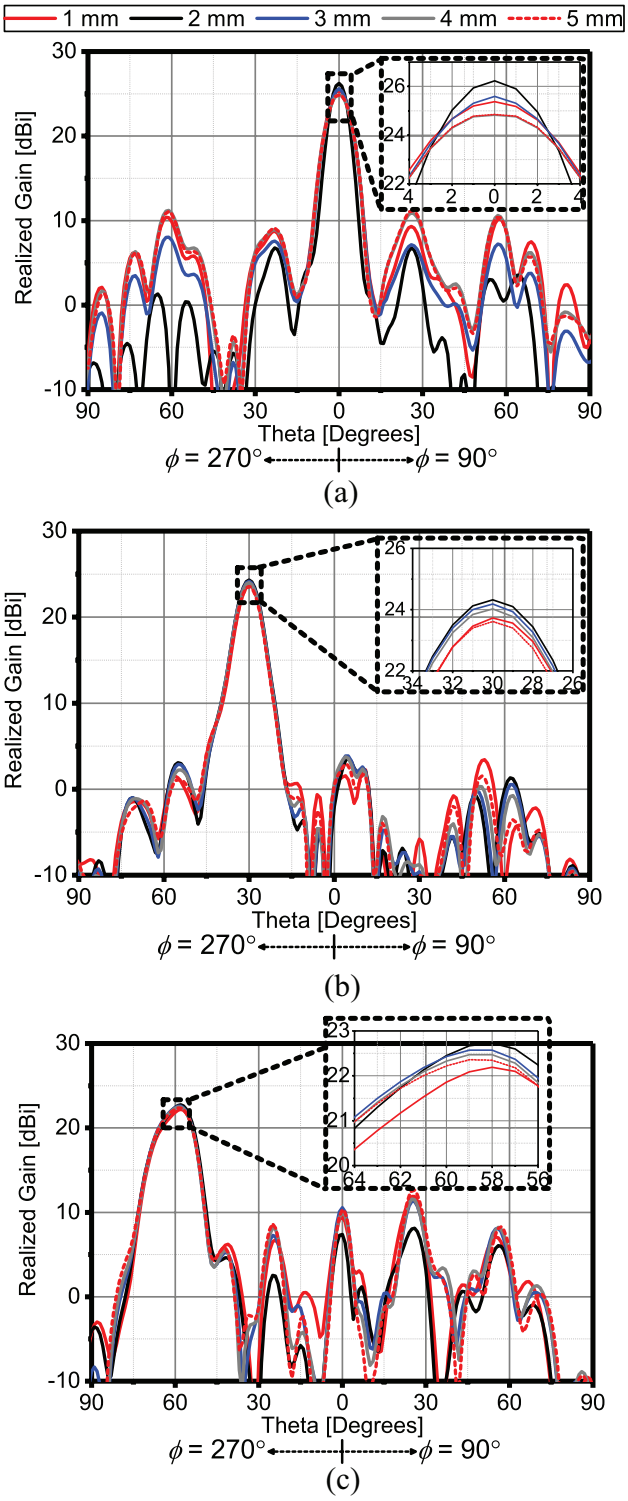

Figure 4.5: Simulated radiation patterns of the beam-steerable antenna system at 10 GHz. (a) Main beam at $\theta = 0°$, (b) Main beam at $\theta = 30°$ and (c) Main beam at $\theta = 60°$ in the H-plane for different distances between the two PSSs.

from 1 mm to 5 mm. A distance of 2 mm between the two PSSs was found to have the best overall performance in terms of providing the lowest transmission loss and phase error. The overall performance may be further optimized by considering the oblique incidence and using a better space resolution between two unit cells. Here I only aim to demonstrate the validity of this co-design method.

4.3 Simulation and Measurement Results of the Beam-Steerable Antenna System

I performed full-wave simulations of the beam-steerable antenna system shown in Fig. 4.1 to verify the results obtained with the unit cell co-design method. The two PSSs had diameters of D=345 mm (equivalent to $11.5\lambda_0$ at 10 GHz). A horn antenna with an aperture area of $40\times$ 40 mm^2 was used to illuminate the PSSs from a distance of f=172.5 mm. The peak gain of the feed horn antenna is 12.8 dBi. Fig. 4.4 shows the corresponding simulated electric field distribution generated by the feed horn antenna on the surface coinciding the first lens aperture at 10 GHz. The amplitudes of the incident electric fields at the edge of the first lens aperture in E-plane and H-plane are about 24 dB and 16.5 dB, respectively, lower than those at the lens's center.

Fig. 4.5 shows the radiation patterns of the antenna system configured to generate the main beams at $\theta = 0°, 30°$ and 60°, respectively, for five different cases where the distance between the PSS was varied from 1 mm to 5 mm. At the broadside direction, observe that the distance of 2 mm provides the highest realized gain (about 0.5-1.0 dB higher than the other cases) and the lowest side lobe levels. For the main beams that are generated at $\theta = 30°$ and 60°, the distance of 2 mm still provides the highest realized gain. The peak gain improvement for the 2 mm spacing is 0.1 - 0.6 dB higher than the other spacing choices. Therefore, I chose the distance of 2 mm between the PSSs for the final antenna system design and evaluated its beam scanning performance using full-wave simulations. Figs. 4.6(a) and

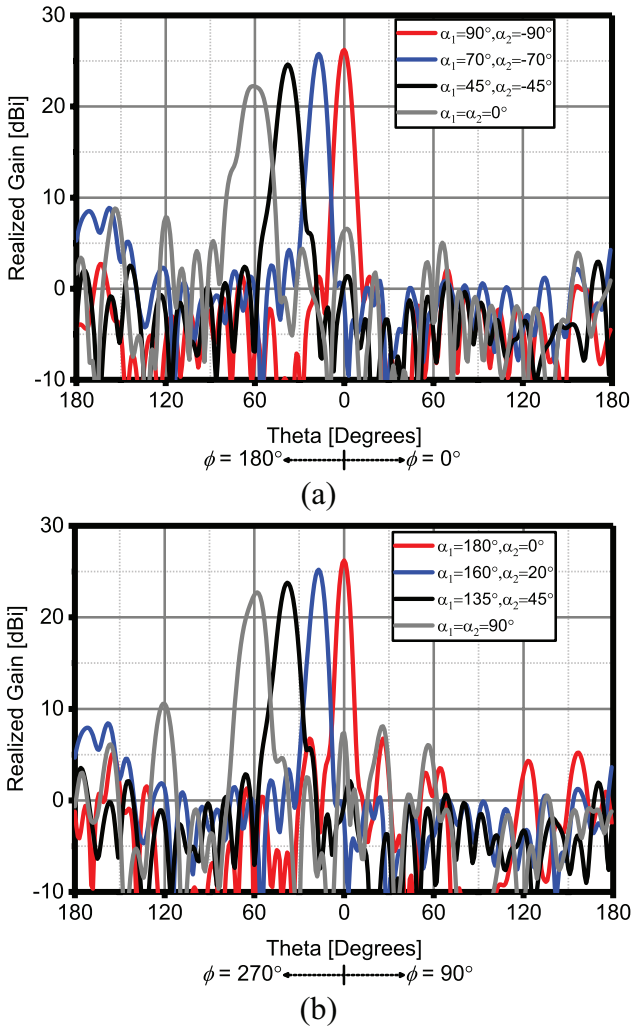

Figure 4.6: Simulated radiation patterns of the beam-steerable antenna system at 10 GHz for different scan angles for the final antenna system design with a 2-mm spacing between the two PSSs in the (a) E-plane and (b) H-plane.

(b) show the simulated radiation patterns at 10 GHz for four different scan angles in the E- and H-planes, respectively. Each scan angle corresponds to a rotation configuration, which is defined by the rotation angles with respect to the x-axis of the two PSSs, α_1 and α_2, as shown in Fig. 4.1(b). In the E-plane (x-z plane), the peak gain at broadside is 26.2 dBi and the gain reduction at $\theta = 60°$ direction is 4 dB. In the H-plane (y-z plane), the gain is reduced by 3.5 dB when the beam is scanned from broadside to $\theta = 60°$. Additionally, side lobe levels are below -12.4 dB and normalized cross-polarization levels are lower than -25 dB for all beam scenarios.

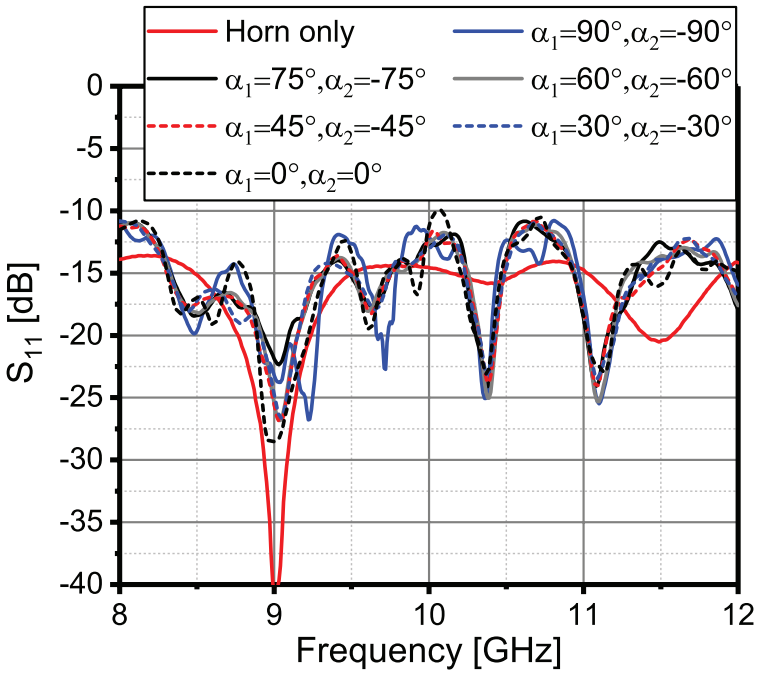

Figure 4.7: The experimental S_{11} of the beam steering antenna system for all beam scenarios.

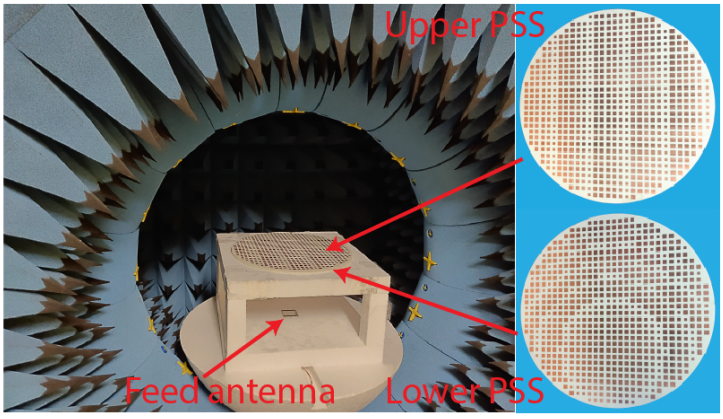

Figure 4.8: Photographs of the fabricated prototype and the measurement setup used to characterize the response of the antenna.

Prototypes of the two PSSs were fabricated using printed circuit board lithography. Fig. 4.7 shows the experimentally measured S_{11} of the beam steering antenna system for all beam scenarios. I also added a reference S_{11} by measuring the feed horn alone. The reflection coefficients varied when rotating two PSSs, but the reflection coefficients at the input of the horn antenna was below -10 dB for all beam steering scenarios.

The fabricated PSS prototypes were experimentally characterized in a near field spherical

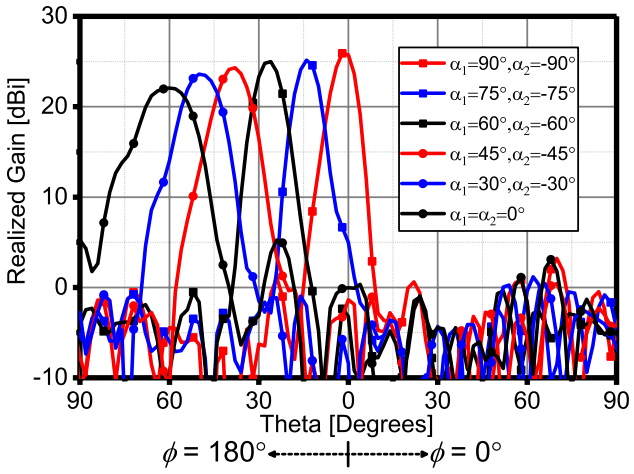

(a)

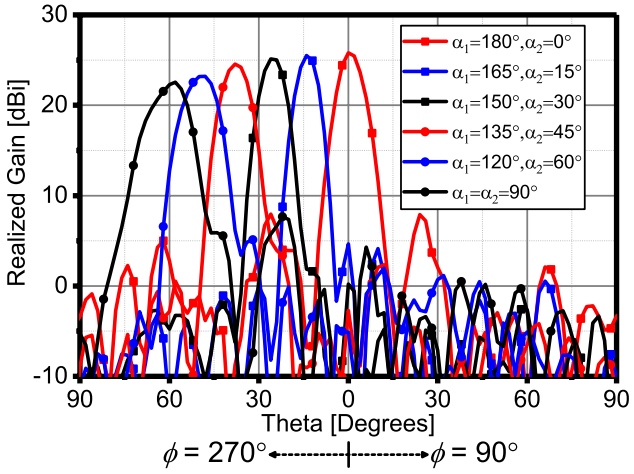

(b)

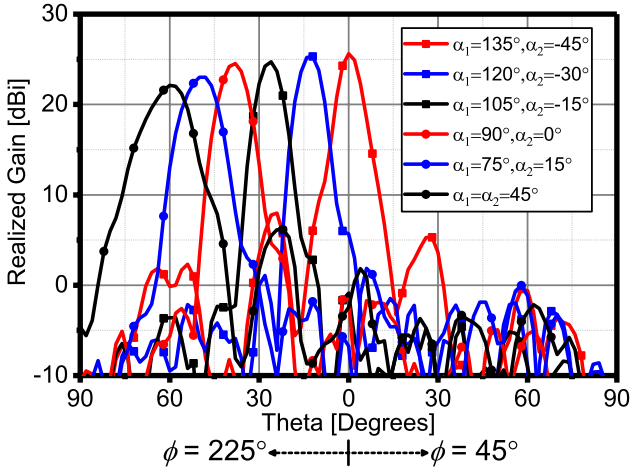

(c)

Figure 4.9: Measured radiation patterns of the fabricated mechanical beam-steering antenna system at 9.78 GHz in the (a) E-plane, (b) H-plane, and (c) D-plane.

measurement chamber, with the setup shown in Fig. 4.8. A styrofoam fixture was used to position the bottom PSS at a distance of 172.5 mm from the feed horn antenna. Multiple acrylonitrile butadiene styrene (ABS) washers were used to separate the two PSSs by a distance of 2 mm. I experimentally characterized the beam scanning performance of the antenna system in three principal planes (E-plane, H-plane, and D-plane) in the near-field spherical measurement chamber. In each plane, radiation patterns were measured for six different cases where the main beams were generated at $\theta = 0°, 13°, 26°, 38°, 49°$ and $60°$, respectively. Observed that the center frequency of the fabricated prototype shifted from 10 GHz (as the intended operating frequency) to 9.78 GHz. This frequency shift can be attributed to fabrication tolerances and uncertainties in material properties of the fabricated PSSs.

Figs. 4.9(a)-(c) show the measured co-polarization patterns in the E-plane, H-plane and D-plane respectively. Observe that the main beam can be scanned from the broadside direction to a maximum scan angle of 60° in the E-plane, H-plane and D-plane with the maximum scan loss of 3.5 dB, 3.4 dB and 3.5 dB, respectively. The maximum realized gains of the broadside beams in the E-plane, H-plane, and D-plane are 25.8 dBi, 25.8 dBi and 25.6 dBi, respectively, corresponding to the aperture efficiencies of 29.1%, 29.1% and 27.8%, respectively. This relatively low aperture efficiency is mainly due to the low f/D ratio of the structure and the transmission loss of the PSSs. The differences between the simulated and measured peak gains are less than 0.5 dB for all scan angles. These discrepancies were likely due to misalignment between the feed antenna and the PSSs, and the elements present in the measurement setup that were not taken into account in the full-wave simulation model (e.g., styrofoam fixture to position the PSSs, dielectric spacers to separate the two PSSs, and cable connecting the feed antenna to the chamber test port). The measured side lobe levels are less than -15 dB for every scan angle in each plane except for the case of 60° scan angle in the H-plane, where the maximum side lobe level is -13.1 dB. The fabricated prototype shows very good polarization purity of at least 20 dB for all the measurement cases.

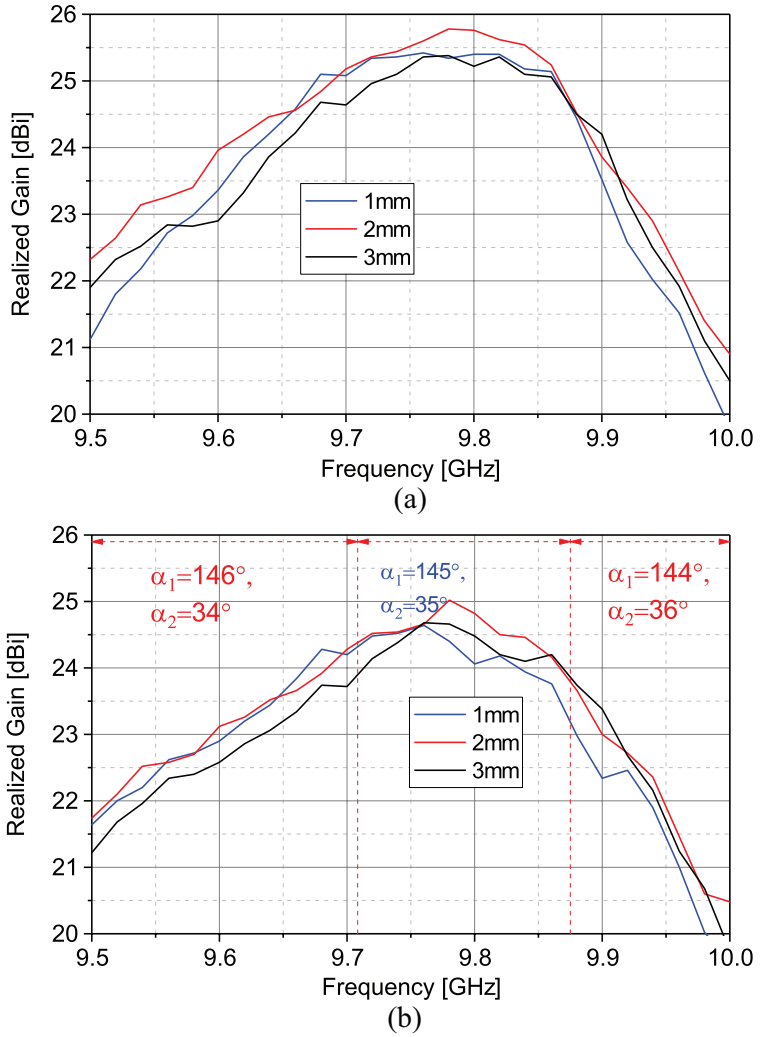

Figure 4.10: Measured realized gains as a function of frequency at (a) $\theta = 0°$ and (b) $\theta = 30°$ in the H-plane for different distances between the two PSSs. For $\theta = 30°$, the rotation angles are marked for different frequencies. For $\theta = 30°$, the rotation angles of the prisms must be changed with frequency to maintain the desired beam direction.

Additionally, I evaluated the bandwidths of the antenna system for two cases where the main beams are generated at $\theta = 0°$ and $30°$, respectively, where the distance between the PSS was varied from 1 mm to 3 mm, as shown in Fig. 4.10. Among the measured cases with different distances between the PSSs, the distance of 2 mm provided the highest realized gains for most of the measured frequency points. I also observed that the maximum realized gain of 2 mm distance was approximately 0.5 dB higher than the other cases at the center frequency. For the distance of 2 mm case, the measured 3-dB gain bandwidth is 4.2% at

broadside direction and 5.3% for $\theta = 30°$. This bandwidth is primarily determined by the low f/D ratio of the antenna and the single-frequency nature of the design and optimization process of the device.

Table 4.3: Comparison of the main beam directions acquired from the theoretical calculations and measurement results in the (a) E-plane, (b) H-plane, and (c) D-plane.

Theoretical results	0°	13°	26°	38°	49°	60°
Measurement (E-plane)	0°	14°	27°	39°	50°	60°
Measurement (H-plane)	0°	13°	26°	38°	49°	59°
Measurement (D-plane)	0°	13°	26°	38°	49°	59°

I also assessed the beam pointing accuracy of the fabricated beam-steering antenna system by comparing the measured main-beam directions in the E-plane, H-plane and D-plane with the values calculated using theoretical formulas. The theoretical results were derived by assuming that the total phase gradient of the output aperture is the linear combination of the phase gradient vectors of the two PSSs, which were determined in the design procedure. With this assumption, the total phase gradient vector was calculated based on the rotation angles of the PSSs and used in conjunction with $kd\sin\theta = \Delta\phi$ to calculate the main beam direction θ for each beam scan scenario. Table 4.3 reports the main beam directions acquired from the measurement results and theoretical calculations for different beam scan scenarios. The measurement and theoretical results agree very well with each other as the maximum beam pointing errors are 1° for all cases.

4.4 Conclusion

This chapter presented a mechanical beam-steering antenna system operating at X-band and exploiting the Risley prism concept. Low-pass FSS unit cells were designed to provide the desired phase profiles for the two PSSs used in the antenna system. I used a co-design approach that chose optimal designs for unit cells while simultaneously varying their spacing.

The optimization metric was to maximize transmission through two cascaded unit cells spaced by the best distance for those two unit cell designs. This method was validated by both simulation and measurement results. A prototype of the proposed beam-steering system was fabricated and experimentally characterized. The simulation and measurement results show reasonable agreement and verify a good beam scanning performance of the proposed antenna system. The measured radiation patterns show that the main beam can be scanned from broadside direction to 60° in the upper hemisphere within a gain variation of less than 3.6 dB. The beam pointing errors are less than 1° within the scan range for the fabricated beam-steering antenna system. The low-complexity, high efficiency, and good beam steering performance of the proposed antenna system make it a promising candidate for affordable phased-array antennas.

Chapter 5

A Low-Profile, Risley-Prism-Based, Beam-Steerable Antenna Employing a Single Flat Prism

The full manuscript was published as:

Z. Zhang, Y. C. Zhong, H. Luyen, J. H. Booske and N. Behdad, "A low-profile, Risley-prism-based, beam-steerable antenna employing a single flat prism," *IEEE Trans., Antennas Propag.*, 2022. In Press. Doi: 10.1109/TAP.2022.3161562

5.1 Introduction

Beam-steerable antennas can be categorized into two broadly-defined groups of conventional (active/passive) phased-arrays and those that use low-complexity beam-steering techniques. Traditional phased-array antennas electronically manipulate the phase shift of each array element to control the radiation patterns of the array [1–3, 63, 112]. Many phased-array antennas have been developed for adaptive beam steering in various applications ranging from satellite and airborne communications to imaging systems. However, due to their inherent complexity, such phased-arrays are usually costly to implement. Furthermore, in situations where high power handling capability may be needed, the thermal management issues and the limited power handling capability of the phase shifters or T/R modules used in conventional phased-arrays causes additional design challenges that need to be addressed [1–3]. This has been the motivation for developing low-complexity and low-cost beam-steering techniques. Among low-complexity beam-steering techniques reported in the literature, several rely on using micro- or macro-scale mechanical movements of parts or all of the aperture to perform beam steering [44–52]. Compared to conventional phased-array antennas, mechanically beam-steerable antennas do not use any electronic phase shifting mechanisms. Thus, they benefit from lower losses, have reduced cost, and are often better suited for high-power applications. This, however, comes at the expense of reduced scanning speeds. Therefore, in applications that prioritize high-power handling, lower cost, and reduced complexity over high-speed beam scanning, mechanical beam steering techniques may present good alternatives to conventional active or passive electronically steered arrays.

Recently, mechanically beam-steerable antenna systems based on the Risley-prism concept have attracted attention for their simplicity and good beam scanning performance [53–58, 115]. In the optical regime, a Risley-prism system typically consists of a pair of rotatable wedge-shaped prisms used in conjunction with a well-collimated beam of light (e.g., a laser beam) [59, 60]. The beam can be steered when the prisms are rotated with

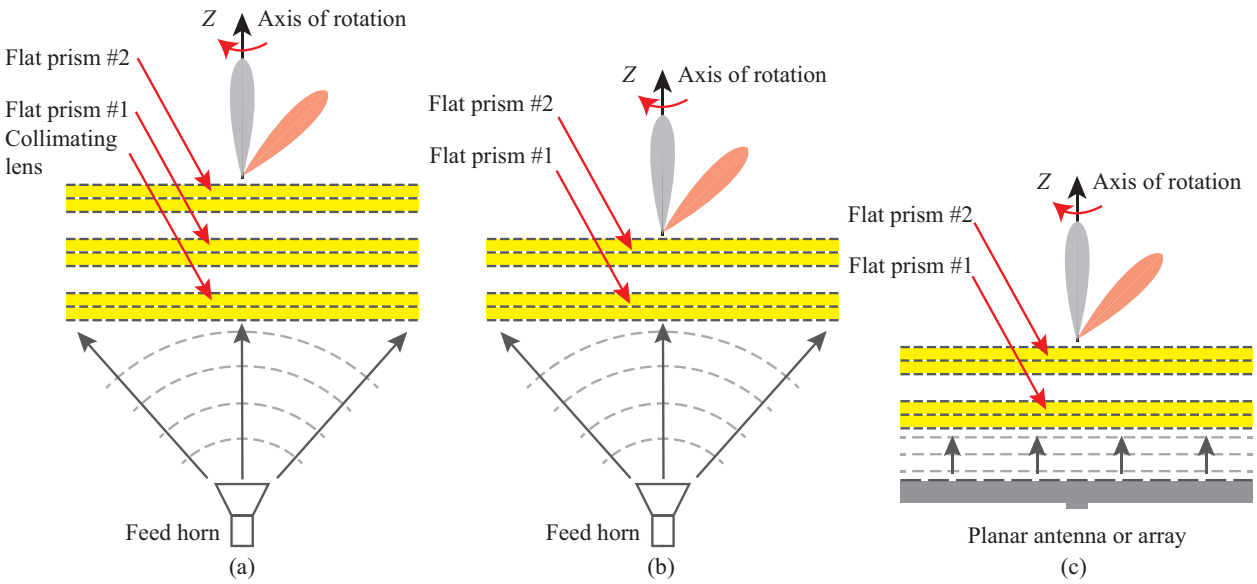

Figure 5.1: Different configurations of the Risley-prism-based beam-steerable antenna system reported in the literature. (a) A system employing a feed horn, a collimating lens, and two flat prisms (used in [53]). (b) The system in part (a) in which the collimating lens is integrated with the first prism (used in [53–55, 115]). (c) The system in part (a) in which the horn antenna is replaced with a planar antenna or antenna array placed in close proximity to the two flat prisms (used in [56, 57]). In such a system, a collimating lens is not needed.

respect to each other. In the microwave regime, different configurations of Risley-prism-based beam-steering systems [53–58, 115] have been proposed and implemented. Fig. 5.1 shows three different configurations of Risley-prism-based beam-steerable antenna systems used at microwave frequencies [53–57, 115]. Fig. 5.1(a) shows the architecture of the first reported beam-steerable antenna that employed the Risley-prism concept. Here, the two wedge-shaped prisms used in optical systems were replaced by a pair of flat prisms, illuminated by a feed antenna. The spherical wave radiated by the feed antenna is collimated by the lens placed below the two flat prisms. The relative rotational displacement between Prism #1 and Prism #2 provides beam steering in both azimuth and elevation directions in the upper hemisphere of the outgoing aperture. This design configuration was demonstrated for beam steering systems working at Ka-band with a $\pm 75^{\circ}$ scan range [53]. The configuration is relatively complex because it uses two flat prisms and a collimating lens, each of which is implemented with multiple metal and dielectric layers. Furthermore, this design

has a high overall profile of 8.3 λ_0 at 30 GHz. The structure shown in Fig 5.1(b) combines the collimating lens with the bottom flat prism. It not only collimates the spherical wave radiated by the feed antenna but also provides the corresponding phase gradient needed from the first prism for beam steering. This architecture of a Risley-prism-based beam-steering antenna was used in [54] and [55]. Reference [54] presented a high-power-capable beam steering lens antenna to work at X-band with a $\pm 20^\circ$ beam scan range. In [55], a planar Risley-prism-based system was reported to generate a quasi-nondiffractive beam at Ka-band with a $\pm 54^\circ$ beam scan range. However, these structures still have an overall profile of 17.15 λ_0 at 9.375 GHz in [54] and 17.4λ_0 at 28 GHz in [55] due to the usage of the horn antenna, which must be placed at some distance from the input aperture of the collimating lens/first prism. This high overall thickness motivated the development of the low-profile Risley-prism-based beam-steerable antenna architecture shown in Fig 5.1(c). Here, the horn antenna was replaced by a planar antenna or an array to achieve a low-profile beam steering system [56, 57]. In [56], a Fabry–Perot resonator antenna was used to feed the two prisms to steer the main beam with a $\pm 51^\circ$ range. This antenna system provides a peak gain of 19.4 dBi with a corresponding aperture efficiency of 19.2%. In [57], a dual-linear-polarized continuous transverse stub array was implemented to illuminate the two prisms and achieved a $\pm 40^\circ$ beam scan range with an aperture efficiency of 17.8%. Although these two works presented low-profile designs (1.27 λ_0 at 11 GHz [56], and 1.17 λ_0 at 12.35 GHz [57]), they still required the use of two flat prisms along with one antenna or planar array as a main feed. Each additional prism introduces ohmic and reflection losses, resulting in reductions of aperture efficiency and peak gain of the beam steering system. Furthermore, each flat prism is generally implemented by multilayer printed circuit boards, which add to the cost and weight of the antenna system.

In this chapter, I present a compact and low-profile Risley-prism-based beam-steerable antenna system that uses only a single flat prism. The proposed beam-steerable antenna consists of two parts: a holographic leaky-wave antenna and a PSS layer acting as a flat prism

placed on top of it. The holographic leaky-wave antenna provides an electric field distribution with a linear phase shift gradient over the input aperture of the flat prism. Therefore, only a single flat prism with the same phase gradient is needed to perform the beam steering. This leaky-wave antenna is easy to implement and has a single patterned metal layer. This architecture further reduces the loss, weight, cost, and complexity of Risley-prism-based beam steerable antenna systems and offers an improved aperture efficiency. Beam steering in this system is achieved by rotating the flat prism and the leaky-wave antenna against each other. Since the feed antenna is also rotated, the proposed approach is only suitable for designing circularly-polarized beam-steerable antennas. If the leaky-wave antenna is linearly-polarized, beam scanning can be performed but the polarization of the antenna will also change as a function of scan angle, which is generally not desirable. In circularly-polarized systems, however, physically rotating the feed antenna does not adversely impact the polarization of the radiated wave.

In this design, the bottom holographic leaky-wave antenna was constructed using an array of sub-wavelength metallic patches with slits, placed on a grounded dielectric substrate. The flat prism was implemented using a low-pass PSS with hexagonal unit cells. 2D beam scanning in elevation and azimuth is achieved by rotating the top flat prism and leaky-wave antenna with respect to each other. A prototype antenna with an overall thickness of only 1.1 λ_0 at 10 GHz was designed, fabricated, and experimentally characterized. The antenna has a measured peak gain of 22.3 dBc and a corresponding aperture efficiency of 34.5%. The main beam of the antenna can be scanned from the broadside direction to a maximum scan angle of $\pm 57^\circ$ in 2D with a maximum scan loss of 3.6 dB.

5.2 Principles of Operation

Fig. 5.2 shows the structure of the proposed Risley-prism-based beam-steerable antenna system. The antenna system includes a holographic leaky-wave antenna and a flat prism placed

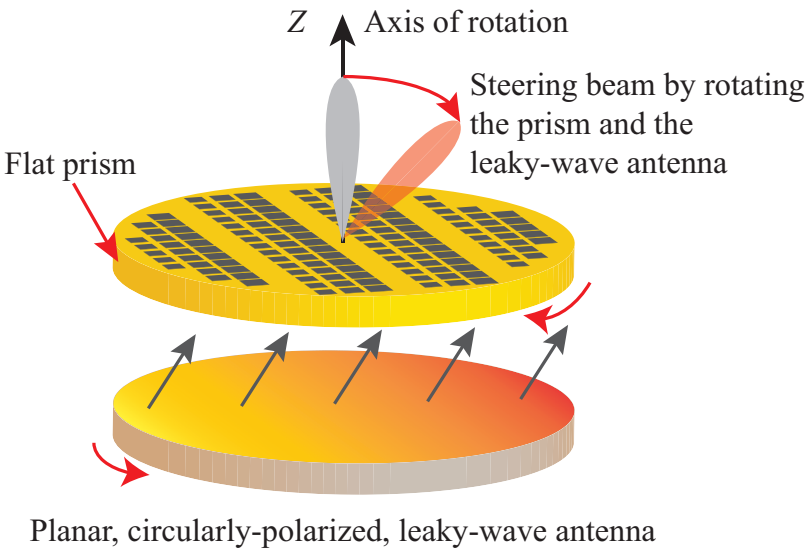

Figure 5.2: 3-D topology of the proposed mechanically beam-steerable antenna system using a simplified Risley prism structure.

on top of it. The leaky-wave antenna is designed to provide an electric field distribution with a linear phase-shift gradient over its output aperture. Due to the leaky-wave nature of the antenna, the amplitude of this electric field distribution is not uniform. Therefore, the electric field at the output aperture of the leaky-wave antenna resembles the field generated by a horn antenna, which is then collimated by a lens and passed through a flat prism that provides a linear phase shift gradient, as shown in Fig. 5.1(a). This way, the leaky-wave antenna in a single layer offers the same function achieved by the combination of the feed antenna, collimating lens, and the first flat prism in the setup shown in Fig. 5.1(a). However, as the polarization of this antenna system needs to be maintained when the leaky-wave antenna and the flat prism are rotated against each other, the system needs to be circularly polarized. Therefore, the holographic leaky-wave antenna was designed to be right-hand circularly polarized. Thus, when the leaky wave antenna and the top prism are rotated with respect to each other, the antenna polarization does not change.

In this work, I designed the leaky-wave antenna and the flat prism layer to provide the same phase gradient for simplicity. The relationship between the main beam direction of the beam-steerable antenna system and the rotation angles of the two layers is shown in Fig. 5.3.

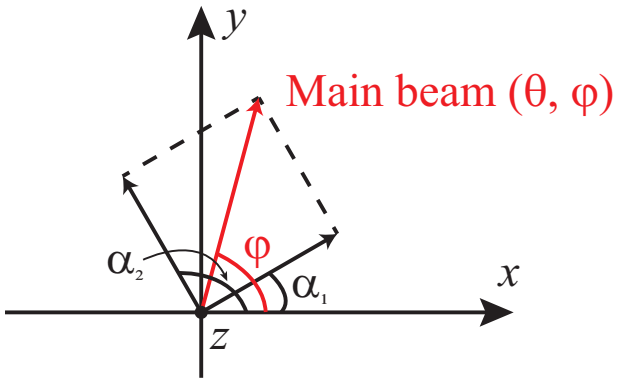

Figure 5.3: The direction of the main beam can be calculated based on the relative rotation angles of the leaky-wave antenna and the flat prism. Black arrows show the directions of the phase shift gradients of the two layers and the red arrow shows the direction of the steered beam. α_1: rotation angle of the leaky-wave antenna. α_2: rotation angle of the top flat prism.

In this case, the direction of the phase-shift gradient provided by each layer is shown with an arrow. The elevation and azimuth angles of the main beam are denoted by θ and φ, while the rotation angles of the leaky-wave antenna and the flat prism are denoted by α_1 and α_2, respectively. In Fig. 5.3, two vectors with the same length are used to represent the equivalent phase gradient of the leaky-wave antenna and the top flat prism. The azimuth angle of the main beam, φ, can be represented as $\varphi = (\alpha_1 + \alpha_2)/2$. Accordingly, the relative rotation angle, ζ, with respect to the main beam direction, can be written as $\zeta = |\varphi - \alpha_1|$ or $\zeta = |\varphi - \alpha_2|$.

When the top prism and holographic leaky-wave antenna are rotated with respect to each other, the equivalent phase gradient at the output aperture changes. It can be calculated as a linear combination of the two phase gradient vectors and changes as a function of the relative rotation angles of the two surfaces, ζ. Then, the elevation angle of the main beam direction, θ, can be expressed as

$$kd \sin\theta = 2\Delta\phi \cos\zeta \tag{5.1}$$

where k is the wave number in free space, d is the unit cell's size, and $\Delta\phi$ is the phase

difference between two adjacent unit cells along the phase gradient direction of the top PSS. As a result, the main beam of the outgoing wave can be pointed anywhere within a cone with an apex angle of $2\theta_0$, where θ_0 is the maximum scan angle corresponding to the maximum phase gradient of $2\Delta\phi/d$. θ_0 can be calculated as

$$\theta_0 = \arcsin(\frac{2\Delta\phi}{kd}). \tag{5.2}$$

A comprehensive study of the relationship between the main beam directions and the rotation mechanism was presented in [56].

In this design, a maximum scan angle of 57° was selected to design a proof-of-concept prototype of the proposed beam-steerable antenna system. Therefore, to get the same equivalent phase gradient as the top PSS, the leaky-wave antenna needs to provide a phase shift gradient over its aperture that corresponds to a far-field beam directed towards $\theta = \arcsin(\Delta\phi/kd)$, which can be calculated as $\theta = \arcsin(\sin\theta_0/2) = 25°$.

5.3 Holographic Leaky-Wave Antenna

The leaky-wave antenna employed in this work is designed based on the holographic impedance modulation concept (also known as the modulated surface impedance) [116–123].The holographic technique has several advantages in comparison with classical leaky-wave antenna design techniques. Specifically, the design procedure is relatively simple, the antenna does not need complex feeding networks, and it is relatively easy to control the radiation pattern characteristics such as polarization [119], beam shape [120], and the number of beams [123].

5.3.1 Basic Concept

Originally developed in the optical regime, holography can fully record and reconstruct a 3D image of an object. The holographic technique has been recently employed for antenna

design. Here, I only review the basic concepts of the holographic technique for the sake of brevity.

Two main steps are needed to implement the holographic leaky-wave antenna [116]. First, the holographic impedance surface is recorded with respect to the object wave and reference wave, which correspond to the desired radiation pattern and antenna feed, respectively. Then, the object wave is reconstructed by exciting the reference wave on the holographic impedance surface. In this design, a short monopole fed with a coaxial cable was used to feed the holographic leaky-wave antenna. Since the vertical linearly-polarized wave excited by the monopole antenna needs to be transformed into a circularly-polarized wave, a tensor artificial impedance surface was used [116]. Specifically, I used anisotropic circular slotted metal patches as the constituting elements of the holographic tensor artificial impedance surface.

5.3.2 Implementation of Artificial Impedance Surface

According to the holographic artificial impedance theory, the tensor impedance can be expressed as

$$\begin{aligned}\overline{\overline{Z}} = j \begin{pmatrix} X & 0 \\ 0 & X \end{pmatrix} \\ + j\tfrac{M}{2} \operatorname{Im}\left(\overrightarrow{E}_{rad} \otimes \overrightarrow{J}^{*}_{surf} - \overrightarrow{J}_{surf} \otimes \overrightarrow{E}^{*}_{rad} \right)\end{aligned} \tag{5.3}$$

where $\overrightarrow{E}_{rad}$ is the radiated electric field, corresponding to a RHCP wave in this design, and $\overrightarrow{J}_{surf}$ is the surface current excited by the monopole antenna. Operators $\otimes$ and * represent the outer product and the complex conjugate operation, respectively. X and M parameters are the selected average impedance value and the modulation depth, respectively. For a monopole antenna placed at the origin of the coordinate system, J_{surf} can be written as

$$J_{surf} = \frac{(x, y, 0)}{r} e^{-jknr} \tag{5.4}$$

where it is assumed that the holographic artificial impedance is placed on the $x-y$ plane, $r=\sqrt{x^2+y^2}$, and n is the effective refraction index seen by the surface currents. To radiate a circularly-polarized wave with the main beam at $(\theta, 0^\circ)$, E_{rad} can be written as

$$E_{rad} = (j\cos\theta, 1, -j\sin\theta)e^{-j\vec{k}\cdot\vec{r}} \tag{5.5}$$

Then the tensor impedance can be derived as

$$Z_{xx} = X + M\frac{x}{r}\cos\theta\cos\gamma \tag{5.6}$$

$$Z_{xy} = \frac{M}{2}(\frac{y}{r}\cos\theta\cos\gamma - \frac{x}{r}\sin\gamma) \tag{5.7}$$

$$Z_{yy} = X - M\frac{y}{r}\sin\gamma \tag{5.8}$$

where $\gamma = kx\sin\theta - knr$.

Using this approach, I designed a holographic leaky-wave antenna radiating a RHCP wave at $\theta = 25^\circ$, at 10 GHz. I employed an array of circular metallic patches with variable sizes and variable slot angles to realize the tensor impedance surfaces. The unit cell of the structure was designed using a grounded dielectric substrate with a thickness of 1.27 mm (Rogers RO3010). Each unit cell has dimensions of 3 mm × 3 mm, corresponding to $\lambda_0/10$ × $\lambda_0/10$. In this design, I used the average reactance of X = 316 Ω, and the reactance modulation depth of M = 136 Ω to span the entire available impedance range. Fig. 5.4 shows the perspective views of the holographic leaky-wave antenna.

I conducted full-wave simulations in Ansys HFSS to calculate the impedance of a unit cell in a periodic environment. In doing so, only two parameters were changed: the radius of the circular patch (1~1.4 mm) and the rotation angle of the slot (0°~360°), while fixing the width of the slot at 0.2 mm. After sweeping these two parameters in Ansys HFSS, the relation between the impedance and the radius and rotation angle was computed in Matlab using the full-wave computed impedance data. For a detailed explanation of this process,

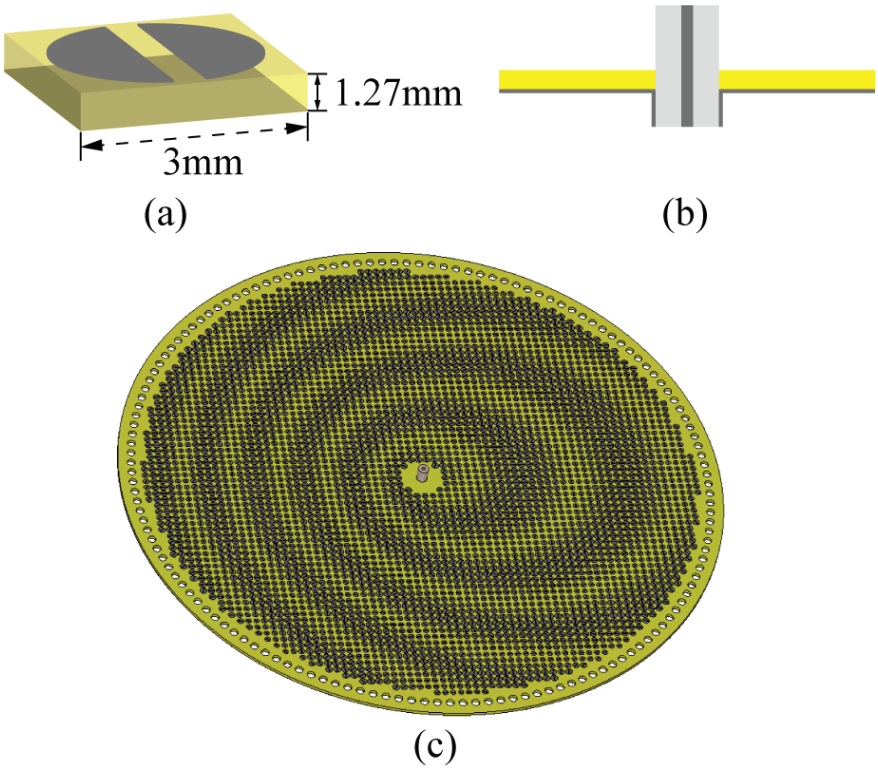

Figure 5.4: (a) 3D view of the unit cell of the leaky-wave antenna. (b) The cross-sectional view of the monopole antenna used to excite the leaky-wave antenna. (c) 3D topology of the holographic leaky-wave antenna. Black and yellow represent metal and dielectric substrate, respectively.

the interested reader is referred to [116].

5.3.3 Simulation and Measurement Results

A prototype of the leaky-wave antenna was fabricated using printed circuit board lithography and its photograph is shown in Fig. 5.5. The outer diameter of the prototype is 230 mm. On the periphery of the board, an array of circular-shaped holes with diameters of 3 mm were drilled. The effective aperture diameter of the leaky-wave antenna is 213 mm, equivalent to 7.1 λ_0 at 10 GHz. Furthermore, in order to meet the fabrication requirements on a 9" $\times$ 12" Rogers RO3010 substrate board, the PCB board was cut on the one side to be 8" long. Therefore, the effective aperture area was calculated to be 352 cm^2. The leaky wave antenna was excited by a monopole connected to a coaxial connector. The monopole was located

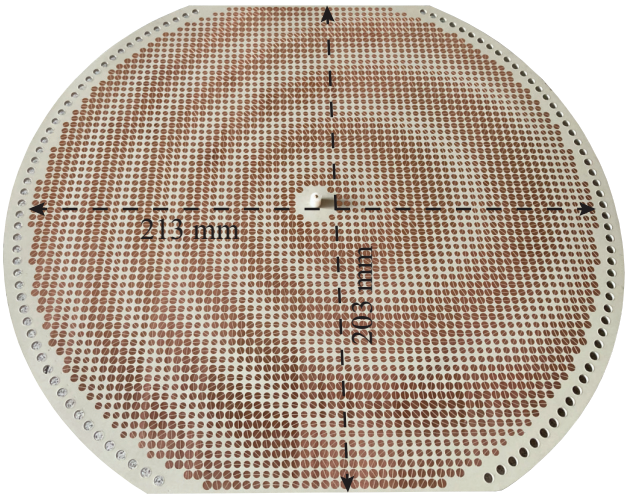

Figure 5.5: Photographs of the fabricated holographic leaky-wave antenna.

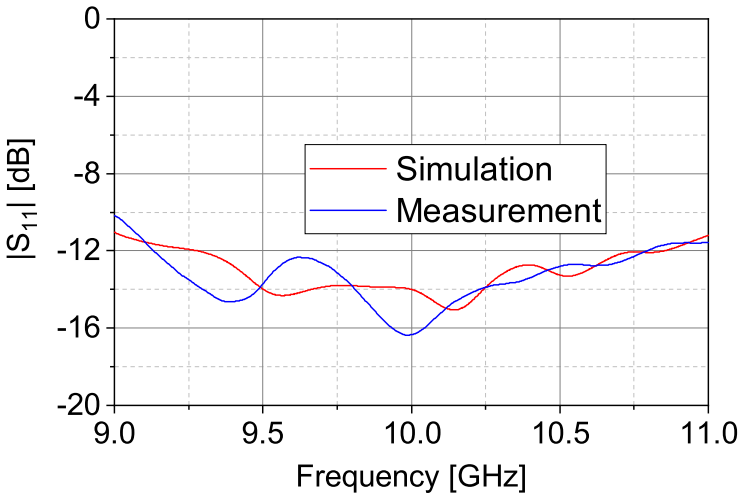

Figure 5.6: Magnitudes of the simulated and measured S_{11} of the leaky-wave antenna.

at the center of the leaky-wave antenna. 21 slotted patches in the center were removed for mounting the monopole antenna and achieving a good impedance match. The length of the monopole antenna above the ground plane is 6.5 mm. Fig. 5.6 shows the simulated and measured S_{11} of the proposed leaky-wave antenna. Both of the measured and simulated input reflection coefficients were below -10 dB from 9 to 11 GHz.

The fabricated prototype was experimentally characterized in a near-field spherical measurement chamber. Fig. 5.7 shows the measured and simulated radiation patterns of the leaky-wave antenna at 10 GHz. The full-wave simulation was conducted using CST Mi-

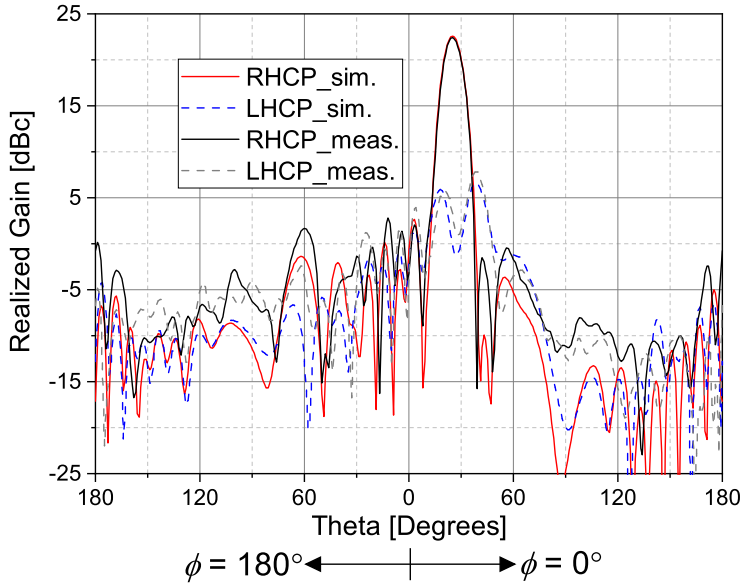

Figure 5.7: Simulated and measured radiation patterns of the holographic leaky-wave antenna at 10 GHz.

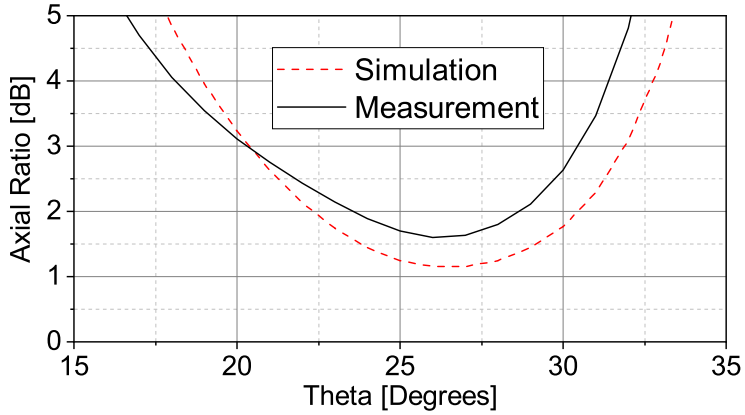

Figure 5.8: Measured and simulated ARs of the holographic leaky wave antenna at 10 GHz.

crowave Studio. The simulated peak RHCP realized gain is 22.6 dBc at $\theta = 25°$, corresponding to an aperture efficiency of 41%. The measured RHCP realized gain reaches its peak value of 22.4 dBc at $\theta = 25°$, corresponding to an aperture efficiency of 39%. The side lobe levels (SLLs) are below -19.5 dB. Fig. 5.8 shows the measured and simulated axial ratios (ARs). Observe that both are less than 3 dB at the main beam direction indicating the circularly-polarized nature of the radiated field.

Fig. 5.9 shows the measurement and simulation results for the maximum realized gains

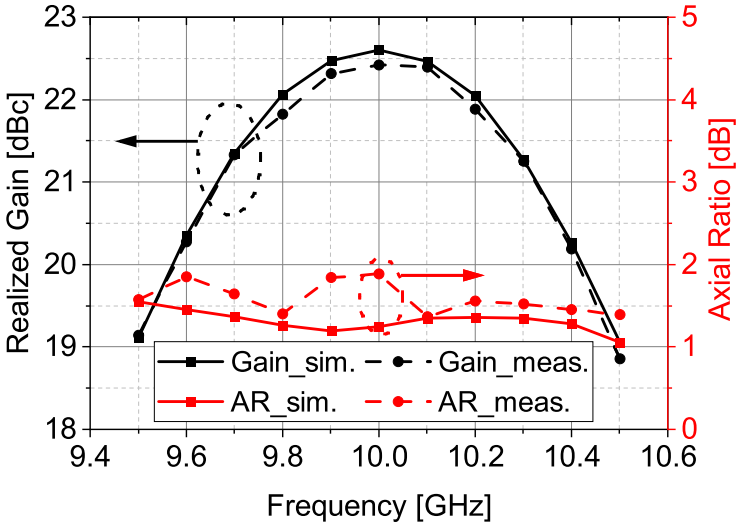

Figure 5.9: Measured and simulated maximum realized gains and ARs as a function of frequency for the holographic leaky-wave antenna.

and ARs as a function of frequency for the holographic leaky-wave antenna. Overall, the simulation and measurement results agree well. Observe that the simulated and measured 3 dB gain bandwidths are both 9.6–10.4 GHz, corresponding to 8% bandwidth. The measured and simulated ARs are all below 3 dB for the examined frequency range of 9.5-10.5 GHz.

5.4 Design of the Flat Prism Using Phase-Shifting Unit Cells

As shown in Fig. 5.2, while the bottom holographic leaky-wave antenna should be designed to have an oblique wavefront incident towards the top PSS, the top PSS must be designed to provide a linear phase gradient of $\Delta\phi/d$. As mentioned in Section 5.2, the relationship between the unit cell's period, d, the phase difference between two adjacent unit cells along the phase gradient direction, $\Delta\phi$, and the maximum scan angle of the radiated beam, θ_0, can be expressed as $kd\sin\theta_0 = 2\Delta\phi$. In this design, the phase progression between two adjacent unit cells along the phase gradient direction of the flat prism, $\Delta\phi$, was chosen to be 45°. This required eight different unit cells to cover the 0°-360° phase range. Then, the unit cell's

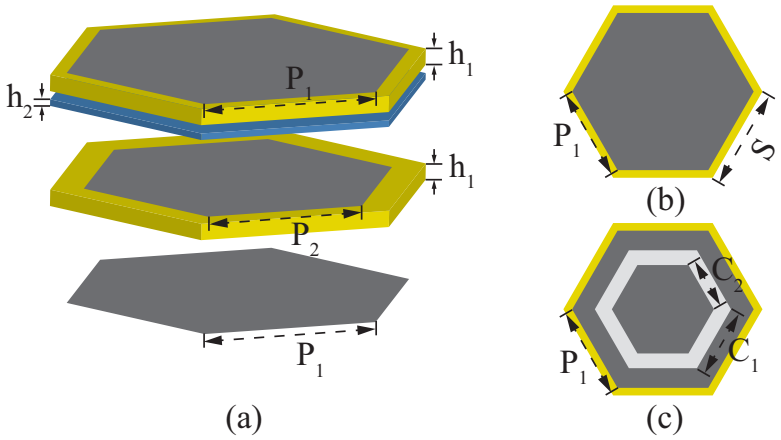

Figure 5.10: 3-D topology of the phase shifting unit cells employed to design the flat prism. (a) 3-D view. (b) Top view of Unit Cell 1 to Unit Cell 7. (c) Top view of Unit Cell 8. Black represents metal, yellow represents dielectric substrates, and blue represents bonding layers.

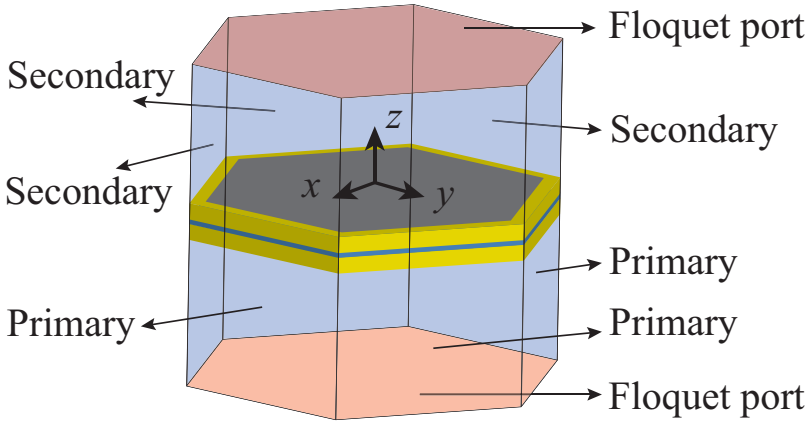

Figure 5.11: Simulation setup of the hexagonal-shaped unit cell in Ansys HFSS. Three pairs of primary-secondary boundary conditions were applied surrounding the unit cell. Floquet ports were used to excite the unit cell to calculate the transmission coefficients of the eight unit cells.

period, d, was calculated to be $d = 2\Delta\phi/(k\sin\theta_0)$, which was 9 mm (about 0.3 λ_0 at 10 GHz).

Eight phase shifting unit cell states were used to design the top flat prism, each of which is the unit cell of a suitably designed phase shifter. Collectively, these unit cells provide the phase profile for the flat prism needed to achieve 2D beam-steering when used in conjunction with the lower leaky-wave antenna. Hexagonal-shaped unit cells were used, shown in Fig. 5.10. Hexagonal-shaped unit cells are more rotationally symmetric and their

Table 5.1: Physical dimensions of the eight different unit cells used to design the flat prism.

Unit cell number	Phase shift (Degrees)	P_1 (mm)	P_2 (mm)	C_1 (mm)	C_2 (mm)
1	315	0	0	NA	NA
2	270	4	2	NA	NA
3	225	4.6	4.3	NA	NA
4	180	4.83	5.15	NA	NA
5	135	5.01	5.52	NA	NA
6	90	5.25	5.54	NA	NA
7	45	5.58	5.42	NA	NA
8	0	5.75	3.4	4.6	3.5

responses is less sensitive to the change of the polarization of the incident wave compared to their rectangular counterparts [124]. Each unit cell is composed of three metal layers sandwiching two dielectric substrates. The unit cells were implemented using Rogers RO5880 substrates, with thicknesses of $h_1 = 1.575$ mm and ϵ_r of 2.2, bonded together by 0.1 mm-thick Rogers RO4450F prepreg bonding layer with ϵ_r of 3.52. The unit cell structure was symmetric with respect to the center (second) metallic layer for simplicity. The dimensions of the hexagonal patches in the metallic layers were tuned in full-wave simulations of the unit cells with periodic boundary conditions in Ansys HFSS to achieve the desired transmission phases at 10 GHz. Fig. 5.11 shows the simulation setup of the hexagonal-shaped unit cell. Three pairs of primary-secondary boundary conditions were applied surrounding the unit cell. Since the unit cell's period is 9 mm, the side length of the hexagonal unit cell, S, was calculated to be 6 mm.

Table 5.1 lists the dimensions of the metallic patches in each unit cell corresponding to different phase shifts. For unit cell number 1 to unit cell number 7, the front and back hexagonal patches are the same, as shown in Fig. 5.10(b). However, as shown in Fig. 5.10(c), there are hexagonal slots in the front and back hexagonal patches for unit cell number 8. The hexagonal slot was implemented to achieve the desired phase shift by increasing the capacitance of this low-pass unit cell. Fig. 5.12 shows the magnitudes and phases of the

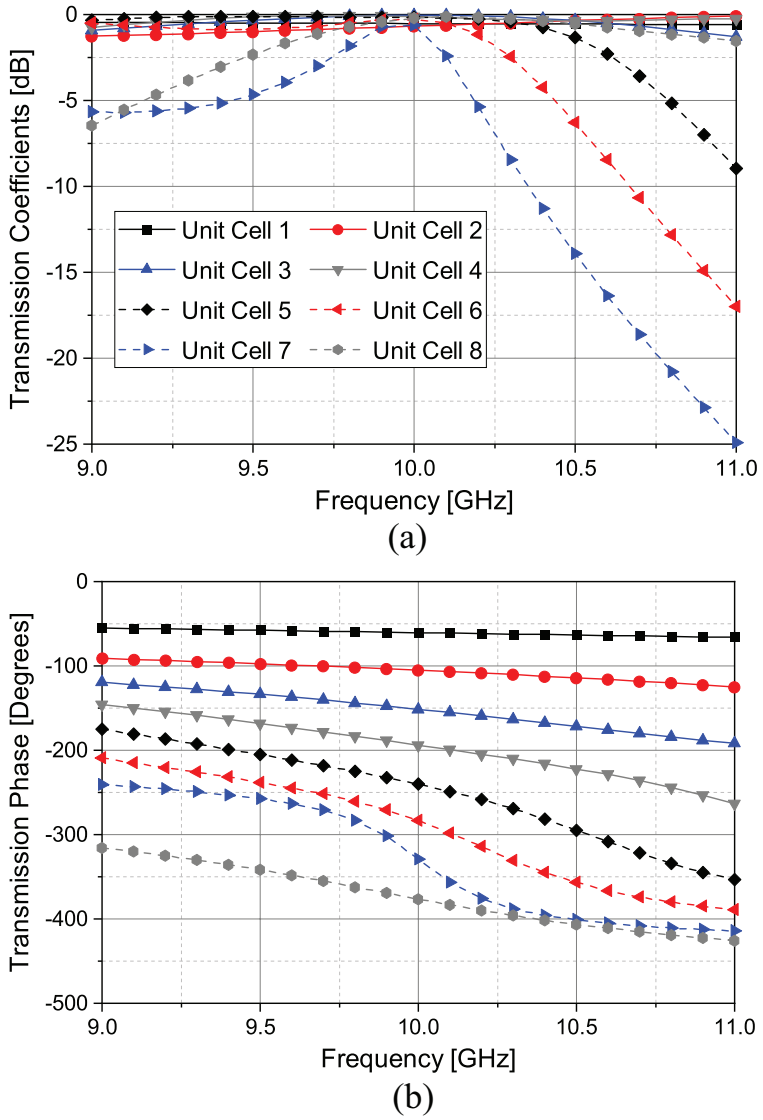

Figure 5.12: (a) Magnitudes and (b) phases of the simulated transmission coefficients of the eight phase shifting unit cells employed in designing the flat prism.

simulated transmission coefficients of different unit cells with RHCP incidence. All unit cells provide transmission coefficients higher than -0.7 dB at 10 GHz. The maximum transmission phase error in all eight unit cells is 2°. The transmission coefficients of all PSS unit cells are higher than -3 dB from 9.7 GHz to 10.1 GHz.

I also examined the frequency responses of the eight unit cells with respect to the elevation angle in the range of 0° to 40° with 10° increments with RHCP incidence. Fig. 5.13 shows the magnitudes and phases of the simulated transmission coefficients of the eight different unit

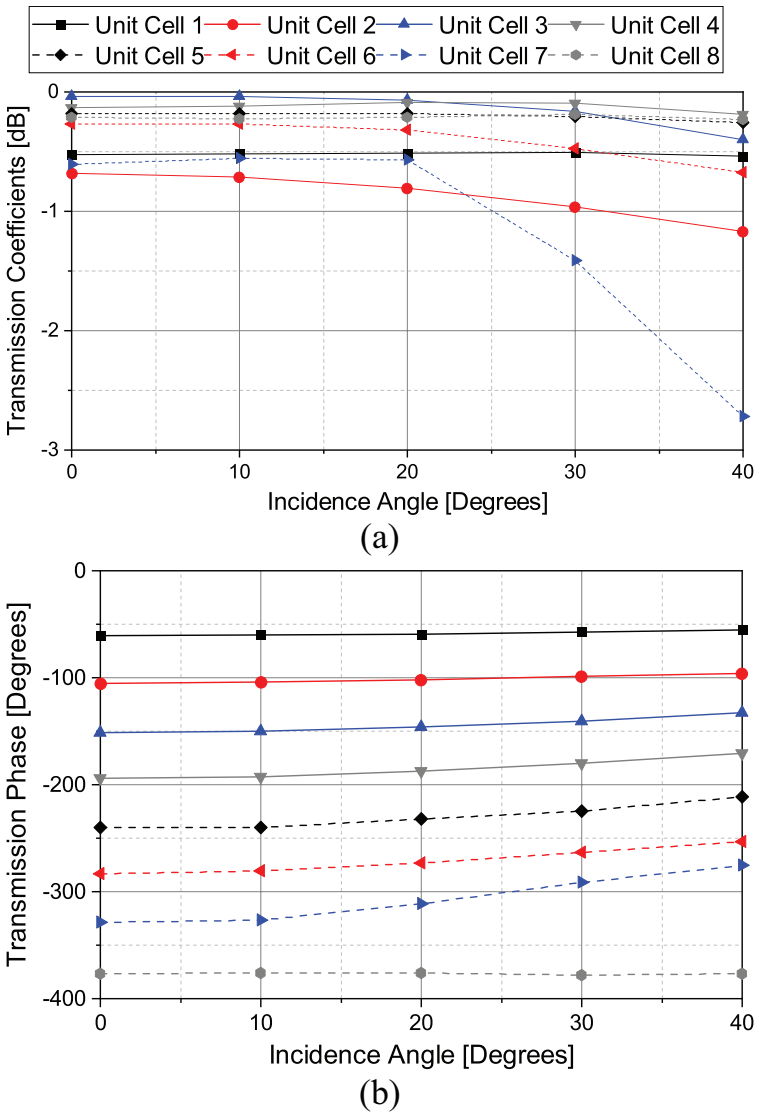

Figure 5.13: (a) Magnitudes and (b) phases of simulated transmission coefficients of the eight unit cell used in designing the flat prism. The results are obtained at 10 GHz for different incidence angles with RHCP incidence.

cells with different incident angles at 10 GHz. The magnitude responses of the eight unit cells are better than -1.2 dB at the operating frequency of 10 GHz for the examined incidence angles up to 40° except for unit cell 7. The phase responses of different unit cells vary for different incidence angles, but the responses are rather stable within a ±30° incidence angle range. The phase differences between the adjacent unit cells are within ±5° of 45° with a 30° incidence angle except for unit cells 6 and 7. Fig. 5.14 shows the magnitudes of the

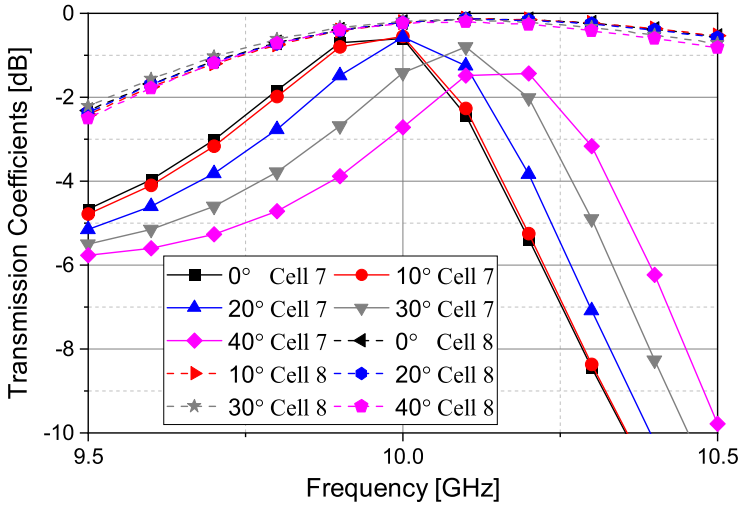

Figure 5.14: Magnitudes of the simulated transmission coefficients of unit cells 7 and 8 for different elevation angles with RHCP incidence.

simulated transmission coefficients of unit cells 7 and 8 with different incidence angles. All other unit cells under different incidence angles provide better transmission coefficients than unit cell 7 does, across the examined frequency range. However, the magnitudes of all of the transmission coefficients are better than -1.5 dB at 10 GHz for incidence angles within a $\pm 30^{\circ}$ range.

5.5 Simulation and Measurement Results of the Beam-Steerable Antenna System

I fabricated a prototype of the proposed low-profile beam-steerable antenna system for experimental verification. The top flat prism layer was fabricated from two Rogers RO5880 panels bonded with a single layer of Rogers RO4450F prepreg. Fig. 5.15 shows the top side of the PCB consisting of a 2D array of hexagonal-shaped unit cells.

Since the top prism was placed in the near-field region of the holographic leaky-wave antenna, the interaction between the flat prism and the holographic leaky-wave antenna would affect the overall performance of the beam steerable antenna system. Therefore, the

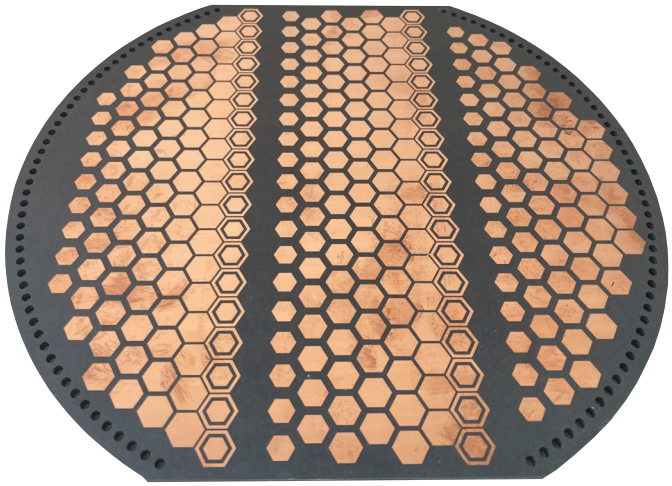

Figure 5.15: Photograph of the fabricated flat prism.

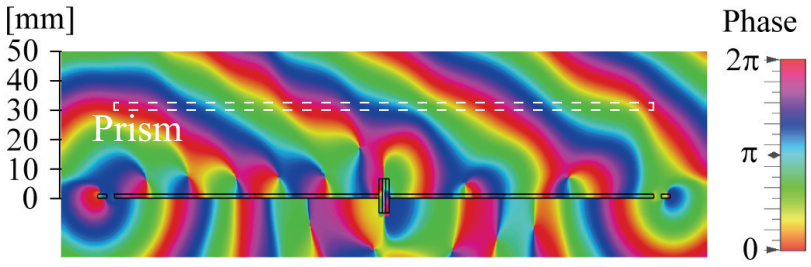

Figure 5.16: The phase of the simulated electric field distribution of the leaky-wave antenna in the near-field region.

distance between the flat prism and the holographic leaky-wave antenna is an important design parameter that needs to be determined. To determine the appropriate distance, two factors need to be taken into account. On the one hand, if the distance is increased, the field generated from the leaky-wave antenna would be more uniform at the input aperture of the flat prism and better resembles a planar wavefront with a linear phase shift gradient. However, increasing the distance will cause energy leakage from the edges of the leaky-wave antenna, thereby deteriorating the overall performance of this system. Moreover, the total profile of the whole antenna system is also increased. On the other hand, if the distance is too small, the loading effect of the flat prism on the leaky-wave antenna can be significant. This can adversely impact the radiation properties of the leaky-wave antenna and in turn the performance of the entire system.

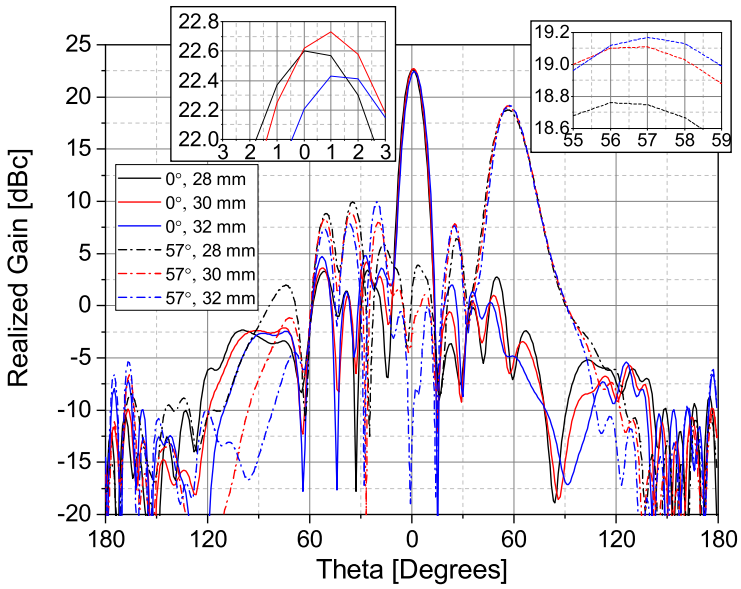

Figure 5.17: Simulated radiation patterns of the beam-steerable antenna system at 10 GHz for main beam steered towards $\theta = 0°$ and 57° for different distances between the flat prism and the leaky-wave antenna.

To identify the appropriate value for this separation distance, I simulated the electric field distribution in the near-field region of the holographic leaky-wave antenna. Fig. 5.16 shows the phase of the simulated electric field distribution in the upper hemisphere region. Observe that the EM waves radiated by the holographic leaky-wave antenna are nonuniform within a 30 mm space above the antenna aperture. At a distance of about 30 mm from the antenna aperture, the radiated EM waves appear almost like a plane wave with relatively uniform oblique phase distribution. Therefore, the top flat prism was put at a distance of 30 mm away from the leaky-wave antenna.

I also conducted full-wave simulations in CST Microwave Studio to evaluate the effect of the distance between the top flat prism and the leaky-wave antenna. The full-wave simulations include the complete model of the leaky-wave antenna and the top flat prism. Fig. 5.17 shows the radiation patterns of the antenna system configured to generate the main beams at $\theta = 0°$ and 57°, respectively, for three different cases where the distance between the top flat prism and the bottom holographic leaky-wave antenna was varied from 28 to 32 mm with 2 mm interval. At the broadside direction, observe that the distance of 30 mm

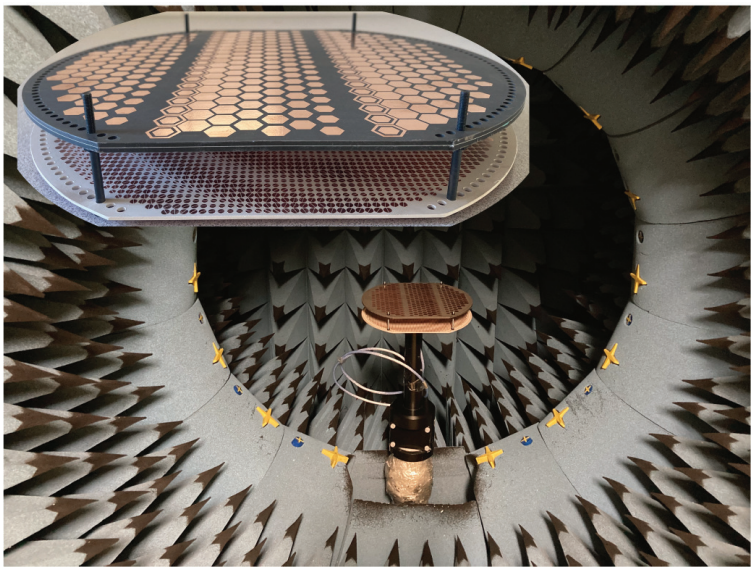

Figure 5.18: Photographs of the fabricated prototype and the measurement setup used to characterize the response of the antenna.

provides the highest realized gain (about 0.1 to 0.3 dB higher than the other cases). For the main beams that are generated at $\theta = 57°$, the distance of 30 mm provides the lowest SLLs. However, the realized gain of the 30 mm case is a little smaller than the realized gain value for the 32 mm case. After considering the overall performance of the Risley-prism-based beam-steerable antenna system at different distance values, I chose the distance of 30 mm between the prism and the holographic leaky-wave antenna for the final antenna system design and evaluated its beam scanning performance using full-wave simulations. Since the top PSS has the same size as the leaky-wave antenna, part of the power radiated by the leaky-wave antenna is not intercepted by the top PSS, resulting in spillover loss. To quantify the level of this loss, I conducted full-wave simulations with different PSS dimensions in CST. The distance between the PSS and leaky-wave antenna was not changed and remained at 30 mm. Using these simulations, the spillover loss was estimated to be approximately 0.3 dB.

I performed full-wave simulations of the beam-steerable antenna system in CST Microwave Studio and measured the performance of the fabricated prototype at 10 GHz. The simulated ohmic and dielectric losses of the antenna system were about 0.38 dB. The

Table 5.2: Simulated and measured realized gains, aperture efficiencies, ARs and SLLs for the radiation patterns shown in Fig. 5.19.

Scan angles	Peak gain [dBc]	Aperture efficiencies (%)	Axial ratio [dB]	SLL [dB]
0° (Sim.)	22.7	37.9	1.7	-18.5
0° (Mea.)	22.3	34.5	1.2	-19.6
15° (Sim.)	22.4	36.6	1.7	-18.1
15° (Mea.)	22.0	33.4	1.7	-17.8
30° (Sim.)	21.9	36.4	2.0	-19.6
30° (Mea.)	21.5	33.2	1.5	-18.9
45° (Sim.)	19.6	26.2	2.6	-15.6
45° (Mea.)	19.2	23.9	2.5	-14.3
57° (Sim.)	19.1	30.4	2.8	-10.2
57° (Mea.)	18.8	28.3	1.9	-8.0

fabricated flat prism and the holographic leaky-wave antenna prototypes were experimentally characterized in a near field spherical measurement chamber, with the setup shown in Fig. 5.18. Four long screws were used to position the top flat prism at a distance of 30 mm from the leaky-wave antenna in the experiment. I experimentally characterized the beam scanning performance of the antenna system in the near-field spherical measurement chamber. The radiation patterns were measured for five different cases where the main beams were steered towards $\theta = 0°, 15°, 30°, 45°$, and 57°, respectively. The reflection coefficients varied when rotating the top prism and the leaky-wave antenna against each other, but the simulated and measured reflection coefficients at the input port of the leaky-wave antenna were below -10 dB for all beam steering scenarios from 9.1 to 10.5 GHz.

Fig. 5.19(a) shows the measured co-polarization patterns of the Risley-prism-based beam steering antenna system at 10 GHz. Observe that the main beam can be scanned from the broadside direction to a maximum scan angle of 57° with the maximum scan loss of 3.6 dB. The rotation angles of the leaky-wave antenna and the top prism are, α_1, α_2= ±90°, ±72.5°, ±52.5°, ±30° and ±0°, for the main beam steered towards $\theta = 0°, 15°, 30°, 45°$, and 57°, respectively. α_1 and α_2 are denoted in Fig. 5.3. The measured peak gains are 22.7 dBc, 22.4

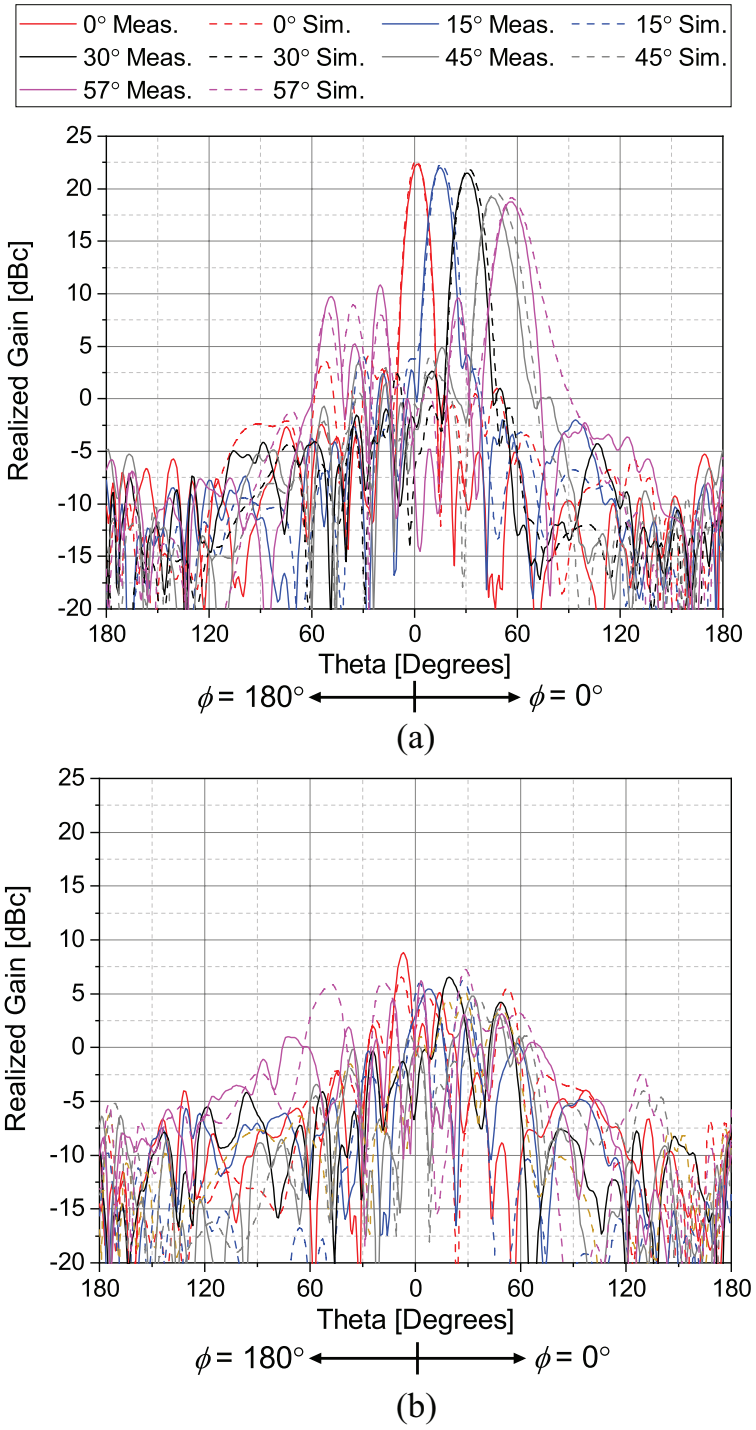

Figure 5.19: Measured and simulated radiation patterns of the proposed beam-steerable antenna at 10 GHz. (a) RHCP. (b) LHCP.

dBc, 21.9 dBc, 19.6 dBc, and 19.1 dBc for $\theta = 0°, 15°, 30°, 45°$, and 57°, respectively. This agrees quite well with the corresponding full-wave simulated gains of 22.3 dBc, 22.0 dBc,

21.5 dBc, 19.2 dBc, and 18.8 dBc for these scan angles. The peak realized gain drops 3 dB at $\theta = 44^\circ$ from the gain at the broadside direction for both the simulation and measurement results. This gain reduction is more than the best-case theoretical reduction, especially at large scan angles. One possible cause for this phenomenon is the relatively high transmission losses of the hexagonal-shaped unit cells with large oblique incidence angles. Fig. 5.13 shows that the unit cells have a higher transmission loss as oblique incidence angle increases. This effect would cause large scan loss when the main beam is scanned towards large elevation angles. Moreover, the edge truncation effect become more significant as the main beam is scanned towards large elevation angles due to the small aperture size. Other factors are the degraded unit cell performance due to non-periodic boundary conditions on the edge of the prism, and possibly the changing interaction between the leaky-wave antenna and the top prism when the beam is scanned off broadside. It is likely that the combined effects of all these factors contribute to different extents to the gain reductions observed in the experiments.

The simulated and measured aperture efficiencies are 37.9% and 34.5% for the broadside beams, respectively. The simulation and measurement results agree well on the general trend in the behavior of the beam steering antenna system. The differences between the simulated and measured peak gains are less than 0.4 dB for all scan angles. These small discrepancies were likely due to fabrication tolerances, uncertainties in dielectric properties of the dielectric substrates, and the presence of the metallic screws used to fix the relative positions of the two layers in the measurement setup that were not accounted for in the simulation model. The measured and simulated SLLs are less than -15 dB for every scan angle in each plane except for the case of 57° scan angle, where the simulated and measured maximum SLL are -10.2 dB and -8.0 dB, respectively. The high SLLs at large scan angles are likely because of the degraded performances of the unit cells located at the edges of the top PSS. These unit cells are designed to operate in a periodic environment but by virtue of their placement are operated in a non-periodic environment. The deviation from the ideal

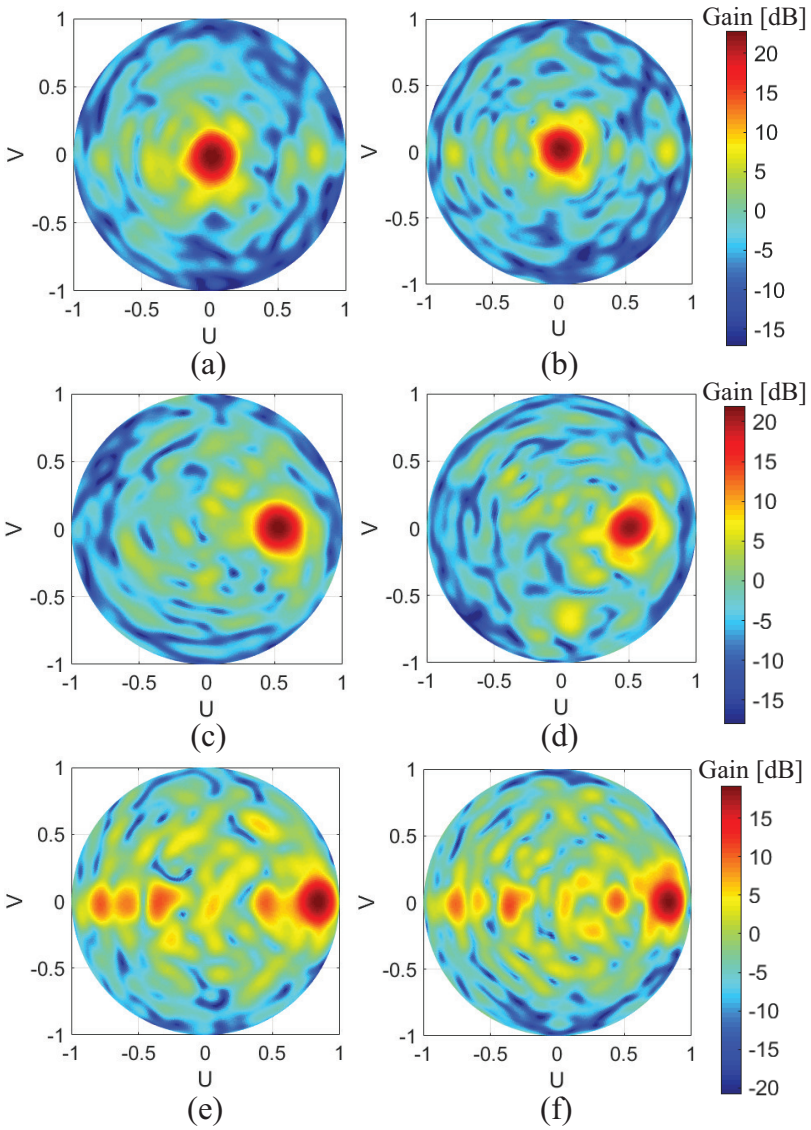

Figure 5.20: (a), (c), (e) Simulated and (b), (d), (f) measured 3D radiation patterns of the proposed beam-steerable antenna at 10 GHz in u-v spectral plane for the main beam steered towards (a), (b) $\theta = 0°$, (c), (d) $\theta = 30°$, and (e), (f) $\theta = 57°$.

periodic boundary conditions is especially more significant for larger scan angles since the unit cells near the edge cannot maintain their corresponding transmitted magnitude and phase responses. The degraded performance of the unit cells at the edge of the PSS would cause an abrupt discontinuity of the phase of the radiated electric field, which can result in a deteriorated SLL. Moreover, since my design has a relatively small aperture, this edge truncation effect becomes significant.

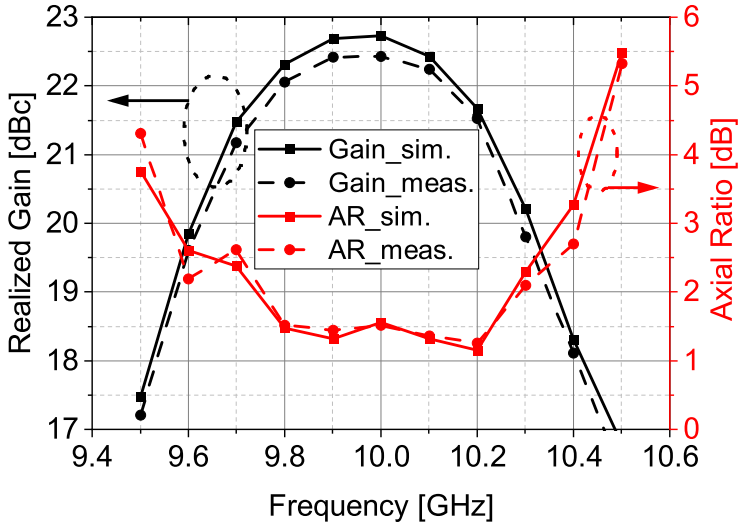

Figure 5.21: Measured and simulated maximum realized gains and ARs as a function of frequency for the Risley-prism-based beam steering antenna system.

Fig. 5.19(b) shows the measured LHCP radiation patterns of the beam-steerable antenna system at 10 GHz. The fabricated prototype shows very good polarization purity of at least 16 dB at the main beam directions for all the simulation and measurement cases. This indicates that the antenna maintains its circular polarization (AR less than 3dB) as the beam is scanned in the $\pm 57^{\circ}$ range. Table 5.2 summarizes the simulated and measured peak co-polarization realized gains, aperture efficiencies, ARs and maximum SLLs for all the radiation patterns shown in Fig. 5.19. The aperture efficiencies shown in Table 5.2 were calculated as: $\eta_{ap} = G\lambda^2/4\pi A_p$, where A_p is the area of the antenna's projected aperture, G is the simulated or measured peak gain at the main beam direction.

Fig. 5.20 shows the simulated and measured 3D radiation patterns at 10 GHz in the u-v spectral plane for the main beam steered towards $\theta = 0^{\circ}$, 30°, and 57°. The measured and simulated radiation patterns are similar to each other. Observe that although the SLL of the Risley-prism-based beam steering antenna system increases with the scan angle, no significant grating lobe was generated.

Fig. 5.21 reports the measured and simulated results for the maximum realized gains and ARs as a function of frequency for the Risley-prism-based beam steering antenna system

Table 5.3: Comparisons between the proposed design and other Risley-prism-based beam-steerable antennas reported in the past.

Ref.	Freq. [GHz]	Aperture dimension (λ_0)	Profile (λ_0)	Feed	Prism layers	Beam scanning range	Gain [dB]	Aperture efficiencies (%)
This work	10.0	7.1, Circular	1.10	Leaky-wave antenna	1	±57°	22.3	34.5
[53]	30.0	15.2, Circular	8.30	Horn antenna	2	±75°	28.0	21.7
[54]	9.4	8.0, Square	17.15	Horn antenna	2	±20°	26.3*	53.0
[56]	11.0	6.0, Square	1.27	Fabry–Perot resonator	2	±51°	19.4	19.2
[57]	12.4	5.1, Circular	1.17	Continuous transverse stub array	2	±40°	17.8	18.5
[58]	14.3	28.5, Circular	8.30	Continuous transverse stub array	3	±46°	38.1	80.5

*Calculated from the data provided in the paper.

that provides beam collimation at broadside direction. It can be seen that the simulated and measured 3 dB gain bandwidths are both 9.6–10.3 GHz, corresponding to 7% bandwidth. The measured AR bandwidth (less than 3 dB) is from 9.6 to 10.4 GHz, while the simulated result predicts a slightly narrower bandwidth of 9.6–10.3 GHz. The bandwidth of the Risley-prism-based beam steering antenna system is determined by the bandwidth of the leaky-wave antenna and the bandwidth of the hexagonal-shaped unit cells employed in the top prism.

I compared my design with other Risley-prism-based mechanical beam-steerable antenna systems reported in the literature [53, 54, 56–58] to highlight the advantages of the proposed approach. Table 5.3 shows the comparison regarding several key parameters of the mechanical beam steering antenna system. The primary advantage of this design over other reported Risley-prism-based beam-steerable antennas is its low profile and the fact that it uses only a single flat prism to steer the antenna beam in two dimensions. This helps with reducing

the loss and improving the aperture efficiency of the system. As can be seen from Table 5.3, the proposed design has the highest aperture efficiency when compared to the other low-profile Risley-prism-based antenna systems [56, 57]. My design also presents the largest beam scanning range among all the low-profile Risley-prism-based antenna systems. Finally, the present design has also the lowest overall thickness of only 1.1 λ_0 among the designs examined in Table 5.3. Because of these advantages, the proposed design is able to achieve 2D beam steering spanning $\pm 57^\circ$ with a low-loss, compact, low-profile, and low-complexity system.

The aperture efficiency of this design is lower than those of the mechanical beam steering systems reported in [54, 58]. This, however, is due to the differences between the feed mechanisms used in these designs. In particular, the designs reported in [54]] and [58] use high-profile, spatial feed techniques with large f/D ratios similar to that shown in Fig. 5.1(b). This helps reduce the amplitude tapering over the aperture of these designs, which results in a larger aperture efficiency. In the proposed design, the aperture efficiency is mainly determined by the bottom holographic leaky-wave antenna. The aperture efficiency of the holographic leaky-wave antenna is mainly determined by the product of tapering efficiency and conversion efficiency as discussed in [122]. The tapering efficiency accounts for the uniformity of the amplitude distribution of the incident wave over the surface of the leaky-wave antenna (e.g., tapering efficiency equals 1 for a perfectly uniform amplitude distribution). The conversion efficiency is defined as the capacity of the modulated holographic impedance surface to transform the surface wave excited by the monopole into radiated leaky-wave power. Since the designed holographic leaky-wave antenna only has a radius of 3.55 λ, the tapering efficiency and conversion efficiency are relatively low. The efficiency of the holographic leaky-wave antenna can be improved by increasing its physical aperture. Therefore, the overall aperture efficiency of the system can be improved by implementing the holographic leaky-wave antenna with a larger physical aperture.

5.6 Conclusion

This chapter presented a low-loss, low-profile Risley-prism-based beam-steerable antenna system operating at X-band. Unlike other Risley-prism-based beam-steerable antenna systems that require two prisms, the proposed design uses only a single flat prism. The feed antenna and the first flat prism used in most conventional Risley-prism-based beam-steerable antenna systems are replaced with a single holographic leaky-wave antenna in this design. This significantly reduces the overall thickness of the proposed beam-steerable antenna. Moreover, eliminating one of the prisms reduces the loss and complexity of the system. The principles of operation of this design were demonstrated through a design example in which a circularly-polarized beam-steerable antenna with an overall thickness of 1.1 λ_0 was designed. A prototype of this antenna was fabricated and experimentally characterized. The experimental results corroborated the simulations and demonstrated that the antenna is capable of performing 2D beam-steering over a $\pm 57^\circ$ field of view while maintaining a good polarization purity. The measured peak gain is 22.3 dBc, corresponding to an aperture efficiency of 34.5%. The measured radiation patterns show that the main beam can be scanned from broadside direction to 57° in the upper hemisphere within a gain variation of less than 3.5 dB. This low-complexity and low-profile Risley-prism-based beam-steerable antenna system is expected to be a promising candidate for designing affordable phased-array antennas in applications that do not require very fast beam scan speeds.

Chapter 6

Future Work

In this dissertation, I have investigated and studied several different techniques for designing low-cost, high-power-capable, passive phased-array antennas. This research is developed to satisfy the demands in applications ranging from electronic warfare, high-power radars, satellite and airborne communications to next-generation unmanned systems. These designs include a dual-band reflectarray that has independent phase control at different bands in Chapter 2, a wideband, electronically-reconfigurable, high-power phase shifter that can be used in high-power microwave phased arrays in Chapter 3, an X-band, mechanically-beam-steerable lens antenna exploiting the Risley prism concept in Chapter 4, and a low-profile Risley-prism-based beam-steerable antenna system employing only a single prism in Chapter 5. These studies are vital for my goal of designing low-cost, high-power-capable beam-steerable arrays and lens antennas. Future work based on the previous designs can be extended to the following topics: developing wideband, high-power-capable sub-array demonstrator and extending the bandwidth of Risley-prism-based antenna system.

6.1 Developing Wideband, High-Power-Capable Sub-Array Demonstrator

The high-power-capable phase shifter described in Chapter 3 can be used either in a high-power transmitarray architecture or in a high-power, direct-fed, phased-array architecture. My current plan is to build a 4×1 direct-fed sub-array. The prototype will include all the necessary digital control circuits and the thermal management solutions at the sub-array level. Both low- and high-power experimental characterization of the sub-array will be performed. Low-power experiments will be performed in a near-field anechoic chamber and used to characterize the beam-forming capabilities of the sub-array as well as its gain, efficiency and radiation patterns. High-power characterization will be performed using a high-power magnetron. These measurement results will be used to estimate and model the performance of a large direct-fed array, especially the power handling capability.

6.2 Extending the Bandwidth of Risley-Prism-Based Antenna

One main constraint of Risley-prism-based, mechanically-beam-steerable antenna is the limited bandwidth, which may limit its applications. Generally, the Risley prism antennas are implemented by printed phase-shifting surfaces. Each element of the PSS is treated as a spatial phase shifter providing a given phase shifter at the desired frequency. Additional, each PSS has a saw-tooth-shaped phase distribution over its aperture due to the phase wrapping. This means the overall phase gradient over the antenna's output aperture would change with frequency when rotating the PSSs against each other. This limits the bandwidth of the Risley-prism-based, mechanically-beam-steerable antenna. One possible solution is to use true-time-delay (TTD) spatial phase shifters to implement TTD lens for Risley-prism-based, mechanically-beam-steerable antenna. Since each spatial phase shifter acts as a true-time-

delay unit and is frequency independent, a wideband lens can be obtained. Therefore, the bandwidth of the Risley-prism-based antenna can be extended.

Bibliography

[1] R. C. Hansen, *Phased Array Antennas,* 3rd ed. Hoboken, NJ, USA: John Wiley & Sons., 2009.

[2] R. J. Mailloux, *Phased Array Antenna Handbook,* 3rd ed. Norwood, MA, USA: Artech house, 2017.

[3] M. Harris and R. Sturdivant, *Transmit Receive Modules for Radar and Communication Systems,* Norwood, MA, USA: Artech house, 2015.

[4] B. A. Kopp, M. Borkowski, and G. Jerinic, "Transmit/receive modules," *IEEE Trans. Microw. Theory Techn.*, vol. 50, no. 3, pp. 827–834, Mar. 2002.

[5] A. Fina, A. Di Carlofelice and F. De Paulis, "High power, thermally efficient, X-band 3D T/R module with calibration capability for space radar," *IEEE Access*, vol. 6, pp. 60921-60929, 2018.

[6] A. Di Carlofelice, F. de Paulis, A. Fina, U. Di Marcantonio, A. Orlandi and P. Tognolatti, "Compact and reliable T/R module prototype for advanced space active electronically steerable antenna in 3-D LTCC technology," *IEEE Trans. Microw. Theory Techn.*, vol. 66, no. 6, pp. 2746-2756, June 2018.

[7] Z. Duan, Y. Wang, W. Lv, Y. Dai, and F. Lin, "A 6-bit CMOS active phase shifter for Ku-band phased arrays," *IEEE Microw. Compon. Lett.*, vol. 28, no. 7, pp. 615–617, Jul. 2018.

[8] N. Li et al., "A four-element 7.5–9-GHz phased-array receiver with 1–8 simultaneously reconfigurable beams in 65-nm CMOS," *IEEE Microw. Compon. Lett.*, vol. 69, no. 1, pp. 1114–1126, Jan. 2021.

[9] V.-V. Nguyen, H. Nam, Y. Choe, B.-H. Lee, and J.-D. Park, "An X band bi-directional transmit/receive module for a phased array system in 65-nm CMOS," *Sensors*, vol. 18, no. 8, p. 2569, Aug. 2018.

[10] C. Liu et al., "A fully integrated X-band phased-array transceiver in 0.13-μm SiGe BiCMOS technology," *IEEE Trans. Microw. Theory Techn.*, vol. 64, no. 2, pp. 575–584, Feb. 2016.

[11] S. Sim, L. Jeon, and J. Kim, "A compact X-band bi-directional phased array T/R chipset in 0.13 μm CMOS technology," *IEEE Trans. Microw. Theory Tech.*, vol. 61, no. 1, pp. 562–569, Jan. 2013.

[12] D. Shin, C. Kim, D. Kang, and G. M. Rebeiz, "A high-power packaged four-element X-band phased-array transmitter in 0.13-μm CMOS for radar and communication systems," *IEEE Trans. Microw. Theory Tech.*, vol. 61, no. 8, pp. 3060–3071, Aug. 2013.

[13] H. Nam, V.-V. Nguyen, V.-S. Trinh, J.-M. Song, B.-H. Lee, and J.-D. Park, "A full X-band phased-array transmit/receive module chip in 65-nm CMOS technology," *IEEE Access*, vol. 8, pp. 76182–76192, 2020.

[14] R. R. Romanofsky, "Array phase shifters: Theory and technology,," in *Antenna Engineering Handbook*, J. Volakis, 4th Ed. New York, NY, USA: McGraw-Hill, 2007.

[15] G. M. Rebeiz et al., "Tuning in to RF MEMS," *IEEE Microw. Mag.*, vol. 10, no. 6, pp. 55-72, Oct. 2009.

[16] A. Chakraborty and B. Gupta, "Paradigm phase shift: RF MEMS phase shifters: an overview," *IEEE Microw. Mag.*, vol. 18, no. 1, pp. 22-41, Jan. 2017.

[17] C. D. Patel and G. M. Rebeiz, "A high-reliability high-linearity high-power RF MEMS metal-contact switch for dc–40-GHz applications," *IEEE Trans. Microw. Theory Techn.*, vol. 60, no. 10, pp. 3096-3112, Oct. 2012.

[18] X. Yang et al., "Compact and low loss phase shifter with low bias field using partially magnetized ferrite," *IEEE Trans. Magn.*, vol. 49, no. 7, pp. 3882-3885, July 2013.

[19] F. A. Ghaffar and A. Shamim, "A partially magnetized ferrite LTCC-based SIW phase shifter for phased array applications," *IEEE Trans. Magn.*, vol. 51, no. 6, pp. 1-8, June 2015.

[20] G. J. Deng, W. H. Huang, J. W. Li, T. Ba, L. T. Guo and Y. Jiang, "A novel high power X-band ferrite phase shifter," *Rev. Sci. Instrum.*, vol. 88, Jan. 2017.

[21] V. G. Harris, "Modern microwave ferrites," *IEEE Trans. Magn.*, vol. 48, no. 3, pp. 1075-1104, March 2012.

[22] T. N. Ross, K. Hettak, G. Cormier and J. S. Wight, "Design of X-Band GaN phase shifters," *IEEE Trans. Microw. Theory Techn.*, vol. 63, no. 1, pp. 244-255, Jan. 2015.

[23] W. Luo, H. Liu, Z. Zhang, P. Sun, and X. Liu, "High-power X-band 5-b GaN phase shifter with monolithic integrated E/D HEMTs control logic," *IEEE Trans. Electron Devices*, vol. 64, no. 9, pp. 3627–3633, Sep. 2017.

[24] J. Chen, S. Mou, K. Ma and F. Meng, "A 3–6-GHz wideband compact 6-bit phase shifter in 0.5-μm GaAs technology," *IEEE Microw. Wireless Compon. Lett.*, vol. 30, no. 8, pp. 794-797, Aug. 2020.

[25] Y. Yang, C. Yuan and B. Qian, "A novel phase shifter for Ku-band high-power microwave applications," *IEEE Trans. Plasma Sci.*, vol. 42, no. 1, pp. 51-54, Jan. 2014.

[26] C. Chang et al., "A new compact high-power microwave phase shifter," *IEEE Trans. Microw. Theory Techn.*, vol. 63, no. 6, pp. 1875-1882, June 2015.

[27] K. F. Warnick, R. Maaskant, M. V. Ivashina, D. B. Davidson and B. D. Jeffs, *Phased Arrays for Radio Astronomy Remote Sensing and Satellite Communication*, Cambridge, U.K.:Cambridge Univ. Press, 2018.

[28] G. Han, B. Du, W. Wu, and B. Yang, "A novel hybrid phased array antenna for satellite communication on-the-move in Ku-band," *IEEE Trans. Antennas Propag.*, vol. 63, no. 4, pp. 1375–1383, Apr. 2015.

[29] Advanced Scanning Technology for Imaging Radars (ASTIR), DARPA-BAA-14-53, August 4, 2014.

[30] E. Brookner, "Phased arrays and radars- past, present and future," *Microwave Journal*, pp. 24-46, Jan. 2006.

[31] E. Brookner, "Phased-array radars: past, astounding breakthroughs and future trends," *Microwave Journal*, pp. 30-50, Jan. 2008.

[32] E. Brookner, "Radar and phased array breakthroughs," *Microwave Journal*, pp. 30-50, Jan. 2008.

[33] C. -W. Luo, G. Zhao, Y. -C. Jiao, G. -T. Chen and Y. -D. Yan, "Wideband 1 bit reconfigurable transmitarray antenna based on polarization rotation element," *IEEE Antennas and Wireless Propag. Lett.*, vol. 20, no. 5, pp. 798-802, May 2021.

[34] A. Clemente, L. Dussopt, R. Sauleau, P. Potier and P. Pouliguen, "1-bit reconfigurable unit cell based on PIN diodes for transmit-array applications in X-band," *IEEE Trans. Antennas Propag.*, vol. 60, no. 5, pp. 2260-2269, May 2012.

[35] P. Feng, S. Qu and S. Yang, "Octave bandwidth transmitarrays with a flat gain," *IEEE Trans. Antennas Propag.*, vol. 66, no. 10, pp. 5231-5238, Oct. 2018.

[36] K. Mavrakakis, H. Luyen, J. H. Booske and N. Behdad, "Wideband transmitarrays based on polarization-rotating miniaturized-element frequency selective surfaces," *IEEE Trans. Antennas Propag.*, vol. 68, no. 3, pp. 2128-2137, March 2020.

[37] H. Chen et al., "Ultra-wideband polarization conversion metasurfaces based on multiple plasmon resonances," *J. Appl. Phys.*, vol. 115, no. 15, p. 154504, 2014.

[38] S. Montori et al., "A transportable reflectarray antenna for satellite Ku-band emergency communications," *IEEE Trans. Antennas Propag.*, vol. 63, no. 4, pp. 1393-1407, April 2015.

[39] M.-T. Zhang et al., "Design of novel reconfigurable reflectarrays with single-bit phase resolution for Ku-band satellite antenna applications," *IEEE Trans. Antennas Propag.*, vol. 64, no. 5, pp. 1634-1641, May 2016.

[40] H. Luyen, Z. Yang, M. Gao, J. H. Booske and N. Behdad, "A wideband, single-layer reflectarray exploiting a polarization rotating unit cell," *IEEE Trans. Antennas Propag.*, vol. 67, no. 2, pp. 872-883, Feb. 2019.

[41] H. Luyen, Z. Zhang, J. H. Booske and N. Behdad, "Wideband, beam-steerable reflectarrays based on minimum-switch topology, polarization-rotating unit cells," *IEEE Access*, vol. 7, pp. 36568-36578, 2019.

[42] H. Luyen, J. H. Booske and N. Behdad, "2-bit phase quantization using mixed polarization-rotation/non-polarization-rotation reflection modes for beam-steerable reflectarrays," *IEEE Trans. Antennas Propag.*, vol. 68, no. 12, pp. 7937-7946, Dec. 2020.

[43] H. Luyen, Z. Zhang, J. H. Booske and N. Behdad, "Wideband, beam-steerable reflectarray antennas exploiting electronically reconfigurable polarization-rotating phase shifters," *IEEE Trans. Antennas Propag.*, vol. 70, no. 6, pp. 4414-4425, June 2022.

[44] X. Yang et al., "A mechanically reconfigurable reflectarray with slotted patches of tunable height," *IEEE Antennas and Wireless Propag. Lett.*, vol. 17, no. 4, pp. 555-558, April 2018.

[45] X. Yang et al., "A broadband high-efficiency reconfigurable reflectarray antenna using mechanically rotational elements," *IEEE Trans. Antennas Propag.*, vol. 65, no. 8, pp. 3959-3966, Aug. 2017.

[46] P. Nayeri, F. Yang and A. Z. Elsherbeni, "Bifocal design and aperture phase optimizations of reflectarray antennas for wide-angle beam scanning performance," *IEEE Trans. Antennas Propag.*, vol. 61, no. 9, pp. 4588-4597, Sept. 2013.

[47] G. Wu, S. Qu and S. Yang, "Wide-angle beam-scanning reflectarray with mechanical steering," *IEEE Trans. Antennas Propag.*, vol. 66, no. 1, pp. 172-181, Jan. 2018.

[48] S. M. A. M. H. Abadi, K. Ghaemi, and N. Behdad, "Ultra-wideband, true-time-delay reflectarray antennas using ground-plane-backed, miniaturized-element frequency selective surfaces," *IEEE Trans. Antennas Propag.*, vol. 63, no. 2, pp. 534-542, Feb 2015.

[49] E. B. Lima, S. A. Matos, J. R. Costa, C. A. Fernandes and N. J. G. Fonseca, "Circular polarization wide-angle beam steering at Ka-band by in-plane translation of a plate lens antenna," *IEEE Trans. Antennas Propag.*, vol. 63, no. 12, pp. 5443-5455, Dec. 2015.

[50] P. Naseri, S. A. Matos, J. R. Costa and C. A. Fernandes, "Phase-delay versus phase-rotation cells for circular polarization transmit arrays—application to satellite Ka-band beam steering," *IEEE Trans. Antennas Propag.*, vol. 66, no. 3, pp. 1236-1247, March 2018.

[51] S. A. Matos et al., "High gain dual-band beam-steering transmit array for satcom terminals at Ka-Band," *IEEE Trans. Antennas Propag.*, vol. 65, no. 7, pp. 3528–3539, Jul. 2017.

[52] S. M. A. M. H. Abadi, J. H. Booske, and N. Behdad. "MAcro-Electro-Mechanical Systems (MÆMS) based concept for microwave beam steering in reflectarray antennas," *Journal of Applied Physics*, 120.5: 054901, 2016.

[53] N. Gagnon and A. Petosa, "Using rotatable planar phase shifting surfaces to steer a high-gain beam," *IEEE Trans. Antennas Propag.*, vol. 61, no. 6, pp. 3086-3092, June 2013.

[54] X. Zhao et al., "All-metal beam steering lens antenna for high power microwave applications," *IEEE Trans. Antennas Propag.*, vol. 65, no. 12, pp. 7340-7344, Dec. 2017.

[55] Y. C. Zhong and Y. J. Cheng, "Generating and steering quasi-non-diffractive beam by near-field planar Risley prisms," *IEEE Trans. Antennas Propag.*, vol. 68, no. 12, pp. 7767-7776, Dec. 2020.

[56] M. U. Afzal and K. P. Esselle, "Steering the beam of medium-to-high gain antennas using near-field phase transformation," *IEEE Trans. Antennas Propag.*, vol. 65, no. 4, pp. 1680-1690, April. 2017.

[57] T. Lou, X. Yang, H. Qiu, Z. Yin and S. Gao, "Compact dual-polarized continuous transverse stub array with 2-D beam scanning," *IEEE Trans. Antennas Propag.*, vol. 67, no. 5, pp. 3000-3010, May. 2019.

[58] Y. Sun et al., "A beam-steerable lens antenna for Ku-band high-power microwave applications," *IEEE Trans. Antennas Propag.*, vol. 68, no. 11, pp. 7580-7583, Nov. 2020.

[59] Y. Yang, "Analytic solution of free space optical beam steering using Risley prisms," *J. Lightw. Technol.*, vol. 26, no. 21, pp. 3576–3583, Nov. 2008.

[60] Y. Lu, Y. Zhou, M. Hei, and D. Fan, "Theoretical and experimental determination of steering mechanism for Risley prism systems," *Appl. Opt.*, vol. 52, no. 7, pp. 1389–1398, Mar. 2013.

[61] J. Huang and J. A. Encinar, *Reflectarray Antennas*, 1st ed. Hoboken, NJ, USA: Wiley, 2008.

[62] P. Nayeri, F. Yang and A. Z. Elsherbeni, *Reflectarray Antennas: Theory, Designs and Applications*, Wiley-IEEE Press, 2018.

[63] S. V. Hum and J. Perruisseau-Carrier, "Reconfigurable reflectarrays and array lenses for dynamic antenna beam control: A review," *IEEE Trans. Antennas Propag.*, vol. 62, no. 1, pp. 183–198, Jan. 2014.

[64] P. Nayeri, F. Yang and A. Z. Elsherbeni, "Beam-scanning reflectarray antennas: A technical overview and state of the art," *IEEE Antennas Propag. Mag.*, vol. 57, no. 4, pp. 32-47, Aug. 2015.

[65] H. Kamoda, T. Iwasaki, J. Tsumochi, T. Kuki and O. Hashimoto, "60-GHz electronically reconfigurable large reflectarray using single-bit phase shifters," *IEEE Trans. Antennas Propag.*, vol. 59, no. 7, pp. 2524-2531, Jul. 2011.

[66] H. Yang et al., "A 1-bit 10×10 reconfigurable reflectarray antenna: Design, optimization, and experiment," *IEEE Trans. Antennas Propag.*, vol. 64, no. 6, pp. 2246-2254, Jun. 2016.

[67] T. Debogovic and J. Perruisseau-Carrier, "Low loss MEMS-reconfigurable 1-bit reflectarray cell with dual-linear polarization," *IEEE Trans. Antennas Propag.*, vol. 62, no. 10, pp. 5055-5060, Oct. 2014.

[68] H. Zhang, X. Chen, Z. Wang, Y. Ge and J. Pu, "A 1-Bit electronically reconfigurable reflectarray antenna in X Band," *IEEE Access*, vol. 7, pp. 66567-66575, 2019.

[69] J. Han, L. Li, G. Liu, Z. Wu and Y. Shi, "A wideband 1 bit 12 × 12 reconfigurable beam-scanning reflectarray: Design fabrication and measurement," *IEEE Antennas and Wireless Propag. Lett.*, vol. 18, no. 6, pp. 1268-1272, 2019.

[70] E. Carrasco, M. Barba, J. A. Encinar, "X-Band reflectarray antenna with switching-beam using PIN diodes and gathered elements," *IEEE Trans. Antennas Propag.*, vol. 60, no. 12, pp. 5700-5708, 2012.

[71] Y. Zhong, H. Luyen and N. Behdad, "1-bit, low-complexity, 20 × 20-element electronically reconfigurable reflectarray antenna," *2019 13th European Conf. Antennas Propagation (EuCAP)*, Krakow, Poland, 2019, pp. 1-3.

[72] A. Aziz, F. Yang, S. Xu and M. Li, "An efficient dual-band orthogonally polarized transmitarray design using three-dipole elements," *IEEE Antennas Wireless Propag. Lett.*, vol. 17, no. 2, pp. 319–322, Feb. 2018.

[73] R. Wu, Y. B. Li, W. Wu, C. Shi and T. J. Cui, "High-Gain dual-band transmitarray," *IEEE Trans. Antennas Propag.*, vol. 65, no. 7, pp. 3481– 3488, Jul. 2017.

[74] K. T. Pham, R. Sauleau, E. Fourn, F. Diaby, A. Clemente and L. Dussopt, "Dual-band transmitarrays with dual-linear polarization at Ka-band," *IEEE Trans. Antennas Propag.*, vol. 65, no. 12, pp. 7009–7018, Dec. 2017.

[75] S. A. Matos et al., "High gain dual-band beam-steering transmit array for satcom terminals at Ka-Band," *IEEE Trans. Antennas Propag.*, vol. 65, no. 7, pp. 3528–3539, Jul. 2017.

[76] A. Aziz, F. Yang, S. Xu, M. Li and H. Chen, "A high-gain dual-band and dual-polarized transmitarray using novel loop elements," *IEEE Antennas Wireless Propag. Lett.*, vol. 18, no. 6, pp. 1213-1217, June 2019.

[77] T. Smith, U. V. Gothelf, O. S. Kim, and O. Breinbjerg, "Design, manufacturing, and testing of a 20/30 GHz dual-band circularly polarized reflectarray antenna," *IEEE Antennas and Wireless Propag. Lett.*, vol. 12, pp. 1480–1483, 2013.

[78] R. S. Malfajani and Z. Atlasbaf, "Design and implementation of a dual-band single layer reflectarray in X and K bands," *IEEE Trans. Antennas Propag.*, vol. 62, no. 8, pp. 4425–4431, Aug. 2014.

[79] M. R. Chaharmir and J. Shaker, "Design of a multilayer X/Ka-band frequency-selective surface-backed reflectarray for satellite applications," *IEEE Trans. Antennas Propag.*, vol. 63, no. 4, pp. 1255–1264, Apr. 2015.

[80] L. Guo, P.-K. Tan, and T.-H. Chio, "Single-layered broadband dual-band reflectarray with linear orthogonal polarizations," *IEEE Trans. Antennas Propag.*, vol. 63, no. 9, pp. 4064–4068, Sep. 2016.

[81] R. Deng, Y. Mao, S. Xu and F. Yang, "A single-layer dual-band circularly polarized reflectarray with high aperture efficiency," *IEEE Trans. Antennas Propag.*, vol. 63, no. 7, pp. 3317-3320, July 2015.

[82] R. S. Malfajani and B. A. Arand, "Dual-band orthogonally polarized single-layer reflectarray antenna," *IEEE Trans. Antennas Propag.*, vol. 65, no. 11, pp. 6145-6150, Nov. 2017.

[83] R. Deng, F. Yang, S. Xu and M. Li, "An FSS-backed 20/30-GHz dual-band circularly polarized reflectarray with suppressed mutual coupling and enhanced performance," *IEEE Trans. Antennas Propag.*, vol. 65, no. 2, pp. 926-931, Feb. 2017.

[84] R. Deng, S. Xu, F. Yang, and M. Li, "Single-layer dual-band reflectarray antennas with wide frequency ratios and high aperture efficiencies using phoenix element," *IEEE Trans. Antennas Propag.*, vol. 65, no. 2, pp. 612–622, Feb. 2017.

[85] T. Su, X. Yi and B. Wu, "X/Ku dual-band single-layer reflectarray antenna," *IEEE Antennas Wireless Propag. Lett.*, vol. 18, no. 2, pp. 338-342, Feb. 2019.

[86] M. Abdollahvand, K. Forooraghi, J. A. Encinar, Z. Atlasbaf and E. Martinez-de-Rioja, "A 20/30 GHz reflectarray backed by FSS for shared aperture Ku/Ka-band satellite communication antennas," *IEEE Antennas Wireless Propag. Lett.*, vol. 19, no. 4, pp. 566-570, April 2020.

[87] P. Naseri, M. Riel, Y. Demers and S. V. Hum, "A dual-band dual-circularly polarized reflectarray for K/Ka-band space applications," *IEEE Trans. Antennas Propag.*, vol. 68, no. 6, pp. 4627-4637, June 2020.

[88] A. Tayebi, J. Tang, P. R. Paladhi, L. Udpa, S. S. Udpa and E. J. Rothwell, "Dynamic beam shaping using a dual-band electronically tunable reflectarray antenna," *IEEE Trans. Antennas Propag.*, vol. 63, no. 10, pp. 4534-4539, Oct. 2015.

[89] H. Yang et al., "A 1600-element dual-frequency electronically reconfigurable reflectarray at X/Ku-band," *IEEE Trans. Antennas Propag.*, vol. 65, no. 6, pp. 3024-3032, June 2017.

[90] C. Guclu, J. Perruisseau-Carrier and O. Civi, "Proof of concept of a dual-band circularly-polarized RF MEMS beam-switching reflectarray," *IEEE Trans. Antennas Propag.*, vol. 60, no. 11, pp. 5451–5455, Nov. 2012.

[91] A. Yu, F. Yang, A. Z. Elsherbeni, J. Huang and Y. Rahmat-Samii, "Aperture efficiency analysis of reflectarray antennas," *Microw. Opt. Technol. Lett.*, vol. 52, no. 2, pp. 364–372, Feb. 2010.

[92] C. A. Balanis, *Antenna Theory: Analysis and Design*, 4th ed. Hoboken, NJ, USA: Wiley, 2016.

[93] L. Guo, W. Huang, C. Chang, J. Li, Y. Liu and R. Meng, "Studies of a leaky-wave phased array antenna for high-power microwave applications," *IEEE Trans. Plasma Sci.*, vol. 44, no. 10, pp. 2366-2375, Oct. 2016.

[94] Y. Liang, J. Zhang, Q. Liu and X. Li, "High-power radial-line helical subarray for high-frequency applications," *IEEE Trans. Antennas Propag.*, vol. 66, no. 8, pp. 4034-4041, Aug. 2018.

[95] G. Kong, X. Li, Q. Wang and J. Zhang, "A wideband reconfigurable dual-branch helical reflectarray antenna for high-power microwave applications," *IEEE Trans. Antennas Propag.*, vol. 69, no. 2, pp. 825-833, Feb. 2021.

[96] L. Yu, C. Yuan, J. He and Q. Zhang, "Beam steerable array antenna based on rectangular waveguide for high-power microwave applications," *IEEE Trans. Plasma Sci.*, vol. 47, no. 1, pp. 535-541, Jan. 2019.

[97] Z. Zhang, H. Luyen, J. H. Booske and N. Behdad, "A dual-band, polarization-rotating reflectarray with independent phase control at each band," *IEEE Trans. Antennas Propag.*, vol. 69, no. 9, pp. 5546-5558, Sept. 2021.

[98] J. Yin, Q. Wu, Q. Lou, H. Wang, Z. N. Chen and W. Hong, "Single-beam 1 bit reflective metasurface using prephased unit cells for normally incident plane waves," *IEEE Trans. Antennas Propag.*, vol. 68, no. 7, pp. 5496-5504, July 2020.

[99] B. G. Kashyap, P. C. Theofanopoulos, Y. Cui and G. C. Trichopoulos, "Mitigating quantization lobes in mmwave low-bit reconfigurable reflective surfaces," *IEEE Open J. Antennas Propag.*, vol. 1, pp. 604-614, 2020.

[100] K. Sarabandi and F. T. Ulaby, "Technique for measuring the dielectric constant of thin materials," *IEEE Trans. Instrum. Meas.*, vol. 37, pp. 631–636, Dec. 1988.

[101] R. H. Caverly and G. Hiller, "Establishing the minimum reverse bias for a p-i-n diode in a high-power switch," *IEEE Trans. Microw. Theory Techn.*, vol. 38, no. 12, pp. 1938–1943, Dec. 1990.

[102] Macom, "Design with PIN Diodes" [Online]. Available: https://cdn.macom.com/applicationnotes/AG312.pdf [Accessed: 17-September-2021].

[103] J. C. Pedro and N. B. Carvalho, *Intermodulation Distortion in Microwave and Wireless Circuits*, Norwood, Boston, MA, USA: Artech House, 2003.

[104] R. H. Caverly and G. Hiller, "Distortion in p-i-n diode control circuits," *IEEE Trans. Microw. Theory Techn.*, vol. 35, no. 5, pp. 492-501, May 1987.

[105] C.-H. Liu and N. Behdad, "High-power microwave filters and frequency selective surfaces exploiting electromagnetic wave tunneling through epsilon-negative layers," *J. Appl. Phys.*, vol. 113, no. 6, p. 064909, 2013.

[106] M. Li and N. Behdad, "Frequency selective surfaces for pulsed high power microwave (HPM) applications," *IEEE Trans. Antennas Propag.*, vol. 61, no. 2, pp. 677–687, Feb. 2013.

[107] C.-H. Liu and N. Behdad, "Investigating the impact of microwave breakdown on the responses of high-power microwave metamaterials," *IEEE Trans. Plasma Sci.*, vol. 41, no. 10, pp. 2992–3000, Oct. 2013.

[108] C. Liu, J. D. Neher, J. H. Booske and N. Behdad, "Investigating the physics of simultaneous breakdown events in high-power-microwave (HPM) metamaterials with multiresonant unit cells and discrete nonlinear responses," *IEEE Trans. Plasma Sci.*, vol. 42, no. 5, pp. 1255-1264, May 2014.

[109] C. Liu et al., "Metamaterials for rapidly forming large-area distributed plasma discharges for high-power microwave applications," *IEEE Trans. Plasma Sci.*, vol. 43, no. 12, pp. 4099-4109, Dec. 2015.

[110] E. Tolin, O. Litschke, S. Bruni and F. Vipiana, "Compact extended scan range antenna array based on Rotman lens," *IEEE Trans. Antennas Propag.*, vol. 67, no,12, pp. 7356–7367, Dec. 2019.

[111] J. G. Marin and J. Hesselbarth, "Lens antenna with planar focal surface for wide-angle beam-steering application," *IEEE Trans. Antennas Propag.*, vol. 67, no. 4, pp. 2757-2762, April 2019.

[112] A. Clemente, L. Dussopt, R. Sauleau, P. Potier and P. Pouliguen, "Wideband 400-element electronically reconfigurable transmitarray in X band," *IEEE Trans. Antennas Propag.*, vol. 61, no. 10, pp. 5017-5027, Oct. 2013.

[113] M. Li and N. Behdad, "Wideband true-time-delay microwave lenses based on metallo-dielectric and all-dielectric lowpass frequency selective surfaces," *IEEE Trans. Antennas Propag.*, vol. 61, no. 8, pp. 4109-4119, Aug. 2013.

[114] A. H. Abdelrahman, A. Z. Elsherbeni and F. Yang, "Transmission phase limit of multilayer frequency selective surfaces for transmitarray designs," *IEEE Trans. Antennas Propag.*, vol. 62, no. 2, pp. 690-697, Feb. 2014.

[115] Z. Zhang, H. Luyen, J. H. Booske, and N. Behdad, "X-band, mechanically-beam-steerable lens antenna exploiting the Risley prism concept," *IET Microw., Antennas Propag.*, vol. 14, no. 14, pp. 1902 –1908, 2020.

[116] B. H. Fong, J. S. Colburn, J. J. Ottusch, J. L. Visher and D. F. Sievenpiper, "Scalar and tensor holographic artificial impedance surfaces," *IEEE Trans. Antennas Propag.*, vol. 58, no. 10, pp. 3212-3221, Oct. 2010.

[117] G. Minatti, F. Caminita, M. Casaletti and S. Maci, "Spiral leaky-wave antennas based on modulated surface impedance," *IEEE Trans. Antennas Propag.*, vol. 59, no. 12, pp. 4436-4444, Dec. 2011.

[118] A. M. Patel and A. Grbic, "A printed leaky-wave antenna based on a sinusoidally-modulated reactance surface," *IEEE Trans. Antennas Propag.*, vol. 59, no. 6, pp. 2087–2096, Jun. 2011.

[119] S. Pandi, C. A. Balanis, and C. R. Birtcher, "Design of scalar impedance holographic metasurfaces for antenna beam formation with desired polarization," *IEEE Trans. Antennas Propag.*, vol. 63, no. 7, pp. 3016–3024, Jul. 2015.

[120] G. Minatti et al., "Modulated metasurface antennas for space: synthesis, analysis and realizations," *IEEE Trans. Antennas Propag.*, vol. 63, no. 4, pp. 1288-1300, April. 2015.

[121] G. Minatti, F. Caminita, E. Martini, M. Sabbadini and S. Maci, "Synthesis of modulated-metasurface antennas with amplitude, phase, and polarization control," *IEEE Trans. Antennas Propag.*, vol. 64, no. 9, pp. 3907-3919, Sept. 2016.

[122] G. Minatti, E. Martini and S. Maci, "Efficiency of metasurface antennas," *IEEE Trans. Antennas Propag.*, vol. 65, no. 4, pp. 1532-1541, April. 2017.

[123] M. Karimipour and N. Komjani, "Holographic-inspired multibeam reflectarray with linear polarization," *IEEE Trans. Antennas Propag.*, vol. 66, no. 6, pp. 2870-2882, June. 2018.

[124] M. Li, S. Xiao and D. F. Sievenpiper, "Polarization-insensitive holographic surfaces with broadside radiation, " *IEEE Trans. Antennas Propag.*, vol. 64, no. 12, pp. 5272-5280, Dec. 2016.